Resonant Cantilever Sensing:
From Model Systems to Application

Rosemary Paxman

London Centre for Nanotechnology
University College London

Supervisors:
Dr. Bart Hoogenboom
Dr. Rachel McKendry

Thesis submitted for the degree of
Doctor of Engineering at University College London

February 2013

I, Rosemary Paxman, confirm that the work presented in this thesis is my own. Where information has been derived from other sources, I confirm that this has been indicated in the thesis.

Abstract

Micro and nanomechanical resonators are highly sensitive, label-free analyte sensors in a range of environments. Resonant cantilevers, i.e. those operated in dynamic mode, can be considered as mechanical oscillators, with analyte adsorption creating a shift in cantilever resonance. Cantilever sensors work via a purely mechanical approach, transducing an analyte binding event into a nanomechanical signal. This response is governed by changes in sensor mass and stiffness due to adsorbed analytes, with previous theoretical work predicting the latter to produce significant effects on measured frequency shifts, *counteracting* effects of adsorbed mass. This highlights a particularly unsatisfactory feature of micro/nano-mechanical sensors, as an accurate interpretation of the sensor response must depend on both adsorbate mass and rigidity, which for nanometer-scale coverage can only be guessed, rather than derived from independent measurements. In this thesis, procedures to disentangle such effects in air and liquid are discussed and tested on a range of surface coatings, offering a novel method of analyte detection and analysis.

The dynamic characteristics of cantilever beams are strongly dependent on the mass density and viscosity of the fluid in which the beams are immersed. The application of cantilevers in accurately determining such rheological properties is also presented, first via the use of model solutions, and then extending measurements to a range of commercial alcoholic and non-alcoholic drinks. A method to quantify alcohol content is also discussed, further demonstrating the commercial applications of cantilever sensors.

Acknowledgements

The work in this thesis would not be possible without the following people, who I would like to thank for their encouragement and support throughout.

First and foremost, I would like to thank my supervisors Dr. Bart Hoogenboom and Dr. Rachel McKendry. Their academic guidance has been invaluable throughout and I would not have been able to complete my EngD research without it. I thank you for our fruitful discussions during meetings, your continued support and for reviewing this thesis. I would also like to thank Dr. Hoogenboom and Dr. McKendry for the opportunity to work in the fascinating and ever-developing area of cantilever sensing, along with the conference and travel opportunities which have come with this.

I would also like to thank the all members of both Dr. Hoogenboom and Dr. McKendry's research groups for the opportunity to discuss my research with such a receptive audience. I gratefully acknowledge Professor Marshall Stoneham for his discussions; Dr. Joseph Ndieyira for his generosity and enthusiasm; Dr.Carl Leung and Dr Nitya Gosvami for their kind helpfulness and support; Alice Payne, Dino Osmanovic, Aizhan Bestembayeva and Sebastian Hoof for helping make such a sociable research group; Zermina Khan for her friendship and encouragement and Anna Dejardin for her insights into computer simulations. I also wish to thank past-group members, particularly Raphael Grüter, for helping me to 'hit the ground running' when starting my research.

I would like to thank Richard Thorogate for managing the laboratories and consumables, and for helping develop my understanding of operating the JPK Nanowizard I AFM.

I also thank Dr. Maria Sushko for her insight and discussion with regards to self-assembled monolayer experiments.

I am further grateful for financial support received from the UCL Graduate School, UCL Graduate Fund, namely the scholarships that funded my PhD, a conference travel grant, and the opportunity to attend the UCL-Beijing summer school. I also wish to thank the Department of Chemistry’s Molecular Modelling and Materials Simulation Doctoral Training Centre fund and the Physical Sciences Research Council (EPSRC).

I would like to thank my friends for making my time in London so enjoyable. In particular, I would like to thank those from my time as an undergraduate at The University of York who also descended on London after graduation.

Most importantly, I would like to thank my grandparents, parents, brothers, sisters-in-law and nephew for their unwavering support. I would also like to thank my family-in-law Keith, June, Garry and Anna for their understanding at my recent missed trips to the west-midlands, and for so warmly welcoming me into their family.

Last but by no means least, I would like to thank my partner Neil. Your tireless encouragement and support has been invaluable over the last few months, as has your cooking! I dedicated this thesis to my family and you.

Contents

CONTENTS

CONENTS

List of Figures

LIST OF FIGURES

List of Tables

Abbreviations

AFM	Atomic Force Microscopy
Γ	Hydrodynamic function
CCl_4	Carbon tetrachrloide
Δd	PSD displacement signal
D_0	Unloaded cantilever flexural rigidity
D	Cantilever flexural rigidity
DAla	Mucopeptide analogues terminating in L-Lysine-D-Alanine-D-Alanine (vancomycin suscebtible)
DNA	Deoxyribosenucleic Acid
H	Viscosity
E.Coli	Escherichia coli
E_a	Adsorbate Young's modulus
E_c	Cantilever Young's modulus
EtOH	Ethanol

ABBREVIATIONS

$f_0^{(n)}$	Natural frequency of the n-th mode of cantilever oscillation
$f_{res}^{(n)}$	Resonance frequency of the n-th mode of cantilever oscillation
$f_{0,air}^{(n)}$	Natural frequency of the n-th mode of bare cantilever oscillation in air
$f_{0,vac}^{(n)}$	Natural frequency of the n-th mode of bare cantilever oscillation in vacuum
FIB	Focussed Ion Beam microscope
Γ_i	Imaginary part of hydrodynamic function
k	Spring constant
K_d	Equilibrium dissociation constant
l	Cantilever length
μ	Mass per unit length of the cantilever beam
m^*	Effective mass
m_0	Mass of unloaded cantilever
m_a	Adsorbate mass
m_c	Cantilever mass
n	Alkyl chain length
n-th	Flexural oscillation mode number
PEG	Thiol terminating in triethylene glycol (reference coating)
PSD	Position sensitive detector
PVD	Physical vapour deposition
$Q_0^{(n)}$	Quality factors of n-th mode of the unloaded cantilever
$Q^{(n)}$	Quality factors of n-th mode of the loaded cantilever

ABBREVIATIONS

QCM	Quartz crystal microbalance
ρ_c	Mass density of the cantilever (typically the density of Silicon)
ρ_m	Mass density of the surrounding medium
Γ_r	Real part of the hydrodynamic function
R	Radius of curvature
S	Entropy
SAM	Self-assembled monolayer
SAW	Surface acoustic wave
SEM	Scanning electron microscopy
SFM	Scanning force microscopy
SHO	Simple harmonic oscillator
SLD	Superluminous diodes
SPR	Surface plasmon resonance
STM	Scanning Tunnelling Microscopy
t_a	Adsorbate thickness
t_c	Cantilever thickness
v	Poission ratio
VSE	Vancomycin-sensitive Enterococci
w	Cantilever width
X	SAM terminating group
Δx	Cantilever deflection

CHAPTER 1

Introduction

1.1 Introduction to Cantilever Sensors

Nanomechanical cantilever sensors have been widely used as miniaturized, selective, fast-responding sensors in chemistry, medicine and physics [Lavrik04, Lang07, Goeders08]. They have attracted much attention due to their overall favourable capabilities, including parallelisation, miniaturisation, integration, and mass production [Vettiger00]. The advent of atomic force microscopy (AFM) over 20 years ago [Binning86] brought with it an increase in microcantilever production and consequently a growth in cantilever sensor research and development. AFM was originally developed to help overcome a basic drawback with Scanning Tunnelling Microscopy (STM) techniques, which imaged only conducting or semiconducting surfaces. AFM, however, has the advantage of imaging almost any type of surface, including polymers, ceramics, composites, glass, and biological samples. Typically AFMs use a laser beam deflection system, where a laser is reflected from the back of the reflective AFM lever onto a position-sensitive detector. The AFM cantilever tips are microfabricated from Si or Si_3N_4, with a tip radius ranging from a few to 10s of nanometres. In sample imaging, the cantilever tip is brought into close proximity with the sample surface, with forces between the tip and the sample creating a deflection of the cantilever according to Hooke's law. Forces typically measured in AFM include mechanical contact force, Van der Waals, capillary forces, chemical bonding, and electrostatic forces; it is the use of AFM cantilevers as nanomechanical sensors which will form the focus of this thesis.

Cantilever sensor operation is based on their ability to act as a transducer, detecting changes in cantilever mass or stiffness and converting this into a convenient output. Sensing parameters include: resonance frequency; quality factor; spring constant and degree of bending as a result of differential stress. These devices are typically microfabricated rectangular-shaped bars of silicon, generally regarded to be longer than they are wide, and have a thickness much smaller than their length or width. A schematic of their design is shown in Figure 1.1. The structure of these sensors consists of a fixed and moveable part, with the moveable component being a thin membrane, plate or beam. The free end can then be used as a mechanical probe to image sample topography via AFM or scanning force microscopy (SFM). In the case of AFM imaging cantilevers, a sharp tip is adhered to the cantilever’s apex and can be used to locally scan the sample surface. In this thesis we focus on tipless cantilevers as any additional mass at the end of the cantilever will reduce the sensor’s sensitivity and decreases the frequency shift induced by adsorbed analytes or changes in the surrounding medium. A tip-correction factor can be included, accounting for the mass and volume of the tip, however this additional step can complicate analysis and reduce the reliability of the results. For these reasons, only tipless cantilevers will be considered in this thesis.

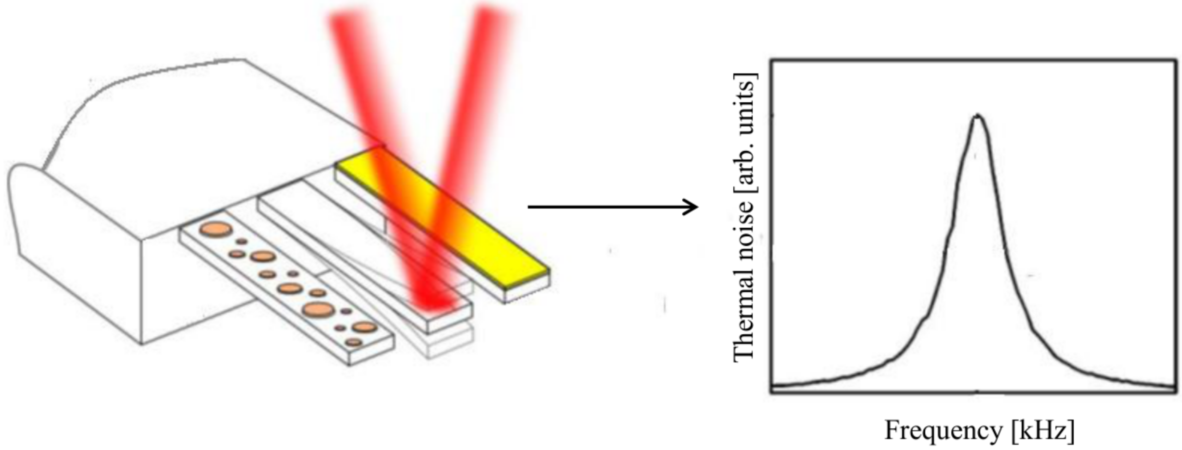

Figure 1.1 *Schematic illustration of a rectangular cantilever with dimensions and coordinate system. The origin of the coordinate system is at the centre of mass of the beam cross section at its clamped end. l, w,* t_c *represent the cantilever's length, width and thickness respectively.*

1.2 History of Cantilever Sensors

The use of cantilevers as chemical sensors dates back to the 1940's [Norton43]. Here, Norton proposed a hydrogen detector based on a bimetallic plate. Nearly 30 years later, measurement of adsorption-induced bending and resonance frequency changes using silicon beams was described by Wilfinger [Wilfinger68]. *S*ilicon cantilevers of dimensions 50mm × 30mm × 8mm were used, much larger than those used today, which are typically of the micrometer scale.

Increased availability of microfabricated cantilevers brought with it more frequent publications researching the application of cantilevers as sensors. Itoh *et al.* demonstrated the use of cantilever sensors coated with a thin layer of zinc oxide, also proposing piezoresistive deflection as an alternative to optical read-out methods [Itoh94]. Along with this, Gimzewski *et al.* presented the first chemical sensing applications via static mode bending to observe chemical reactions with high sensitivity [Gimzewski94]. In findings by Thundat, the cantilever's resonance frequency and static deflection were found to be influenced by thermal ambient conditions and in the case of metal coated cantilevers, a bimetallic effect was observed [Thundat94]. This describes the thermally induced stress commonly seen in metal coated cantilevers, where the base metal and the metal coating have differing thermal expansion coefficients. As a result one side will undergo a measurable bending in response to temperature changes. This work was later developed by Thundat [Thundat95], where changes in a cantilever's resonance frequency upon analyte vapour adsorption were recorded. It was concluded that such changes are due to changes in the spring constant, brought about by either mass loading or being adsorption-induced.

A further benefit of cantilever sensors is their ability to operate in gas, liquid and vacuum environments, making them a versatile sensing platform. When oscillated in liquid, the cantilever experiences fluid damping and subsequently a reduction in resonance frequency and quality factor. The ability to utilise this as a fluid mass density and viscosity sensors can be widely found in the literature [Sader98, Chon00, Boskovic02] and is a characteristic also investigated in this thesis, using cantilevers to detect alcohol content in everyday drinks (chapter 6).

1.3 Comparison to other sensing techniques

Along with cantilever sensing, other techniques are available in mass detection and biosensing. These include Quartz Crystal Microbalance (QCM), Surface Plasmon Resonance (SPR) and Surface Acoustic Wave (SAW) devices.

Microsensors which use acoustic waves encompass a very versatile class of sensor. They are already fabricated on a large scale for the telecommunication industry [Pohl00]; however their development in the sensors field is a relatively new phenomenon. SAW sensor design comprises of a piezoelectric substrate with an input (transmitting) and output (receiving) transducer deposited on top of the substrate. Such devices can be used in the determination of solid or fluid properties, such as: liquid density; liquid viscosity; polymer elastic modulus and electrical conductivity [McCullen89, Khelbarov92, Grate93]. Furthermore their high sensitivity to surface mass changes makes them ideal for use as chemical sensors.

SAW devices have received widespread use in the field of electronic-nose applications. Here, the device is coated with a sensitive receptor-specific polymer membrane, creating a change in the frequency of the wave to change upon interaction with a compatible analyte. The broad range of possible gas sensitive polymer coatings means SAW devices can detect a broad spectrum of odours [Carey86, Grate91]. They also offer high sensitivity and fast response times [Nagle98]. Polymer-coated SAWs further offer relatively low detection sensitivity. For example, tetrachloroethylene, trichloroethylene and methoxyflurane have been detected at concentrations as low as 0.7, 0.6 and 4ppm, respectively [Albert00]. However the nature of the device also means the necessary circuitry needed to operate them is complex and expensive [Pearce03].

Quartz crystal microbalance (QCM) sensors operate on a similar principle to SAW devices. Application of an AC voltage across the piezoelectric quartz crystal causes the material to oscillate at its resonant frequency, normally between 10 and 30MHz [Schaller98]. The resonance can then be altered by mass addition. Due to their high mass sensitivity (typically ng cm^{-3}) QCMs have proved to be a useful tool in surface film investigation, for example in adsorption, deposition and dissolution [Binning86] and molecular recognition [Wegener01]. QCM has a variety of uses as a piezoelectric device, in particular for measurements in high pressure environments, where other microbalances might be unsuitable. As with cantilevers, QCMs can be operated under vacuum, in the gas phase [King64] and in liquid [Bruckenstein85]. They are commonly applied to the monitoring of deposition rate in thin film deposition systems operated under vacuum. Detection of biomolecular interactions towards surfaces functionalized with recognition sites has also been demonstrated [Marx03, Yang05]. Electromechanical methods such as QCM do not require labelling, as they measure mass changes associated with binding to the biorecognition element. This makes them attractive for use in drug screening applications as labelling can introduce variability. Label-free methods are inherently better as they reduce any conformation uncertainties caused by labelling. In addition, QCMs extension to high-throughput assays has been limited due to scaling issues, even though attempts to build multi-channel devices have been reported [Tatsuma99, Dostálek05].

Frequency measurements are easily made to high precision with QCM, hence it is easy to measure masses in the region of micrograms [Muratsugu93]. Along with this, dissipation is often measured to help analysis, quantifying the damping in the system. This can then be related to the sample's viscoelastic properties. QCM response times can range from approximately 10 seconds [Haug93] to between 30 seconds - 1 min [Carey87], placing it on a par with cantilever sensing technologies.

Drawbacks of QCM gas sensors include complex fabrication processes and circuitry, [Nagle98], and, as with SAW, a poor signal to noise ratio brought about by the surface interferences and crystal size [Nagle98]. Batch-to-batch reproducibility of QCM gas sensors can also be problematic [Dickinson98]. Furthermore, QCM gives a lower sensitivity compared to micromechanical sensors, whose small size offers detectable concentration sensitivities generally two orders of magnitude greater [O'Sullivan99, Sepaniak02, Chapman07,].

Unlike other mechanical oscillators, cantilevers benefit from the fact their fabrication is not limited to only one type of material. For example, fabrication of SAW devices is restricted to piezoelectric materials.

One key disadvantage of single microcantilevers sensors is their susceptibility to thermal drift and chemical interactions with their surrounding environment. To exclude such differences, multiple cantilever arrays are used. The reference cantilever is aligned in the same array as the sensing cantilever and small sensor responses can be determined from large cantilever deflections without being dominated by undesired effects, such as thermal drift or chemical interaction between the cantilever and its environment. This is achieved by observing a difference in signals between the reference and the sensor cantilevers and this shows a net cantilever response.

1.4 Applications of Cantilever Sensors

1.4.1 Overview

Tipless cantilevers are widely used as fast, selective miniaturized sensors in chemistry, medicine and physics [Lavrik04, Lang07, Goders08]. Cantilever-based mass sensors have proved promising in ultrasensitive particle detection. As a result of their miniaturisation, they are capable of detection down to the atomic scale in vacuum [Yang06] as well as atto- and zeptogram (10^{-18} – 10^{-21} g) ranges.

Microcantilevers have proved of particular interest due to their high specificity, high sensitivity, simplicity, low cost, low analyte requirement, quick and non-hazardous usage procedures. Substances at trace levels can also be detected by various techniques including high performance liquid chromatography (HPLC), gas chromatography (GC), thin layer chromatography (TLC) and gas liquid chromatography (GLC). These techniques however are more complex, time-consuming and costly.

1.4.2 Biological Applications

Biosensors are important for medical diagnostics, drug analysis, and cell detection. The range of biological systems that have been investigated by cantilevers is vast, ranging from DNA [Fritz00, Fritz02, McKendry02] to proteins [Backmann05], and cells [Ilic01].

An important landmark in the development of cantilever biosensors was demonstration of their application in DNA analysis. Fritz [Fritz00] published results on the monitoring of oligonucleotide hybridisation via functionalised cantilever arrays and optical detection. This pioneered the use of cantilevers in the detection of nucleic acid hybridisation. Their use has become more widespread [McKendry02], finding cantilever arrays to permit multiple binding assays in parallel, also detecting femtomoles of DNA on the cantilever at a DNA concentration in solution of 75 nM. The simpler case of bacteria detection in air has also been reported, with the mass of a single *Escherichia coli* (*E. coli*) cell reported as 665 femtogram (fg) [Ilic01].

Biosensors have been used in the detection of cells and viruses [Ilic01, Ilic04] with the physics of the nanomechanical biosensor response studied by Sushko [Sushko08]. This reported the first quantitative multiscale model to describe the transduction of specific biochemical reactions into micromechanical cantilever bending motion. Here, model biological interfaces were created using alkanethiol self-assembled monolayers (SAMs) on cantilever arrays. In order to further study the effects of surface stress, model alkanethiol SAMs $HS(CH_2)_{n-1}X$ of chain lengths n-1 (n=3, 8, 11, 16) with either an ionizable, carboxylic acid terminal group (X=COOH) or a non-ionizable, methyl terminal group ($X=CH_3$) were used. In contrast to intrinsically complex biomolecules, which have multiple functional and zwitterionic groups, alkanethiols form well-defined SAMs upon adsorption onto a gold surface. The surface properties are controlled by the thiol chain length and terminal group. Notably, the acid-base properties of carboxylic acid terminating SAMs, which can be controlled via the pH of the aqueous environment, offer an ideal system for fundamental studies with broad applicability to colloidal science and membrane biophysics.

The results of this study have been investigated further in chapter five of this thesis. Despite an increasing number of publications reporting cantilever biosensing applications based on deflection observations, disentangling the adsorbate mass, stiffness and rigidity factors which influence the nanomechanical response has been rarely addressed.

While reactions of SAMs have previously been studied on cantilevers, results have varied widely [Raiteri00, Fritz00b] and have suffered limitations as a result of a lack of mechanical sensitivity, or the use of single cantilever measurements. These face the additional problems of susceptibility to non-specific reactions, changes in temperature, refractive index and reactions occurring on the non-functionalised sites of a cantilever. Differential measurements using an *in-situ* reference cantilever modified with control, non-reactive coating has been shown to be vital when detecting chemically specific surface forces. Furthermore, such control functionalisation enables multiple reactions to be probed in parallel, under similar experimental conditions [Fritz00, Fritz00b, McKendry02].

1.4.3 Fluid Measurements

1.4.3.1 Mass and rigidity sensing

Nanomechanical resonators enable the measurement of mass with high sensitivity. However this ability is significantly reduced in fluid, in part due to reduction in the quality factor. The application of nanomechanical sensors becomes more complex when operated in liquid due to damping effects from the increased viscosity of the surrounding medium [Sader98]. Resultantly, the quantification of adsorbate mass in fluid has received much interest [Ghatkesar04, Burg07].

An early use of cantilevers as mass sensors for micro-sized particles is seen in the detection of 10 µm diameter latex beads using silicon dioxide cantilevers. In a leading example of cantilevers operating as biosensors, the sensors demonstrated a lowest detectable mass of approximately 0.2 ng [Prescesky92].

Single particle detection was a milestone for cantilever mass sensors, but these measurements were performed in air. Detection of few cells on a cantilever surface in liquid has been difficult to quantify due to large damping in liquid and the resulting decrease in the quality factor. Mass detection of latex beads using biotin–streptavidin interactions were performed by calculating the resonant frequency shifts at higher order harmonic frequencies [Braun05], showing a time-resolved mass adsorption of 7±0.7 ng. Additional studies have shown the use of cantilevers to detect and monitor the growth of *E. coli* cells [Gfeller05] in liquid, with the sensor detecting active growth of *E. coli* cells within 1 h, offering a significantly faster alternative to conventional plating method which requires at least 24 h.

For real-time biological detection in liquid, a novel hollow cantilever has been described, where liquid flows inside the cantilever, allowing for measurement of resonant frequency changes to be done in air [Burg03]. A mass sensitivity of 0.1 Hz/pg was observed and since this design does not reduce the cantilever’s quality factor, achieving much higher sensitivities should be possible. The hollow cantilever maintains the high Q obtained by operating in air but can still execute real-time measurements in liquid by flowing the liquid inside the cantilever. One drawback however is due to this design, as viewing and imaging the adsorbates on the channel surface is impossible.

Adsorbate rigidity is also known to influence cantilever resonance, creating a measurable shift in resonance frequency. This positive frequency shift is thought to be comparable or even larger than the mass effect [Tamayo06]. Tamayo reported a theoretical model to study the adsorbate stiffness effects on the resonance frequency of either silicon or the polymer SU-8. Calculations show opposing added mass and stiffness effects cancelling each other to produce a small response. The adsorbates myosin protein and $–SH–(CH_2)_{11}–CH_3$ alkanethiol were used for attachment to the cantilever surface. The calculated resonance frequency shift highlights the impact of the adsorbate’s Young’s modulus on the response of nanomechanical biological and chemical sensors.

This thesis shows experimental work investigating this for a range of materials, starting with a proof-of-principle study with metal layers of varying thickness in air, moving onto metal layers measured in distilled water (milliQ water). This technique is then developed to include molecular overlayers, using self-assembled alkanethiol monolayers adsorbed onto gold-coated cantilevers, finishing on antibiotic sensing.

1.4.3.2 Rheological Measurements

The application of microcantilevers to fluid mass density and viscosity measurements has received much interest over recent years [Oden96, Ahmed01, Boskovic02]. Rheological measurements, i.e. those relating to the fluid flow, are vital to many industrial and healthcare applications. The use of such measurements is commonly found in the food and beverage industries, where quantified fluid properties are essential for quality control processes [Steffe96, Cullen00]. Further applications in medicine include the measurement of blood viscosity [Dintenfass69], imperative for monitoring conditions such as stroke and hypertension. Such sensors have the advantage of being fast, miniaturized and localized, whilst only using a few microlitres (µL) of sample. This potentially offers a valuable means of fluid control whilst also helping to overcome existing measurement problems such as time consuming calibration processes, cleaning difficulties and high equipment costs.

Previous studies [Sader98, Chon00] have investigated the influence of the fluid mass density and viscosity on the resonant properties of cantilevers, and to what extent a cantilever’s length-to-width ratio (aspect ratio) influences the rheological calculations. Sader [Sader98] presented the first general theoretical model of the cantilever resonance frequency for a beam of arbitrary cross section, immersed in fluid and excited by an arbitrary driving force. Unlike previous formulations, this model quantitatively accounts for cantilever geometry and additional fluid loading, therefore allowing the beam's frequency response to be determined without prior knowledge of its material, geometry and the fluid's viscosity and density. A key assumption in this model is that the length of the beam must greatly exceed its width, i.e. it has a high aspect ratio. Experimental validation by Chon [Chon00], examined this procedure using a range of cantilevers, each of varying dimensions, immersed in acetone, water, CCl_4 and 1-butanol. An error of ≤10% was found for aspect (length : width) ratio ranges of 4 – 14.

Microcantilever measurements of Newtonian fluids demonstrated that a sensor measuring several parameters simultaneously can discriminate between density and viscosity effects [Ghatkesar08]. These parameters were: peakfrequency; eigenfrequency and damping due to the surrounding liquid. The sensor was found to be sensitive to liquid properties with a resolution of 1.5% in viscosity and 0.06% in density. Results here indicate that the effect of viscosity on the eigenfrequency cannot be neglected, even at the higher oscillatory modes. A further observation from the work is that density changes contributes to frequency shift, which increases with mode number, whereas Q is unaffected. Contrary to previous papers [Chu63, Elmer97], Ghatkesar *et. al.* demonstrated that the viscosity contributions to changes in the cantilever's effective mass occur even at higher frequencies.

Whilst cantilever-based rheological measurements have been performed on laboratory-made solutions, they have not been applied to commercially available drinks. To demonstrate their potential for real-time drinks analysis, density and viscosity measurements have been carried out on a range of commercial drinks, which is outlined in chapter six of this thesis Using this data, alcohol content can be determined. Finally, details regarding the validity of current theory on more viscous liquids, using aqueous glycerol solutions at differing concentrations are also discussed. The influence of aspect ratio in influencing measurement accuracy is also investigated.

1.5 Summary

Cantilever sensors are well recognized as a powerful and extremely sensitive platform for chemical and biological sensing. Their ability to provide an improved dynamic response, sensor miniaturisation, high precision and consistency offers cantilevers a distinct advantage over other more customary sensor techniques. These unparalleled strengths, coupled with opportunities for large scale fabrication, make cantilevers a highly desirable tool in the field of chemical and biological sensing.

A further distinct advantage offered by cantilevers, particularly those operating in dynamic mode, includes the possibility of the sensing parameters resonance frequency and quality factor to provide simultaneous, complimentary data regarding interactions of the sensor with their environment and adsorbate effects [Grüter10]. By exploiting this, adsorbate mass and stiffness effects can be determined for a range of adsorbate systems operated in both air and liquid.

Cantilever’s application in the study of physisorption and chemisorption processes is also well established [Patel98, Li07]. A further advantage to microelectrical mechanical systems (MEMS) platforms is their ability to operate in gas, vacuum and liquid. Despite significant damping effects occurring in liquid, experiments under clinically and physiologically relevant conditions have given new insights into a wide range of reactions, including DNA hybridisation [Fritz00] and detection of cell mass [Ilic01].

1.6 Thesis Overview

This thesis focuses on the developing the understanding of resonant cantilever sensing, primarily aiming to disentangle different adsorbate effects on the cantilever response. The investigation begins with metallic thin film model systems, moving on to alkanethiol self-assembled monolayer systems, and developing this with antibiotic detection using vancomycin. The application of cantilevers to measure fluid mass density and viscosity is also investigated. To this end, my thesis is structured as follows:

Chapter two gives an overview of the theory behind cantilever sensor response, including stiffness and stress effects on the cantilever beam, and how analysis of the sensor response becomes more complex when the beam is operated in fluid.

Chapter three details the experimental procedures used. This contains information regarding the types of cantilever sensors, functionalisation and deflection read-out techniques applied in this research.

Chapter four details initial investigations into disentangling adsorbate mechanical and mass effects on nanomechanical resonators. In this case, nm-thin metallic films are evaporated onto to the cantilever surface, with the beam then being oscillated in air. Previous theoretical work has predicted rigidity effects to counteract those of added mass, further complicating the interpretation of the sensor response. It is therefore highly desirable to investigate the nature of this interaction, for example, whether one effect dominates the sensor response.

Chapter five develops results from chapter four, now oscillating the cantilever in liquid. This begins with a model system of nm-thick metallic films, extending the system to molecular coatings of self-assembled monolayers, and finally antibiotic detection via vancomycin-mucopeptide complexes. Interpretation of the sensor response is now made more complex, due to an increase in effective cantilever mass from the mass density of the surrounding fluid.

Chapter six describes cantilever application in determining fluid mass density and viscosity, first in model solutions, and then extended to commercially available alcoholic beverages. The application of cantilevers in determining the drink’s alcoholic content is also presented.

Chapter seven is the concluding chapter of this thesis, and summarises key findings and scope for future development.

An appendix is also included, detailing the resonance frequency and quality factor data, along with the Mathematica procedures used in analysis.

CHAPTER 2

Theory

2.1 Chapter Overview

Over the last 20 years, cantilevers have been used in Atomic Force Microscopy (AFM) to study the topography of non-conductive surfaces [Binnig86]. This is due to their high sensitivity in measuring surface forces, allowing the sensing and measurement of various mechanical properties [Finot08]. Cantilevers are flexible, being capable of elastic deformation without breaking. This property establishes the cantilever as the sensor unit, whereby tiny cantilever movements due to molecular interactions occurring on the cantilever surface can be measured.

This chapter details the theory behind cantilever sensing. This begins with the description of static deflection investigations by Stoney [Stoney09], where he studied effects of surface stress in creating curvature of a beam. This is followed by discussion into how such effects influence beam stiffness. A simple harmonic oscillator model is then presented, analogous to a beam operating in dynamic mode. Discussion ends with consideration as to how the surrounding medium influences sensor response analysis.

2.2 Surface stress in cantilever bending

Stress in a thin film on a flexible substrate induces curvature of the substrate, and is an essential property of a solid surface that has been widely studied [Stoney09]. If the in-plane forces acting on the cantilever surface are repulsive, the cantilever surface expands, producing a compressive surface stress. This will in turn induce downward cantilever bending. Oppositely, attractive forces will cause the cantilever surface to contract, giving an upwards bending of the beam and a tensile surface stress. As surface stress is a central principle of the cantilever technique, it is important to gain a more theoretical understanding as to its nature.

2.2.1 Stoney Equation

A convenient method to study stress in thin films is to deposit these films on to a flat substrate and observe the curvature of the substrate due to the stress in the film. In 1909 Stoney derived a relationship between adsorption induced surface stress and the radius of curvature of a thin substrate [Stoney09]. Cantilever deflection, Δx, is related to applied stress, σ, by the Stoney Equation, Equation 2.1

$$\Delta x = \frac{3\sigma(1-v)}{E_c}\left(\frac{L}{t_c}\right)^2 \quad , \qquad 2.1$$

where v is the Poission ratio and describes the ratio of transverse contraction strain to longitudinal extension strain in the direction of stretching force. E_c, l and t_c are the cantilever's Young's Modulus, length and thickness respectively. A first requirement for application of the Stoney Equation is that the substrate is thick compared to the thickness of the film, but still thin enough for it to bend upon stress in the film. A second condition for application of Equation 2.1 is that the film is in a state of plane stress, i.e. in the plane of the film, the stress is directionally independent.

The original derivation of the Stoney Equation considered only a uniaxial cantilever bending, instead of a biaxial stress. In his 1909 paper, Stoney used a centimetre-scaled steel ruler and measured its deformation upon the deposition of metallic thin films. This ranged from 0.005-0.03mm [Stoney09]. Usually the substrate is orders of magnitude thicker than the film, leading to small and purely elastic deformation of the substrate. The surface stress difference between the upper and the lower surface of the ruler was in the range of kN/m. This is a million times larger than the mN/m sensitivity readily achieved today.

2.2.2 Effect of Surface Stress on the Stiffness of Cantilever Beams

Measurements over the past 30 years have indicated that surface stress can significantly affect the stiffness of microcantilever beams [Lagowski75, Chen95, Dorignac06]. In resonant cantilever sensing, stiffness effects on resonance frequency can be comparable to mass effects [Tamayo06].

In a study by Lachut and Sader [Lachut07], the question was asked: what is the relationship between strain-independent surface stress change and the stiffness of cantilever plates? The study considered a rectangular cantilever plate under a uniform and isotropic strain-independent surface stress loading on both faces, i.e., σ_s^+ and σ_s^- on upper and lower faces, respectively. Total surface stress experienced by the cantilever (mN/m) was defined as $\sigma_s^T = \sigma_s^+ - \sigma_s^-$. The prediction of resonant frequency shift due to the strain-independent surface stress within the context of linear elastic beam theory was derived as

$$\frac{\Delta f}{f_0^{(n)}} \approx -0.042 \frac{v(1-v)\sigma_s^T}{E t_c} \left(\frac{w}{l}\right)\left(\frac{w}{t_c}\right)^2 , \qquad 2.2$$

where v is the Poisson ratio, E_c and t_c are the cantilever's Young's modulus and thickness respectively, w is the cantilever width and l its length. Details into its derivation are given in the corresponding paper [Lachut07].

Crucially, their work demonstrated that previous one-dimensional models of surface stress effects on resonant frequencies [McFarland05] violate Newton's third law. Lachut and Sader further noted that the effects of the strain-independent part of the surface stress on the resonant frequencies can only be fully understood by three-dimensional models.

2.3 Mode of Operation

2.3.1 Harmonic Oscillator Model

The natural frequency of a simple harmonic oscillator depends on both the stiffness of the restoring (elastic) cantilever beam and the mass which is being accelerated/decelerated. For a rigid mass m connected to a massless spring of spring constant k, having one end fixed whilst the other is attached to the moving mass, the fundamental resonance frequency $f_0^{(n)}$ can be approximated to

$$f_0^{(n)} = \frac{1}{2\pi}\sqrt{\frac{k}{m^*}}\,, \qquad 2.3$$

In the absence of damping, Equation 2.3 is commonly used as a starting point for the estimation of mass sensitivity of dynamic mode cantilever sensors [Oden98, Davis00, Lavrik03]. m^* is related to the total mass of the suspended part of the beam, m_b, via: $m^*=Nm_b$. N is a geometric parameter, typically 0.24 for a rectangular cantilever.

$f_{res}^{(n)}$ and the quality factor $Q^{(n)}$ are defined via the thermal noise spectrum, measured by mounting the cantilever into an atomic force microscope. This in turn produces a resonance curve, as illustrated in Figure 2.1.

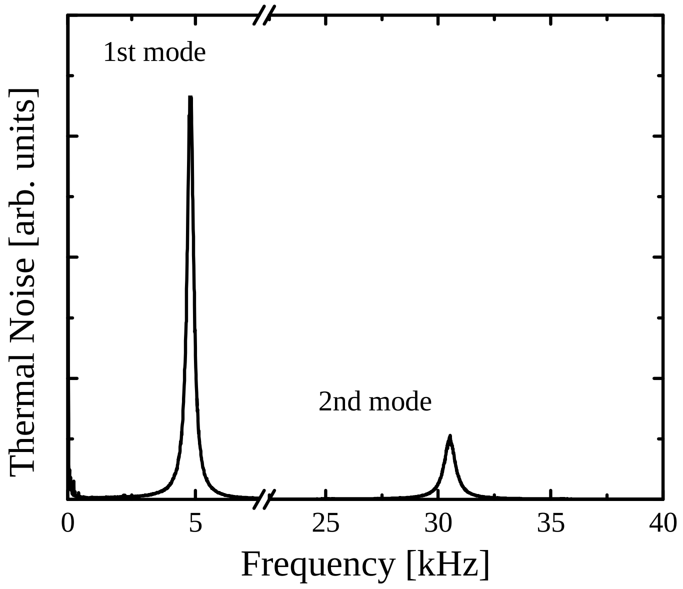

Figure 2.1 *Typical thermal noise spectrum for a cantilever oscillated in air. Example spectrum taken here is for an IBM cantilever with dimensions 500µm x 100 µm x 940nm. The first and second modes of oscillations are labelled above the corresponding peak. Typical resonance frequency and quality factor are 4.8 kHz & 17 and 30.5 kHz & 51 for the first and second modes respectively.*

The two peaks in Figure 2.1 represent different flexural vibration modes, each of which has a specific resonance frequency and mode shape. These are referred to as $n=1$, $n=2$ for the 1st and 2nd modes respectively. The mode shapes of a rectangular beam fixed at one end and free at the other end are given in Figure 2.2.

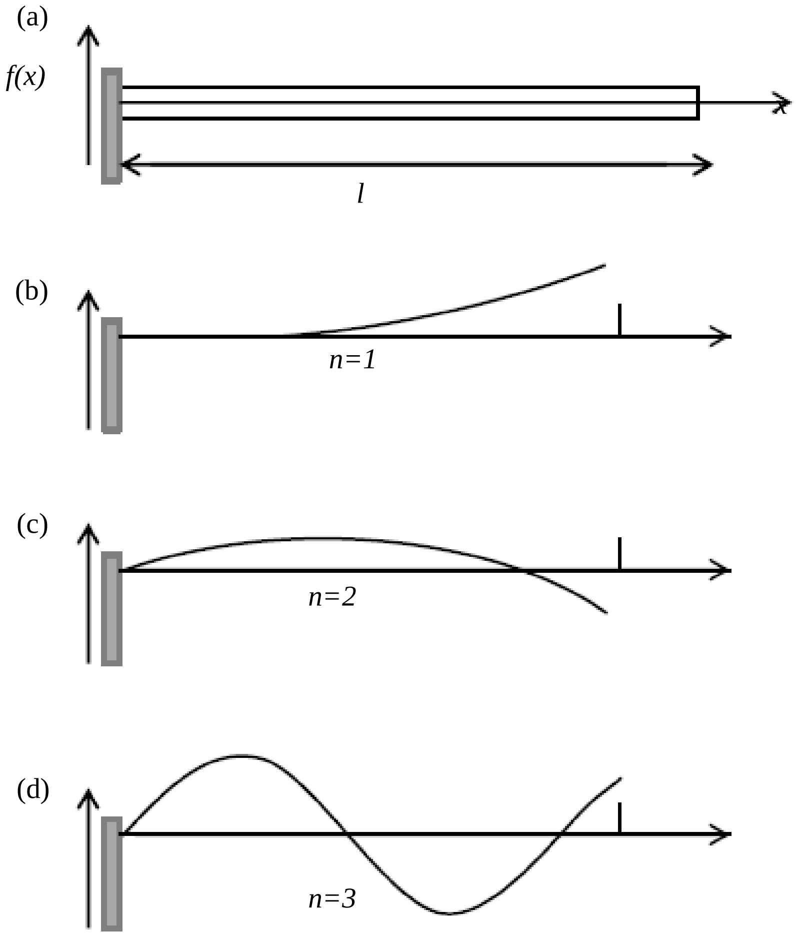

Figure 2.2 *The fundamental (a) and first three undamped natural frequencies and mode shapes of a cantilever beam (b)-(d).*

2.3.2 Dynamic Mode

When operated in dynamic mode, the cantilever is treated as a weakly damped mechanical oscillator. Mass addition can be determined via dynamic mode with a high degree of sensitivity. Upon analyte binding to the functionalisation cantilever surface, the overall cantilever mass will increase, thus creating a shift in the cantilever's eigenfrequency to a lower value. Oscillation occurs typically in the kHz or even MHz range, with examples of actuation methods including modulated laser light, magnetic and electrical actuation. Figure 2.3 depicts a cantilever operating in dynamic mode.

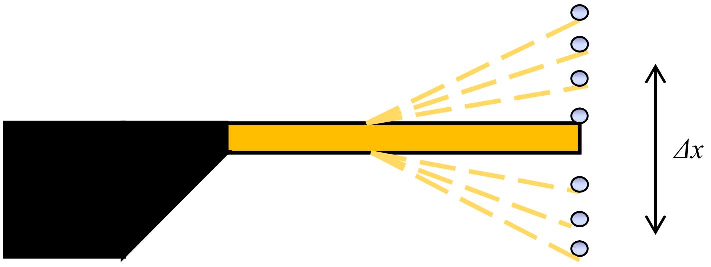

Figure 2.3 *Schematic of a cantilever operating in dynamic mode, with a mass loaded onto the apex of the cantilever. Oscillation of the cantilever at its resonance frequency permits details regarding mass changes on the cantilever surface to be accurately defined (application as a microbalance).*

Cantilever tip displacement can be assumed to be directly proportional to the force exerted on the cantilever tip. From this a simplified model of a resonating cantilever transducer can be established by applying Hooke's Law. Hooke's Law of elasticity, defined by Robert Hooke in 1660, states that, in relatively small deformations of an object, the size of the deformation or displacement is directly proportional to the deforming force or load. Under these conditions, the object returns to its original shape and size once the load has been removed. The spring constant, k, is given in Equation 2.4.

$$k = \frac{Ewt_c^{\ 3}}{4l^3} \quad , \qquad 2.4$$

where w, t_c and l define the cantilever width, thickness and length respectively, and E_c is the cantilever's Young's modulus. For silicon, this is typically E= 150 GPa [Haynes10].

Cantilevers operated in dynamic mode (as opposed to static) offer many distinct sensing advantages, including a high mass sensitivity. Mass detection of alkane thiol self-assembled monolayers (SAMs) in vacuum has been achieved with nanometer-scale resonating cantilevers, with a minimum resolvable mass of 2.7 attograms [Ilic04]. A disadvantage of cantilevers operated in static mode is their susceptibility to drift, whilst effects such as temperature, pH and buffer also need to be disentangled. This in turn complicates interpretation of the static-mode sensor response.

Through resonant cantilever sensing it is also possible to quantify the sensing parameters of resonance frequency and quality factor. These can then be used to provide simultaneous, complimentary data regarding interactions of the sensor with their environment and adsorbate effects [Grüter10]. By exploiting this, adsorbate mass and stiffness effects can be determined for a range of adsorbate systems in both air and liquid.

2.3.3 Energy Dissipation: Quality Factor

The quality factor ($Q^{(n)}$) describes the degree of damping of a microcantilever, with a sharper peak signifying lower mechanical energy dissipation. Duly, each peak in the thermal noise spectrum (Figure 2.1), will have its own value for $Q^{(n)}$. The n-th mode $Q^{(n)}$, is defined as the ratio of the resonance frequency of the *n*-th mode $f_{res}^{(n)}$ to the full width of the resonance peak evaluated at the half-maximum (FWHM = full width half maximum) of the peak.

The value of Q is dependent on the cantilever geometry, material and the surrounding medium [Sandberg05, Tamayo05]. In the absence of any medium, i.e., in vacuum, there is no viscous damping, and the quality factors are >1000. Strong viscous damping in liquids makes resonant operation of microcantilevers and consequently measurements of adsorbed mass more challenging, due to a reduction in $Q^{(n)}$. In order to take this into account, a hydrodynamic function is applied, which accommodates for the fluid damping added mass effects of the surrounding fluid. A more in-depth description of the hydrodynamic function is given in section 2.5.

2.4 Adsorbate Stiffness Effects

Added mass effects on cantilever deflection are well documented [Davis00, Lavik03, Ghatkesar04, Lavrik04, Illic05, Braun05]. Considering the mass on a spring model, it is intuitive that as added mass increases, cantilever deflection frequency decreases. However, is the situation as straightforward as this? An adsorbate possesses other physical properties – for example material stiffness and rigidity. To what extent do these influence a resonant cantilever's sensor response?

Discrepancies have been reported between the added mass calculated by the theory and the mass adsorbed on the cantilever [Chen95], attributing these to adsorption-induced surface stress effects on the resonance frequency. Research into the influence of adsorbate mechanical properties on cantilever sensors conducted by Tamayo [Tamayo06] presented a theoretical model to study the effect of the stiffness of the molecules bound to a microcantilever on the resonance frequency.

Using singly-clamped beams organic and biological adsorbed layers, their work highlighted the important influence of the adsorbates Young's modulus in the response of biological and llechemical sensors based on micro- and nanomechanical resonators. The calculations showed how the opposite contributions of the added mass and stiffness can cancel each other producing small responses. Calculation of the cantilevers flexural rigidity was given by

$$D(x) = \frac{D_0}{1 + (E_a / E_c)(t_a / t_c)} \left\{ 1 + (E_a / E_c)^2 (t_a / t_c)^4 + 2(E_a / E_c)(t_a / t_c)\left[2 + 3t_a t_c + 2(t_a / t_c)^2 \right] \right\} , \qquad 2.5$$

where $D_0 = (1/12)E_c w t_c^3$ is the flexural rigidity of the bare cantilever, *t* and *E* represent the thickness and Young's modulus of the adsorbate (*a*) and cantilever (*c*) respectively. The flexural rigidity *D* can be related to the spring constant by

$$k = \frac{3D}{l^3} , \qquad 2.6$$

This counteracting positive frequency shift produced from mechanical effects emphasizes an unsatisfactory part of micromechanical sensors, where an accurate interpretation of the sensor response must rely on both mass and rigidity of the adsorbate, which for nanometre-scale coverage can only be guessed, rather than derived from independent measurements. Experimental work to solve this problem is central to this thesis, with Equation 2.4 being applied to extracting adsorbate rigidity.

2.5 Frequency Effects of Cantilever Beams Immersed in a Viscous Medium

The frequency response of an elastic beam driven by an external driving force, is strongly dependent on the medium in which it is immersed [Chen94, Sader95, Sader98]. For example, resonance frequencies in water are lower than those in air by up to a factor of 5 for the cantilevers used in this work. Quality factors in water are of order 1, compared with 10–100 in air. The reduced resonance frequencies can be explained by the effect of fluid loading that increases the effective mass of the cantilever, while the low quality factors are due to increased hydrodynamic damping.

The principles applied in rheological analysis to determine the density and viscosity from the measured frequency response using microcantilever measurement are outlined by Sader [Sader98]. Measurements were carried out using an atomic force microscope, and cantilever oscillation followed optically. A schematic of this process is shown in Figure 2.4.

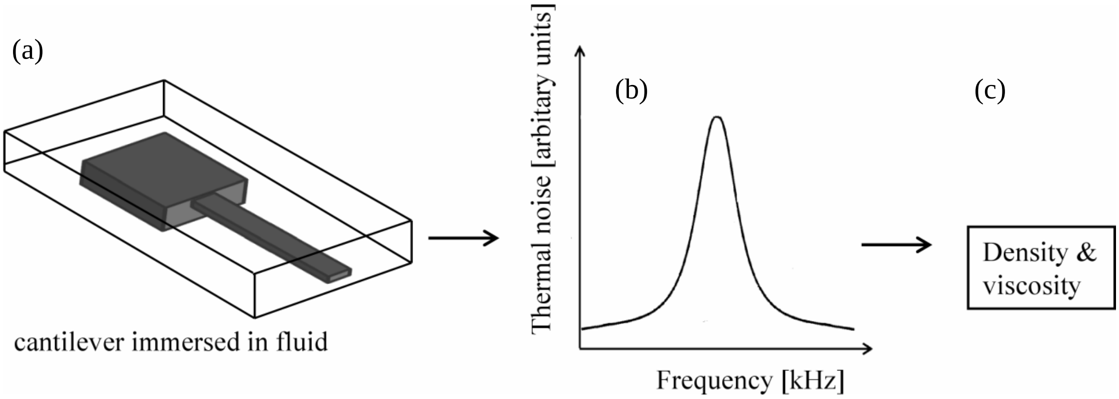

Figure 2.4 *Schematic of the measurement process for fluid density and viscosity determination. (a) The cantilever is mounted into the atomic force microscope and submerged in fluid, typically in the order of µl. Thermal fluctuations are monitored optically via a laser and PSD (Position Sensitive Detector). (b) This in turn produces a thermal noise spectrum, from which the* $f_{res}^{(n)}$ *and* $Q^{(n)}$ *are determined. (c) Changes in these values are then used to calculate the fluid's density and viscosity.*

In application of this model, several assumptions regarding the cantilever's geometry are required. These are: that it has a uniform cross-section and that its length greatly exceeds its width. For cantilevers of rectangular cross-section, it is also assumed that the width greatly exceeds the cantilever thickness. Such criteria are typically satisfied for cantilevers used in practise. The resonance frequency and quality factor are described in Equations 2.7 and 2.8 respectively.

$$f_{res}^{(n)} = \frac{f_{vac}}{\sqrt{1+\frac{\pi \rho w^2}{4\mu}\Gamma_r\left(f_{res}^{(n)}\right)}} \quad , \qquad 2.7$$

$$Q = \frac{\frac{4\mu}{\pi\rho w^2} + \Gamma_r(f_{res}^{(n)})}{\Gamma_i(f_{res}^{(n)})} \quad , \qquad 2.8$$

where $f_{vac}^{(n)}$ is the vacuum resonant frequency of the cantilever, w is its width, ρ_m is the density of the surrounding fluid, and μ is the mass per unit length of the cantilever beam. For the cantilevers, $\mu = \rho_c w t_c$, where ρ_c is the density of the cantilever (typically the density of Silicon, which is 2330 kg/m^3 [Haynes10] and t_c its thickness. Γ_r and Γ_i are the real and imaginary components of a hydrodynamic function, as defined by [Sader98].

$$\Gamma_{rec}(f) = \Omega(f)\Gamma_{circ}(f) \ , \qquad 2.9$$

where *rec* and *circ* denote rectangular and circular respectively. The correction function $\Omega(f)$ is computed using a non-linear least-squares fit over the range $\text{Re} \in [10^{-6}, 10^4]$ as a function of $\log_{10}(\text{Re})$. The Reynolds number Re is the ratio of ratio of inertial to viscous forces. Γ is dependent on the cross-section geometry of the cantilever and the surrounding fluid's density and viscosity [Sader98]. Calculations are carried out using Mathematica (Wolfram Research Inc., IL)

The real part of the hydrodynamic function describes the inertial loading (added mass) onto the beam, which the oscillating cantilever needs to displace due to the mass density of the surrounding medium. The imaginary part of the hydrodynamic function accounts for the strong damping of the cantilever vibration due to the surrounding fluid. It is this damping which leads to the low quality factors as seen from cantilevers oscillating in fluid. The following expressions for the real and imaginary parts of $\Omega(f)$, detailed in Equations 2.10 and 2.11 respectively, are produced from the Sader 1998 viscous model [Sader98].

$$\tau = \log_{10} RE$$

$$\Omega_r(f) = (0.91324 - 0.48274\tau + 0.46842\tau^2 - 0.12886\tau^3 + 0.044055\tau^4 - 0.0035117\tau^5 + 0.00069085\tau^6)(1 - 0.56964\tau + 0.48690\tau^2 - 0.13444\tau^3 + 0.045155\tau^4 - 0.0035862\tau^2 + 0.00069085\tau^6)^{-1} \qquad 2.10$$

$$\Omega_i(f) = (-0.024134 - 0.029256\tau + 0.016294\tau^2 - 0.00010961\tau^3 + 0.000064577\tau^4 - 0.000044510\tau^5)(1 - 0.59702\tau + 0.55182\tau^2 - 0.18357\tau^3 + 0.079159\tau^4 - 0.014369\tau^2 + 0.0028361\tau^6)^{-1} , \qquad 2.11$$

Calibration of the cantilever is needed in order to obtain $f_{vac}^{(n)}$ and t_c. As these quantities are unknown, an additional calculation is required using the $f_{res}^{(n)}$ and $Q^{(n)}$ measured in a known medium. This is typically air, as their density and viscosity are known, ρ_m = 1.18 kg m^{-3}; η = 1.86 x10^{-5} kg m^{-1} s^{-1} [Haynes10]. From Equations 2.7 and 2.8, the following equations for the vacuum frequency and linear mass density can be attained [Boscovic02]

$$f_{med}^{(n)} = f_{vac}^{(n)}\left(1 - \frac{\pi\rho_{med}w}{4\rho_c t_c}\Gamma_r(w, f_{med}^{(n)}, \rho_{med}, \eta\right)^{-1/2} , \qquad 2.12$$

$$\mu = \frac{\pi p w^2}{4}(Q\Gamma_i f_{res}^{(n)}, w) - \Gamma_r(f_{res}^{(n)}, w)) \qquad 2.13$$

2.6 Summary

The theoretical background necessary to further investigate and develop the application of resonant cantilever sensing has been discussed. Key equations which will be used in experimental analysis are outlined, along with how these have been previously applied. Resonant behaviour of the cantilever is first described, along with the harmonic oscillator model which accompanies this. Discussion of previous work and theory surrounding adsorbate stiffness effects show that this model is not as simple as initially assumed, with such mechanical properties counteracting added mass effects. The situation is further complicated when operating the cantilever in liquid, as fluid damping and added mass effects now influence cantilever resonance.

By applying the equations outlined in this chapter, we develop and test a procedure to disentangle this complex sensor response, aiming to simultaneously measure both mass and elastic properties of metal and molecular adsorbates. This would turn an apparent disadvantage of resonant sensors into an impressive and unique asset, enabling them to measure more than mass alone and offering a new method of adsorbate detection.

CHAPTER 3

Materials and Experimental Methods

3.1 Cantilever Instrumentation

Measurements in this thesis were carried out using a selection of tipless cantilevers, each with varying aspect ratio (length : width), thickness and spring constant. The geometries and flexural properties of these are outlined in Table 3.1, with a schematic of a one-end clamped cantilever illustrated in Figure 3.1.

Supplier Details	**Length [µm]**	**Width [µm]**	**Thickness [nm]**	**Aspect Ratio [*l* : *w*]**	**Material**	**Spring Constant [N/m]**
(a) IBM Rüschlikon Research Laboratories, Switzerland	500	100	940	5:1	single crystal Si(100)	0.03
(b) MikroMasch, Tallin, Estonia	350	35	1000	10:1	single crystal Si(100) n-type Si (phosphorous-doped)	0.05
(c) Bruker Probes, Santa Barbara, USA	400	30	2000	13:1	single crystal Si(100) n-type doped Silicon	0.16
(d) (Ultrasmall cantilevers) IBM Rüschlikon Research Laboratories, Switzerland	20-35	4	200	5:1-8:1	single crystal Si(100)	0.05-1

Table 3.1 *Outline of the cantilever dimensions, materials and spring constants used in experimental work, along with manufacturers details.*

Cantilevers *(d)* in Table 3.1 describe the FIB tailored beams, used to study the effects of metal layer adsorption onto the cantilever surface (Chapter 4). Further description into why and how tip removal is conducted can be found in section 3.1.1 of this chapter. As beam geometry is known to influence cantilever sensitivity – smaller, thinner beams are desired for maximum sensitivity - such cantilever tailoring could be applied to further investigate the limits of cantilever mass sensitivity. By precise cutting of the cantilever beam via FIB microscopy, one may be able to produce cantilevers with specific geometric properties. Such work offers scope for further investigation into the capabilities of cantilever sensors.

CHAPTER 3. MATERIALS AND EXPERIMENTAL METHODS

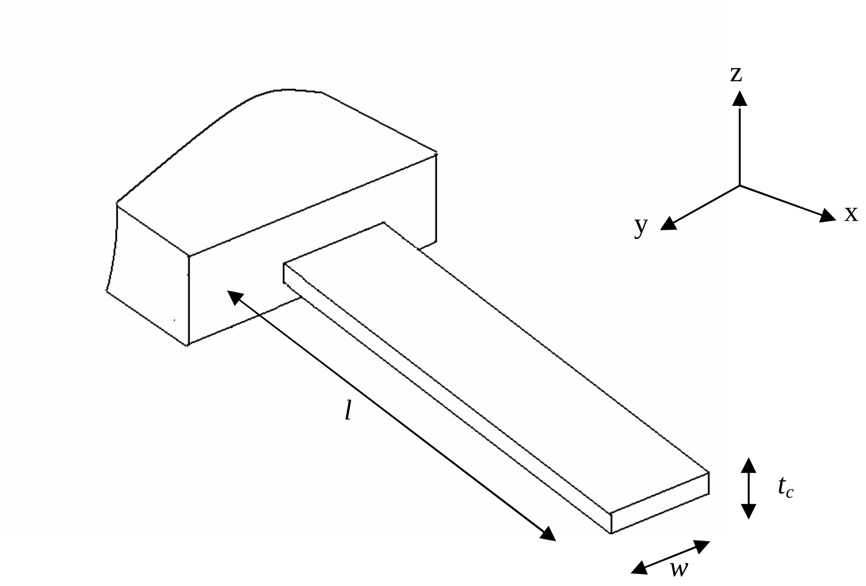

Figure 3.1 *Schematic of a rectangular cantilever, connected to a supporting rigid chip body, with dimensions and coordinate system. The origin of the coordinate system is at the centre of mass of the beam cross-section at its clamped end.* l, w, t_c *represent the cantilever's length, width and thickness respectively.*

Scanning Electron Microscopy (SEM) images of the IBM, MikroMasch and Bruker probes are shown in Figure 3.2.

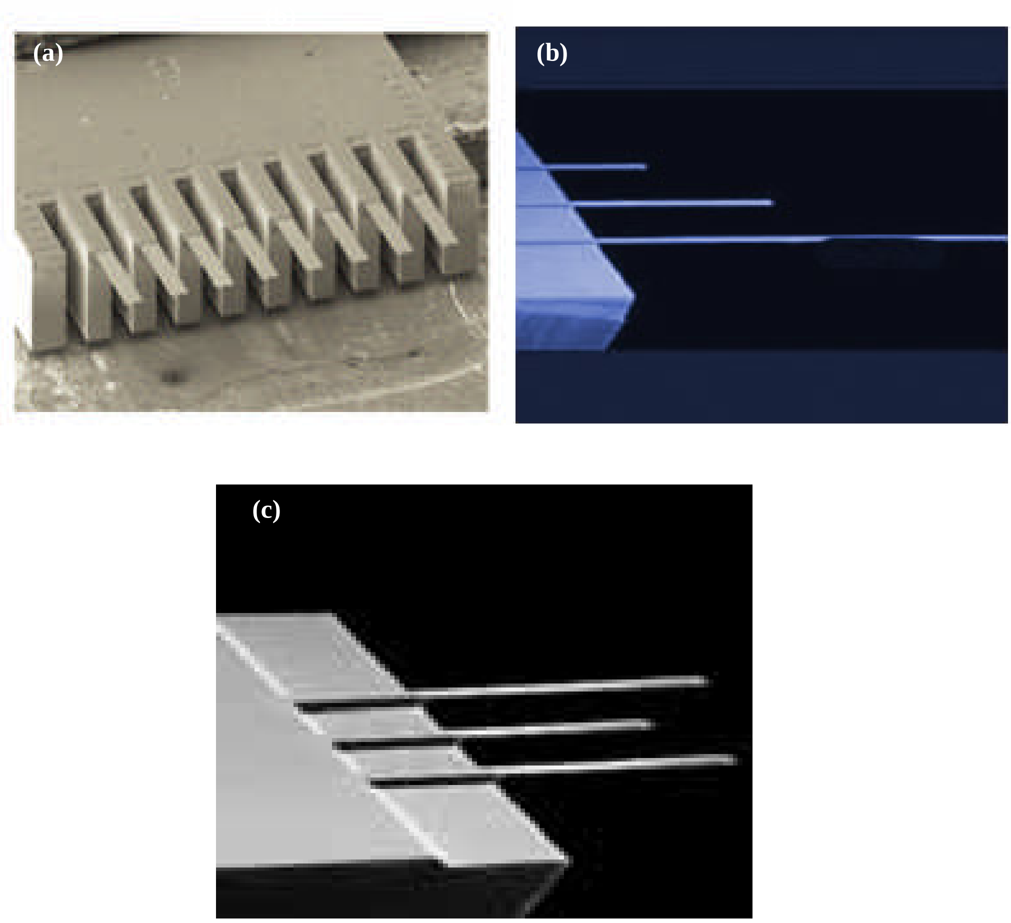

Figure 3.2 *SEM images of the (a) IBM, (b) MikroMasch and (c) Bruker cantilever probes. Images are taken from the manufacturer's website. See Table 3.1 for each cantilever's corresponding dimensions and properties.*

Due to the distance between each cantilever beam, and each beam being anchored to a rigid chip body, the cantilevers are considered mechanically decoupled from one another. For example, in the larger IBM cantilevers (Figure 3.2(a), Table 3.1(a)), the distance between the centres of each cantilever is approximately 250µm. This parallel arrangement of the cantilevers aids time-multiplexed measurement of surface stress changes on multiple cantilevers with differing surface coatings under similar experimental conditions.

The ultrasmall (20-35µm × 4.0µm × 280 nm) [Yang05] IBM cantilevers were originally manufactured for AFM imaging applications, with a tip at the free end, as illustrated in Figure 3.3.

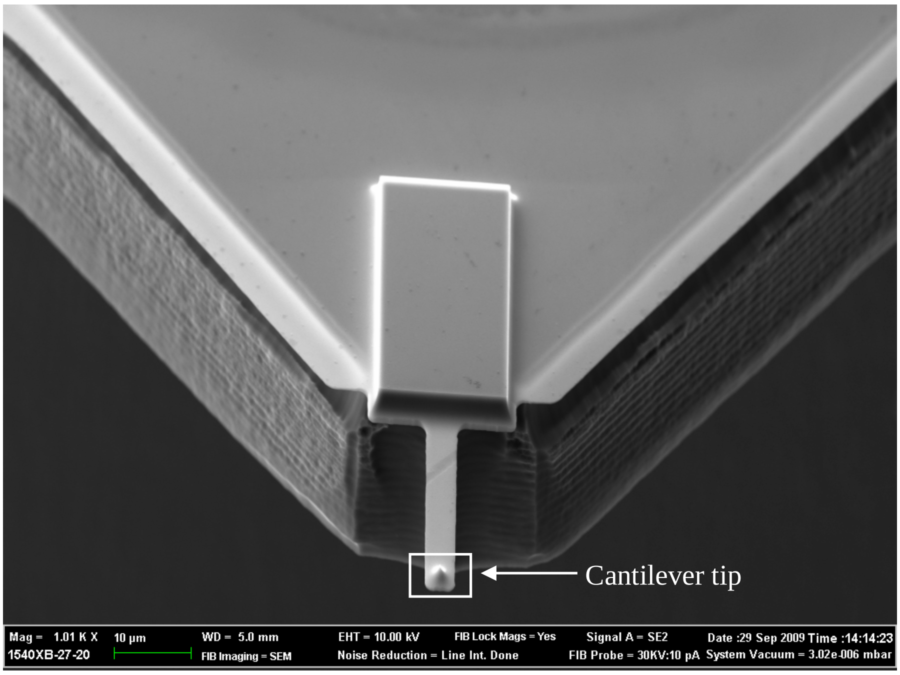

Figure 3.3 *Scanning Electron Microscopy (SEM) image of the ultrasmall IBM cantilevers, with the tip visible at the cantilever apex. See Table 3.1(d) for details of the cantilever's dimensions and properties.*

3.1.1 Cantilever Tip Removal

Any additional mass at the end of the cantilever strongly influences the sensitivity of the sensor response to adsorbed mass, and therefore decreases the frequency shift. This is undesired, as in order to draw an accurate comparison between $\Delta f_{res}^{(n)}$ of cantilevers with or without a tip, a correction factor needs to be introduced, further complicating analysis. The effect of this added mass on the cantilever's frequency shift is dependent on cantilever length and shape, being more prominent for shorter beams. Tip removal was therefore necessary in the case of these cantilevers, and was carried out using an XB1540 Focussed Ion Beam microscope (FIB) (Carl Zeiss, Jena, Germany).

The FIB microscope operates following similar principles to the SEM, in that a beam of charged particles is scanned across a sample, and the resultant signals at each position are plotted to form an image. However, in FIB the charged particle beam consists not of electrons, but ions, which are typically positively charged. The first FIB systems based on field emission technology were developed by Escovitz [Escovitz75], and later expanded on by Seliger [Seliger79] introducing an FIB based on a liquid-metal ion source (LMIS). In the 1980s, the versatility of LMIS instruments, combined with the shrinking dimensions of very large scale integration (VLSI) circuits, led to the use of FIB in semiconductor manufacturers, resulting in a rapid increase in the number of FIB applications.

Operation of the FIB begins with a liquid metal ion source, where typically a reservoir of Gallium (Ga) is positioned in contact with a sharp Tungsten (W) needle. A high extraction field ($>10^8$ V/cm) is then required to pull the liquid Gallium into a sharp cone with a radius between 5–10 nm. It is this beam of ions which are used to cut through the cantilever and remove the tip. Gallium is advantageous to use for two reasons: (i) it has a low melting point, making it exist in a liquid state near room temperature, and (ii) it can be focused to a very fine probe size (<10 nm in diameter). This small probe size is advantageous in milling, as controlled beam movement is required. A further benefit of Gallium in milling comes from its smaller penetration depth, when compared to electrons, also aiding fine movement and positioning.

FIBs typically operate with an accelerating voltage between 5 and 50 keV. By controlling the strength of the electrostatic lenses and adjusting the effective aperture sizes, the probe current density (and therefore beam diameter) may be altered from tens of picoamperes to several nanoamperes, corresponding to a beam diameter of approximately 5 nm - 0.5 mm). A schematic diagram of the LMIS and FIB column is illustrated in Figure 3.4.

Once the tip has been removed, the cantilevers can be used in exactly the same way as other tipless cantilevers. An image of a typical cantilever post tip-removal is shown in Figure 3.5. As the length of the cantilever is altered as a result of tip removal, it is essential to measure the new cantilever length. This is achieved whilst the cantilever is mounted in the FIB.

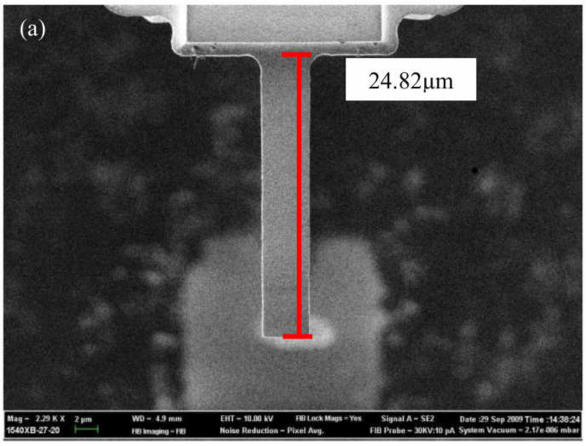

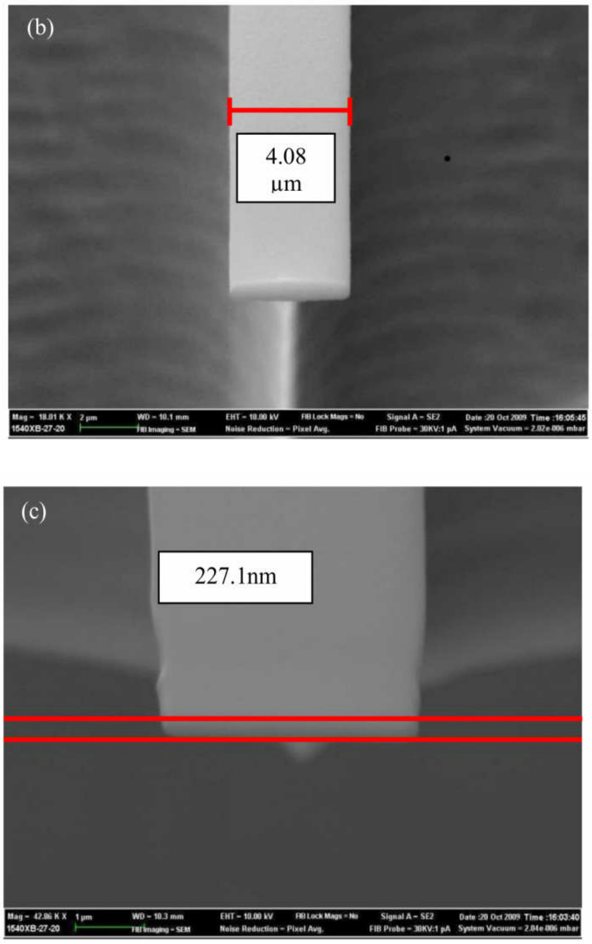

Figure 3.5 *SEM images of length (a), width (b) and thickness (c) measurements of the ultrasmall IBM cantilevers after tip removal using ion beam milling. After tip removal, the cantilever length is reduced, making it essential to gain an accurate determination of the new dimensions.*

3.2 Cantilever Functionalisation

In order to work effectively as sensors, cantilevers need to be coated with a highly specific sensing layer, being able to recognize target analytes in a lock-and-key manner, or at least partially specific.

This in turn means that any sensor response from several cantilevers yields a characteristic response pattern for the desired analyte.

3.2.1 Electron Beam Evaporation

Electron Beam Evaporation (e-beam evaporation) comes under a larger category of Micro-Electro-Mechanical Systems (MEMS) processes known as Physical Vapour Deposition (PVD). In the evaporation process, the metal to be deposited is heated under high vacuum, causing it to vaporise, and later condense onto the cantilever surface.

Different thicknesses of either gold (deposition rate: 0.09 nm/sec) or copper (deposition rate: 0.01 nm/sec) were deposited on the cantilevers. For the fixation of the gold layer, an additional titanium layer was evaporated (deposition rate: 0.03 nm/sec). A low evaporation rate was chosen for copper in order to create a layer affecting only mass but not stiffness of the cantilever. Such a rate promotes island growth, rather than a homogeneous coverage. Isolated, dilute islands can be expected to cause a relatively smaller change in the rigidity of the cantilever, as long as they do not touch. Once these islands cover a substantial part of the beam and coalesce, the adsorbate begins to behave as a homogeneous overlayer, with elastic properties approaching that of the bulk material.

To prevent contamination of the target metal and ensure a clean evaporation path, the evaporation process takes place in a vacuum chamber ($<10^{-5}$ Torr base pressure). At such low pressures, the mean free path of the evaporated species is long enough for it to condense onto the cantilever surface without colliding with any residual gas molecules. An important experimental parameter is therefore the evaporation distance, which is approximately 100mm (Edwards

Vacuum). In e-beam evaporation, a high kinetic energy beam of electrons is directed at the target material. Upon impact, the high kinetic energy is converted into thermal energy, heating up and evaporating the metal, on the premise that the heat produced exceeds the heat lost during the process. A schematic of inside the evaporation chamber is shown in Figure 3.6.

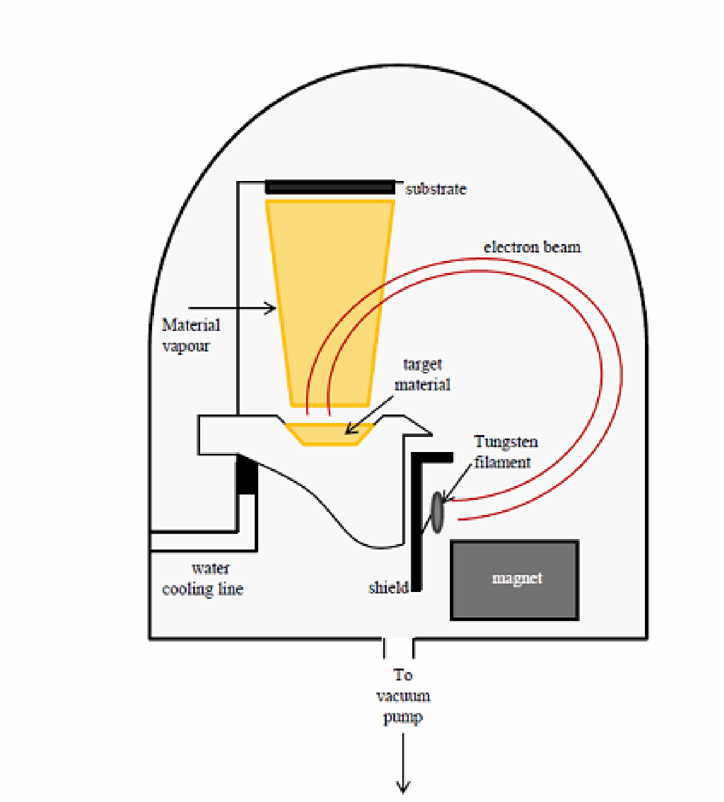

Figure 3.6 *Schematic of the electron-beam evaporation chamber*

In deflection measurements, it is preferential to have an uncoated (reference) cantilever on the same array. This is in order to gain an accurate understanding of adsorbate addition effects, allowing for simultaneous measurement of the reference cantilever aligned in the same array as the metal-coated cantilever. For the coating system outlined, this is achieved by placing a microscope cover-slip over the cantilevers to be left uncoated, before fixing the array into the evaporation chamber of the e-beam evaporator.

It is important to note that a homogenous metal-coating is assumed via e-beam evaporation. However this is not often the case, with the surface morphology in reality being rougher than the assumed smooth cantilever surface. This in turn will increase the surface area of the cantilever, meaning more alkanethiol molecules anchored onto the gold surface. Furthermore, the mass of the gold layer may not be exactly as expected, as areas of thicker or thinner metal coverage may exsist on the beam. Metals with smaller grain size will show a higher lateral Young's modulus compared with those with high grain sizes, as materials with small grains possess a higher concentration of grain boundaries. When under deformation, the small grains act as obstacles for the slipping of atomic layers.

3.2.2 Cantilever Cleaning

Before proceeding with deflection measurements for the gold-coated cantilevers, it was important to thoroughly clean the beams in order to remove any dirt or particulates which may interfere with evaporation. Cleaning the cantilevers also helps to ensure any unwanted particulates are removed from the cantilever surface, as any additional mass may affect frequency measurements and reduce calculation accuracy. The arrays were first cleaned with Piranha Solution (at ratio 1:1 H_2SO_4 and H_2O_2) for 20 minutes, and rinsed thoroughly in deionised water. Following this, the beams were immersed into a solution of H_2O:H_2O_2:NH_4OH (at ratio 1:1:1) for 10 minutes, and rinsed once more with deionised water. Rinsing in ammonia is necessary to ensure all H_2SO_4, H_2O_2 and unwantedparticles are removed from the cantilever surface, ensuring the cantilever surface is as clean and smooth as possible for evaporation. Finally, the arrays were rinsed with pure ethanol and dried on a hotplate at 70 °C.

3.2.3 Capillary Functionalisation

In the case of further functionalisation with self-assembled monolayers, gold-coated cantilevers were incubated into dimension matched capillaries filled in a random order of thiol chain length and terminating group [Sushko08]. The inner diameter of the glass capillaries is approximately 150µm diameter, allowing for the IBM cantilevers (100µm wide) to fit inside. This is illustrated in Figure 3.7.

Cantilever chip body

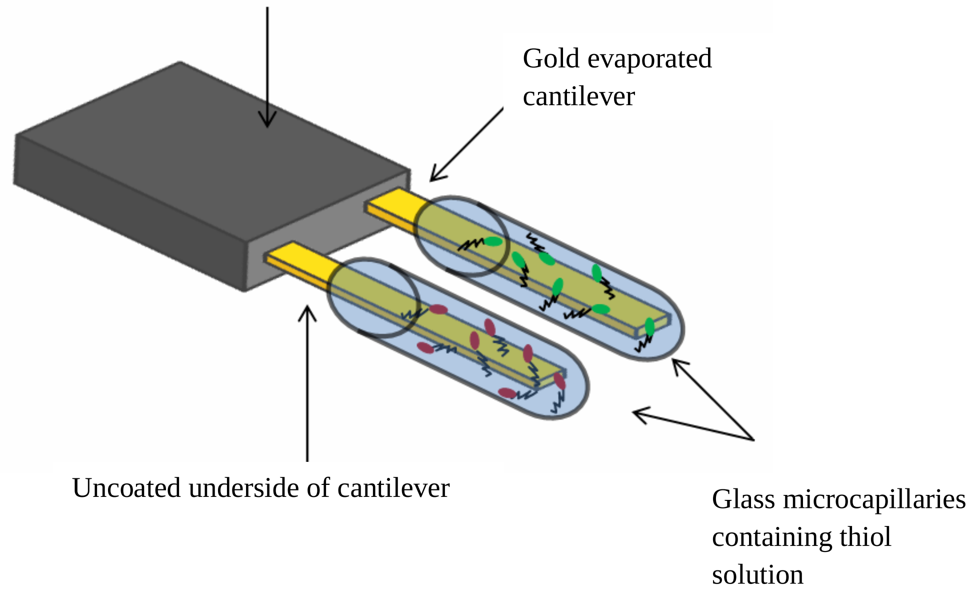

Figure 3.7 *Schematic of cantilever functionalisation via glass microcapillaries containing varying thiol solutions, arranged across cantilevers in a random order. Figure depicts two cantilever beams, however the set-up was repeated over arrays of eight cantilevers.*

3.3 Measurement Systems

Several read-out systems have been applied in the detection of cantilever bending [Raiteri01, Lavrik04, Dueck10] and will be reviewed in this section. Operation of any cantilever sensor depends on real-time deflection measurements with at least nanometre accuracy. For that reason, a vital part of any cantilever sensor is the read-out method. Desired sensitivity, speed of alignment, robustness and ease of read-out all influence which method is chosen.

Cantilever measurements were performed using three different optical detection set-ups, depending on cantilever geometry and surrounding environment. The systems applied were: JPK Nanowizard I; Fabry-Perot interferometery and Veeco Scentris.

3.3.1 JPK Nanowizard I

For the larger IBM, MikroMasch and Bruker probes, the cantilever is mounted in a commercial atomic force microscope (Nanowizard I, JPK Instruments, Berlin, Germany) and, if required, submerged in 100-200 µl of liquid. The resonance behaviour is then determined from the Fourier spectrum of the thermal noise of the cantilever. Dynamic mode measurements are performed on the JPK, as opposed to the Veeco Scentris. This is due to the Scentris having a low pass filter at 5kHz to remove higher frequency signals for the static mode DC measurements, cutting off the frequencies on the Scentris.

The optical lever technique is the original read-out method first applied in AFM [Meyer88] and later successfully applied to cantilever sensors [Gimzewski94]. This method is the most commonly used read-out technique due to its relative simplicity and high lateral resolution. A laser beam is focussed onto the free end of a cantilever and reflected onto a position sensitive detector (PSD). Upon cantilever bending, the position of the laser beam on the PSD changes, which can be measured electronically. The optical lever method was used in the cantilever experiments described in this thesis, with a schematic of its set-up illustrated in Figure 3.8.

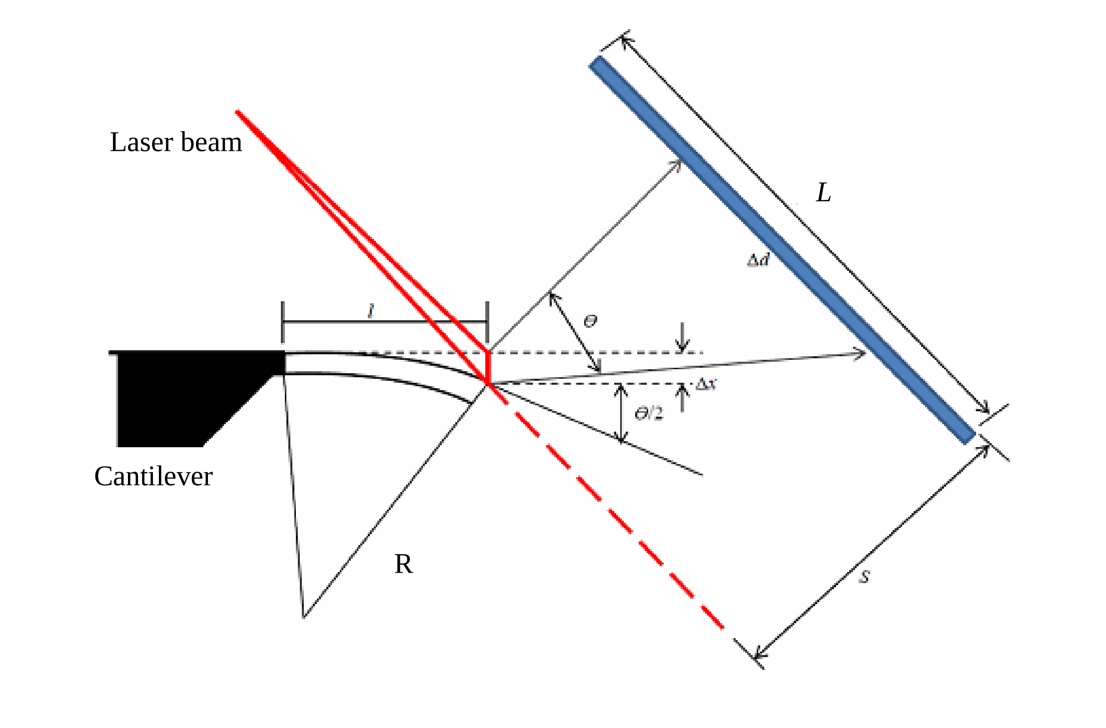

Figure 3.8 *Optical read-out technique. A laser is focused on the free end of the cantilever and reflected back onto the Position Sensitive Detector. Gold coating upon the cantilever can aid this technique by making the cantilever surface more reflective.*

Cantilever deflection (Δx) scales with cantilever dimension, making surface stress $\Delta\sigma$ in N/m an advantageous quantity to measure and compare the cantilever deflection response. R represents the radius of curvature, and provides a measure of bending. Cantilever displacement is monitored via a Position Sensitive Detector (PSD). As shown in Figure 3.8, the cantilever displacement is transformed to a displacement signal (Δd) on the PSD, with the cell transducing the light energy into an electrical signal. Cantilever motion will consequently change the laser position on the photodiode and therefore the light intensity on each cell. Prior to measurement, the laser spot is aligned in the centre of the PSD, so each segment has equal levels of illumination.

This method is highly sensitive for measuring deflection, with bending as small as a few angstroms able to be detected. The absence of electrical connections to the cantilever, linear response and its reliability are all important advantages of this technique. However, applications of cantilever sensors with optical detection are limited to analysis of samples with high transparency and low turbidity.

3.3.1.1 AFM Imaging

For gold and copper layer coatings, AFM imaging was applied to characterize the coatings. The imaging cantilever has a sharp tip (probe) at its end, which is used to scan the specimen surface. The principal modes of operation in AFM imaging are: contact, non-contact and tapping mode, with the latter technique being used in this work. Here, the probe cantilever is oscillated at or near its resonant frequency. The oscillating probe tip is then scanned at a height where it taps the sample surface. The system monitors the probe position and vibrational amplitude to obtain topographical and other property information. Optical detection via a laser beam is used to measure the resulting cantilever deflection.

The advantage of tapping the surface is improved lateral resolution on soft samples. Lateral forces such as drag, common in contact mode, are virtually eliminated.

3.3.2 Interferometric Detection

An alternative optical method uses interferometric techniques [Helm05, Wehrmeister07, Kelling09]. A fibre-optic Fabry-Perot interferometer was used to measure the thermal noise of the ultrasmall IBM cantilevers. Here, interference occurs between the partially reflecting end face surface of the fibre and the cantilever surface. For monochromatic light the intensity of the signal at the detector is dependent on the distance between the end face surface of the fibre and the cantilever surface and therefore the deflection of the cantilever.

For ultrathin, i.e. up to 150nm, and heterogeneous adsorbates, material properties significantly deviate from their bulk values. To increase the sensitivity towards such effects, ultrasmall IBM silicon cantilevers can be used. These are typically 25 µm × 4 µm × 200 nm in dimension, and their thermal noise spectra is measured via a Fabry-Perot interferometer with a <3 µm spot-size [Hoogenboom05]. For all miniaturized cantilevers, the exact dimensions in length and width were determined by scanning electron microscopy (SEM), with an example of this determination shown in Figure 3.5.

In the set-up used, a laser beam (λ=783nm) from a single-mode optical fibre is passed through a lens system, focussing the light into a 3µm spot on the cantilever. The lenses and fibre are mounted in a detector housing which can be fine-positioned along the optical axis with a piezo scanner, and aligned to the cantilever with an *xyz* piezo motor [Hoogenboom05]. An illustration of the interferometric set-up is shown in Figure 3.9.

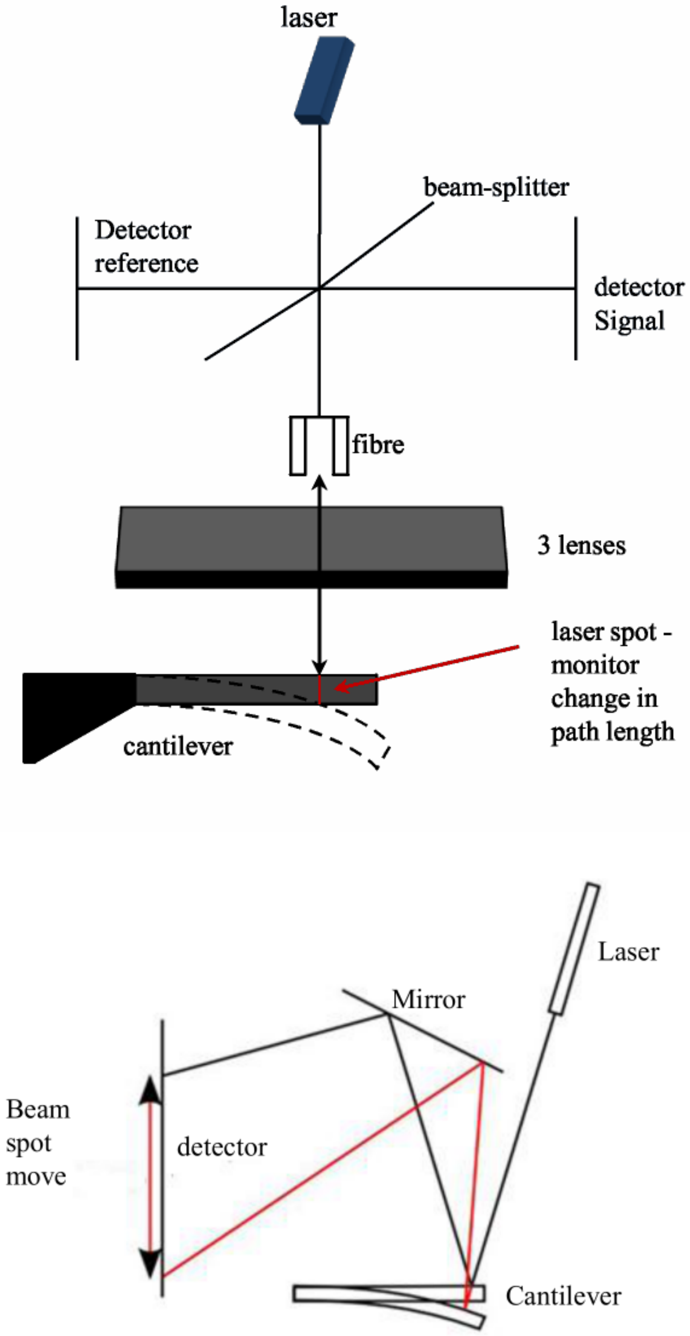

***Figure 3.9** Schematic of interferometric detection instrumentation*

3.3.3 Veeco Scentris

Cantilever deflection for thiol self-assembled monolayers [Sushko08] and vancomycin adsorption experiments were followed using a Veeco Scentris (Veeco Scentris Instruments Inc., Santa Barbara, CA, U.S.A.). This permits measurement of the absolute deflection at the free-end of each cantilever using a time-multiplexed optical detection system in different liquid environments. This was achieved using the larger sized IBM cantilevers. A schematic of its set-up is shown in Figure 3.10 [Watari07].

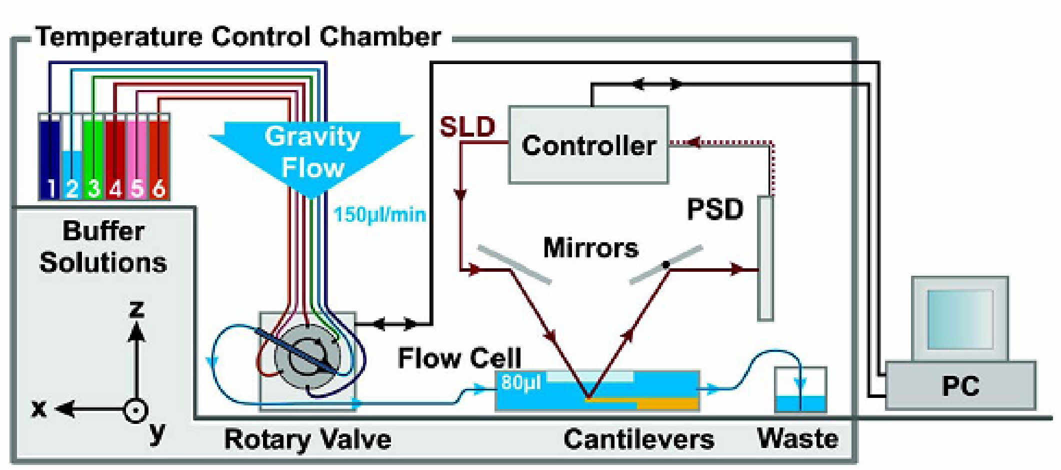

Figure 3.10 *Veeco Scentris instrument set-up. The laser beam path for optical read-out of the cantilever deflection is symbolized by red arrows. The cantilever array is depicted in yellow.*

(Figure from [Watari07]). Permission to reproduce this image has been granted by Dr. Rachel McKendry

Eight superluminous diodes (SLDs) are focused onto the cantilever tip – one SLD for each beam. This beam is then reflected off the cantilever surface and directed towards the position sensitive detector (PSD), following the optical read-out method described previously. Alignment of the laser beam onto the cantilever and then to the PSD is carried out manually, with mirrors in place to assist with this. The entire set-up is enclosed in a box in order to protect the system from changes in room temperature and to isolate the system from room light.

The functionalized cantilever arrays are inserted into a flow-through fluid cell of approximately 80µl, where it is held in position via a spring clip. As fluid flow rate can influence cantilever deflection, a constant flow rate is maintained throughout (150µl min^{-1}). Sample solutions are injected directly using a syringe pump, where the flow can be regulated and uninterrupted. Six different solutions could be used and selected with a rotary switch valve.

A preamplifier transduces the electrical currents delivered by the two electrodes of the PSD into voltages, which can be read by a data acquisition card in the recording computer. The data acquisition translates the analogue signals from the electronics into digital data which can be further processed by the PC.

3.4 Thermal Noise Spectrum Fitting Procedure

The resonance behaviour of the cantilever is determined from the Fourier spectrum of the thermal noise of the cantilever. The thermal noise spectrum can be fitted using a simple harmonic oscillator model. Due to the broadness of the peaks, different modes of oscillation are not strictly separated any more in the frequency domain. To enhance the accuracy of resonance frequency determination, each mode in the thermal noise spectrum is fitted by subtracting the fit(s) of the lower mode(s) from the experimental data. This begins with the first (fundamental) mode, then moves on to each higher mode in the thermal noise spectrum. Doing this helps prevents the tails of the lower modes from polluting the fits to the higher modes of oscillation. Fitting procedures are executed using Mathematica, (Wolfram Research Inc., IL). Acknowledgement is given to UCL PhD student Jake Stinson for devising and implementing this fitting procedure.

To begin the fit, the frequency range of the desired mode is selected, and a line is fitted to a constant. This is achieved using the following evaluation code in Mathematica: *ffit[fpeak, Q, fmin, fmax]*, where *fpeak* is an estimate of the resonant frequency, *Q* is an estimate of the quality factor, and *fmin* and *fmax* define the frequency interval over which the data is fitted. The last part should be a string, '*z0*' for mode 1, '*z1*' for mode 2 etc. The Mathematica code, along with a typical example of the fitting procedure is provided in the Appendix F.

Once the background noise has been subtracted, the following plot can be obtained, allowing for precise determination of the cantilever's resonance frequency without any interference from earlier oscillation modes (Figure 3.11).

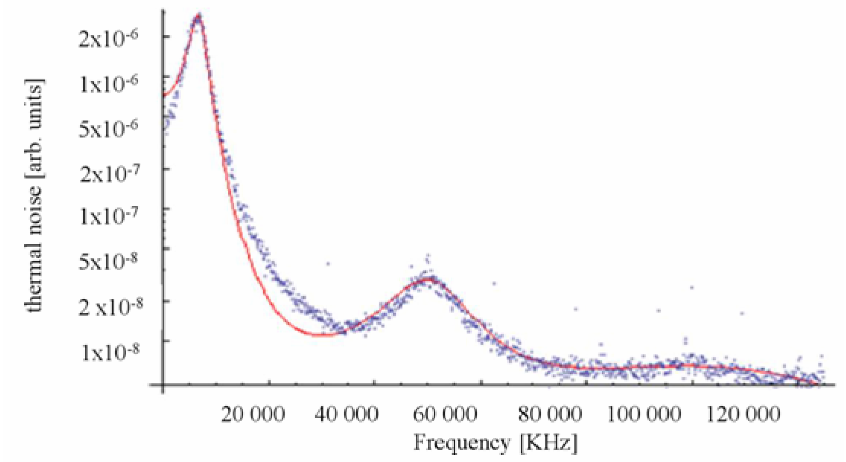

Figure 3.11 *Final thermal noise spectrum once background noise has been removed. The red line denotes the new fit, whilst the blue dots represent the experimental points.*

Resonance peaks can at times display a degree of asymmetry, or their appearance distorted; it is also possible that a 'forest' of multiple peaks is observed in the frequency scan, making spatial resolution difficult. The coupling of the excitation vibration of the incorporated oscillator and the cantilever chip can be responsible for such shaped peaks. An example of this can be seen by comparing Figure 2.1 and 3.11. The ideal case in Figure 2.1 shows a symmetrical peak once background noise and other unwanted resonance effects have been removed, and the peak averaged over the data range to create a smooth curve. In reality, thermal noise measurements produce a peak more similar to that of the blue dots in Figure 3.11, where data points are more scattered and the peak less symmetrical.

At low frequencies, all resistors suffer from conductance fluctuations, usually called $1/f$ noise because the noise power density [V^2/Hz] decreases as one over the frequency. Cantilever noise density has a $1/f$ dependence for low frequency, and merges to a constant noise density (white noise) above the $1/f$ corner frequency. The detrimental effects of $1/f$ noise can be limited by working at low temperatures, where the coefficients of thermal expansion are very small. Peaks below 3kHz can be masked due to $1/f$ noise, making it inaccessible and accurate frequency and quality factor determination not possible.

It is important to note the shift thermal noise peaks due to hydrodynamic damping. In air, the medium does not restrict cantilever oscillation and typical resonance frequency and quality factor are 4.8 kHz & 17 and 30.5 kHz & 51 for the first and second modes respectively in the IBM cantilevers described in Table 3.1(a). However, when identical cantilevers are oscillated in water, fluid damping significantly reduces $f_{res}^{(n)}$ and $Q^{(n)}$ to 5.8 & 3.3 and 18 & 5.2 for the *second* and *third* modes respectively. Note the increase in mode number here. Crucially, when operating the cantilever in liquid, measurement of the first mode peak is no longer possible due to the presence of a 'forest' of peaks close to the y-axis in the thermal noise spectrum. $f_{res}^{(n)}$ and $Q^{(n)}$determination for the proceeding modes in water is also complicated due to a sever reduction in peak amplitude. An example of this is shown in Appendix F.

CHAPTER 4

Disentangling Mechanical and Mass effects of Metallic Thin Film Adsorbates on Nanomechanical Resonators Operated in Air

4.1 Chapter Overview

Micro and nanomechanical resonators are powerful and label-free sensors of analytes in various environments. Their response, however, is a convolution of mass, rigidity, and nanoscale heterogeneity of adsorbates. This chapter discusses initial investigations into disentangling this complex sensor response, to simultaneously measure both mass and elastic properties of nanometer thick samples for cantilevers operated in air. This turns an apparent disadvantage of these resonators into a striking and unique asset, enabling them to measure more than mass alone.

I gratefully acknowledge the work of Masters Student Raphael Grüeter, a past member of Dr. Hoogenboom's research group. His invaluable input to this chapter helped form a solid and exciting basis from which I was able to begin my research. His contribution in this chapter includes: gold film evaporation of 50 and 100nm; copper evaporation of 3, 12, 20nm; corresponding thin film AFM images and thermal noise measurements. Copper 50nm evaporation, AFM measurement and imaging were completed personally.

4.2 Introduction

Due to their smallness [Li07], micro and nanomechanical resonators can detect masses of down to few atoms in vacuum [Ilic04, Yang06]. Analogous to a quartz crystal microbalance (QCM), they transduce the mass of adsorbed material into a shift of the sensor resonance frequency [Ghatkesar07]. They are sensitive to added mass and to other adsorbate-related properties such as rigidity and surface stress [Finot08]. Surface stress has been extensively exploited by measuring the static bending of cantilever sensors [Waggoner07]. On the other hand, it has only a limited effect [Chen 95, Lachut07] on dynamic properties of the resonator. The effect of adsorbate rigidity— though long known [Chen95] — has generally been neglected for such systems. Recent theoretical work, however, has predicted sizable effects of adsorbate rigidity on the measured frequency shifts [Gupta06, Tamayo06] *counteracting* the effect of adsorbed mass. This highlights a particularly unsatisfactory aspect of micro-mechanical sensors as follows: an accurate interpretation of the sensor response must rely on both mass and rigidity of the adsorbate, which for nanometer

-scale coverage can only be guessed, rather than derived from independent measurements. To solve this problem, experimental verification of a theoretical description of the dynamic sensor response [Tamayo06, Sader98] for simple model systems is first investigated. Following this, a method to deconvolve the effects of mass and rigidity on the measured frequency shifts is demonstrated. Unlike other methods [Ramos08, Ramos 2009] it does not require any added complexity to the sensor itself.

Roukes describes a first implementation of a bifurcation-topology amplifier (BTA) based on a coupled pair of nonlinear high-frequency nanomechanical resonators, actuated piezoelectrically and measured by laser interferometry at room temperature [Roukes11]. Such an approach works by inducing dynamical changes to the topology of a simple bifurcation diagram through the application of a small control signal. The study found the principles which underline BTA to be simple and generic, suggesting its applicability to a wide variety of physical, chemical, and biological systems.

Resonance frequency changes described by Tamayo are found to be location dependent. Positioning proteins near the clamped end of the beam, protein adsorption produces a positive relative frequency shift of about 1.1% in SU-8 cantilevers due to the stiffness of the adsorbates. For the silicon cantilever this was about 40 times lower. Similarly, when the proteins were located at the cantilever free end, added mass effects produced a negative relative frequency shift of 0.27% in the SU-8 cantilever and of 0.14% in the silicon cantilever [Tamayo06]. Experiments described in this chapter focus on uniformly coating the cantilever with a metal layer. As a consequence of this, such mass and stiffness effects as described by Tamayo become less pronounced. This is because the mass and stiffness effects begin to counteract one another, cancelling each other out, compared to the transduction of just a mass or stiffness event in cantilever resonance.

CHAPTER 4. DISENTANGLING MECHANICAL AND MASS EFFECTS OF METALLIC THIN FILM ADSORBATES ON NANOMECHANICAL RESONATORS OPERATED IN AIR

In order to advance our understanding of oscillating sensors, thus further developing nanomechancical sensor technology, it is important to gain a more quantitative understanding into the nature of this counteraction.. It is important to note here that such nm-thick metal layers are valid for the development to such an analytical model, whereas the biological layers will be thinner by orders of magnitude (~0.5-1nm), as discussed in Chapter 5.

4.3 Theory

The most common configuration of a micromechanical resonator is that of a rectangular cantilever clamped at one end. A homogeneous adsorbate layer will change the natural frequency $f^{(n)}$ of its n-th mode of flexural oscillation according to

$$\frac{f^{(n)}}{f_0^{(n)}} = \sqrt{\frac{D/D_0}{\rho t}} \quad , \qquad 4.1$$

where $f_0^{(n)}$ is the natural frequency of the unloaded cantilever and $\rho = \rho_a / \rho_c$ and $t = t_a/t_c$ are the ratios between the density and the thickness of the uniformly adsorbed layer (a) and the cantilever (c), respectively. D/D_0 is a function of t and of the Young's moduli of the adsorbate (E_a) and the cantilever (E_c); it describes the relative change in flexural rigidity [Tamayo06].

The quality factors $Q^{(n)}$ provide another source of information on the adsorbate properties [Sandberg05]. For pressures above 10^{-2} mbar, the cantilever $Q^{(n)}$ is determined by the surrounding medium [Yang02]. This is most useful, since the effect of the medium on both $f_{res}^{(n)}$ and $Q^{(n)}$ is known [Sader98]

$$\frac{Q^{(n)}}{Q_0^{(n)}} = (1+\rho t)\frac{\operatorname{Im}\Gamma(f_0^{(n)})}{\operatorname{Im}\Gamma(f^{(n)})} \ , \qquad 4.2$$

where $Q_0^{(n)}$ is the quality factors of the unloaded cantilever. Γ is the (known) hydrodynamic function for a rectangular beam, which depends on the frequency and the width of the cantilever, and on the density and the viscosity of the medium. Equation 4.2 is only strictly valid for $Q > 1$ and it has been assumed that the effect of the medium on $f^{(n)}/f_0^{(n)}$ is negligible (as appropriate for measurements in air). The conclusions of this chapter also hold, with some added mathematical complexity, without the latter approximation.

4.4 Methods

Metal films are used as a model system to quantitatively investigate the effect of adsorbates on the dynamic (as opposed to static) properties of cantilevers. As a first model system, gold films of variable thickness are evaporated onto an array of eight single-crystal silicon cantilevers ($500 \times 100 \times 0.9$ m^3) [Ghatkesar07] measured in air and in water at room temperature. Further details regarding these cantilevers are presented in Table 3.1, Chapter 3.

An adhesion layer of 2 nm titanium facilitates the fixation of gold to the cantilevers. All metal evaporation procedures were carried out using an e-beam evaporator (BOC Edwards A500, U.K), with the applied layer thickness determined via an internal QCM. Details regarding the evaporation process are discussed in section 3.2.1 of this thesis.

To avoid detrimental effects due to inefficient cantilever actuation, investigation focuses on the thermal noise of the cantilevers, rather than on resonance curves with external excitation. The thermal noise measurements were carried out on a commercially available atomic force microscope (JPK Nanowizard I), with deflection detected optically.

4.5 Results

4.5.1 Gold Thin Films

Figures 4.1(a) and 4.1(b) show thermal noise spectra for cantilevers without coating and for cantilevers covered with 50 and 100 nm thick gold films, all within the same array, in air and in water. Figures 4.1(c) and 4.1(d) show normalised frequency shifts $\Delta f^{(n)}/f_0^{(n)} = (f^{(n)} - f_0^{(n)})/f_0^{(n)}$ and changes in quality factors $\Delta Q^{(n)}/Q_0^{(n)} = (Q^{(n)} - Q_0^{(n)})/Q_0^{(n)}$ as determined from the thermal noise measurements, compared to the theoretical predictions for added mass only (i.e., setting $D/D_0 = 1$), for rigidity only (i.e., setting $\rho = 0$), and for the combined effect of added mass and change in rigidity (Equations 4.1 and 4.2 which is practically independent of n for the first few modes). The data are plotted as a function of added (adsorbate) mass m_a over cantilever mass m_c, as determined from quartz crystal microbalance measurements during metal evaporation and from the cantilever dimensions. This enables direct comparison of the frequency shifts for different rectangular cantilevers, even if their dimensions are not the same.

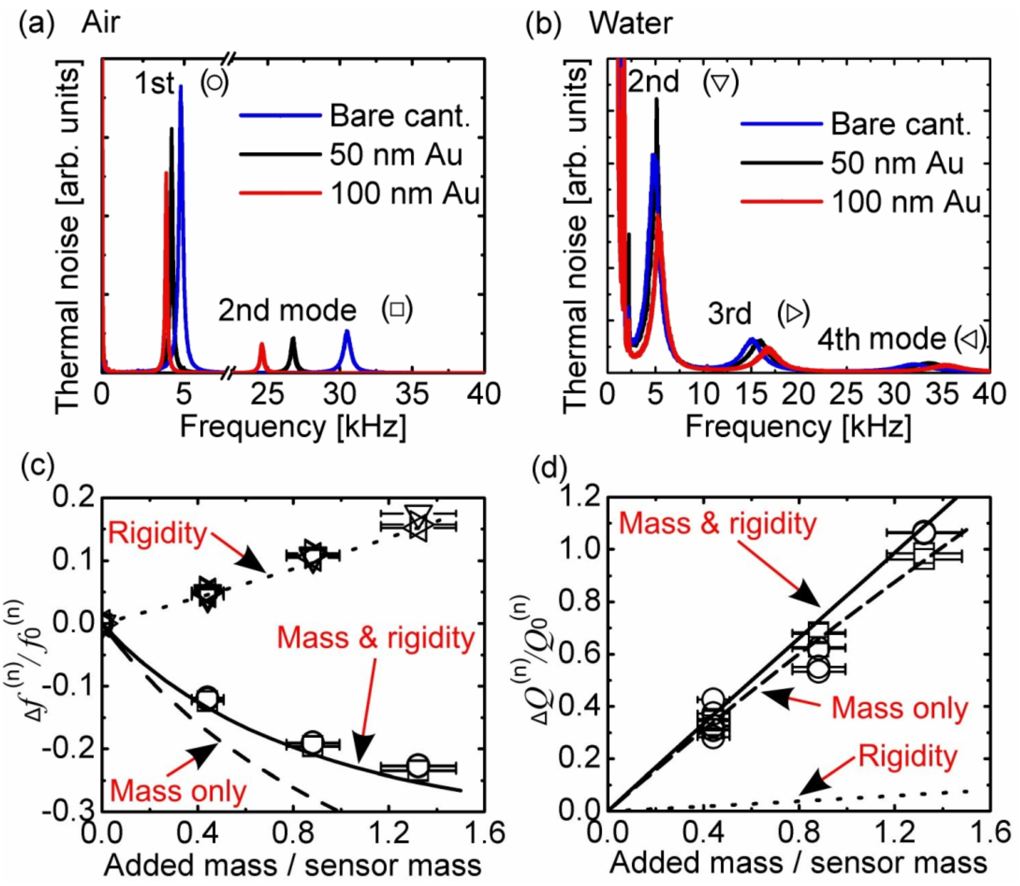

Figure 4.1 *(a) Thermal noise spectra for cantilevers with different gold coatings, in air. (b) As (a), in distilled water. (c)* $\Delta f^{(n)}/f_0^{(n)}$ *as a function of metal film mass normalised to cantilever mass. Circles and squares denote data taken in air for the 1st and 2nd mode, respectively, see (a); triangles denote data taken in water for the 2nd, 3rd, and 4th mode, see (b). (d)* $\Delta Q^{(n)}/Q_0^{(n)}$*. The curves mark theoretical predictions.*

In air, the experimental data clearly deviate from the prediction for added mass only, but match the theoretical curves for added mass and rigidity. In water, however, due to the increased effective mass of the bare cantilever [Ghatkesar08] the cantilevers behave as if the gold films only affect the rigidity of the cantilevers, without increasing their mass at all. The first mode in water has been disregarded in the analysis, since its $Q \approx 1$.

For ultrathin and heterogeneous adsorbates, the material properties are expected to significantly deviate from their bulk values. To increase the sensitivity for such effects, ultrasmall silicon cantilevers are used, typically 25μm × 4 μm × 200 nm [Yang05]. First, their thermal noise spectra are determined around the first mode of oscillation in air using a small-spot interferometer [Hoogenboom05]. The resonance frequencies of different cantilevers before and after adding thin films can then be compared. The exact dimensions of each cantilever were determined by scanning electron microscopy, which also enabled corrections for the mass of the AFM tip on these cantilevers.

4.5.2 Copper Thin Films

Copper films are used as a model system for this second set of experiments, because (i) copper gives rise to a large difference between the frequency shifts due to mass-only and rigidity-only; (ii) it does not require any intermediate layer to adhere on silicon(-oxide); and (iii) for the deliberately chosen slow evaporation rates, copper films show island growth [Benouattas06].

The results of these experiments are shown in Figure 4.2, along with the nanoscale topography of the films as measured by atomic force microscopy (AFM), and compared to the theoretical predictions (mass only and mass and rigidity) for pure copper films. For an average copper thickness of 3 nm (about 3 pg mass), the adsorbed copper appears as isolated islands, resulting in frequency shifts that correspond to a mass-only effect on the cantilever resonance frequencies. For increasing film thickness, the islands coalesce and the frequency shifts show increasing deviations from the mass-only prediction, to finally approach the mass and rigidity prediction for homogeneous copper coverage. The copper will certainly be oxidized to some extent (as stated earlier, the thermal noise was measured under ambient conditions) but oxidation alone cannot fully account for the deviations from the “mass and rigidity” prediction for homogeneous films; to first order in t, $\Delta f^{(n)}/f_0^{(n)} = ½(3E-\rho)t = ½[(E_a\rho_c)/(E_c/\rho_a) - 1]m_a/m_c$ [Tamayo06] and since the product $E_a\rho_c/E_c\rho_a$ hardly changes from copper to copper-oxide [Tan07], the main effect of oxidation will be an increase in slope due to the added oxygen mass, by at most 25% (one oxygen atom for each copper atom). This is not sufficient to account for the experimental data. The observed behaviour can more readily be interpreted by assuming that isolated, dilute islands do not have any effect on the overall rigidity of the cantilever, while they do contribute to its mass. As soon as the islands cover a substantial part of the cantilever and coalesce, the adsorbate starts to behave like a homogeneous over-layer, with elastic properties approaching that of the bulk material.

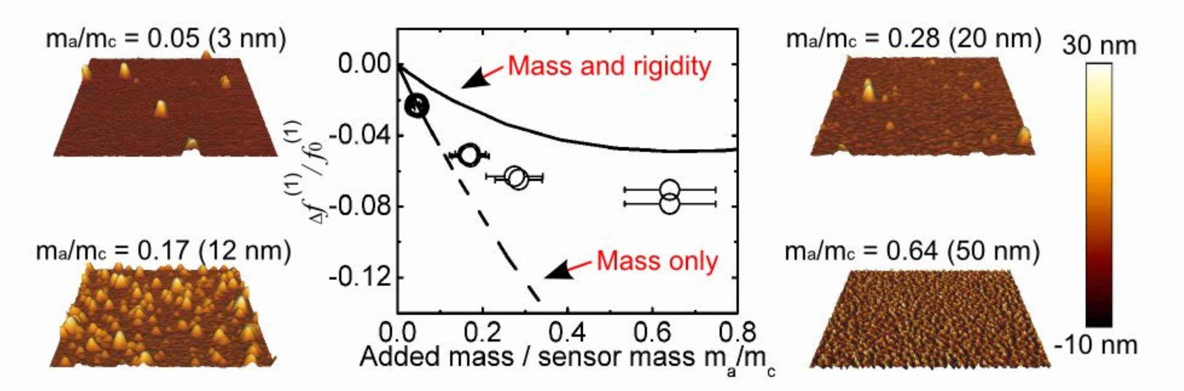

Figure 4.2 *Effect of copper films on the cantilever resonance frequencies, from dilute coverage to homogeneous films. Centre, circles: $\Delta f^{(1)}/f_0^{(1)}$ as a function of added copper mass normalised to cantilever mass (m_a/m_c), compared to theoretical predictions. Left and right: 1 × 1 μm^2 AFM topographic images illustrate the cantilever coverage for average film thicknesses of 3, 12, 20, and 50 nm.*

4.5.3 Rigidity Effects

Based on the results in Figure 4.1 and 4.2, it can be concluded that it is not possible to determine added mass (or added rigidity, or both) from the frequency shifts without *a priori* knowledge on the adsorbate or without additional sources of information. However, the quality factors (Equation

4.2) enable extraction of the relative change in mass (ρt) of the cantilever, once the natural frequency and quality factor before and after adsorption of the sample have been measured. Subsequently, ρt can be inserted in Equation 4.1 to determine D/D_0. The results of this procedure are plotted in Figure 4.3, where $t = t_a/t_c$ was determined from independent quartz crystal microbalance measurements and cantilever thickness, and compared to the theoretical behaviour straight line with slope ρ_a/ρ_c in (a), and D/D_0 from [Tamayo06] and Equation 2.5, Chapter 2 in (b). The larger scatter of the data for the first mode (Figures. 4.3(a)–4.3(c)) is attributed to its low quality factor, partially invalidating the assumption $Q >> 1$ for Equation 3.2 as follows: $Q_0^{(1)} \approx 17$ for these cantilevers, whereas $Q_0^{(2)} \approx 50$. The errors in these cantilever measurements are small compared to the errors in the film thickness measurements with the quartz crystal microbalance during evaporation. Certain assumptions are being made when using quartz crystal to monitor film deposition, including: proper calibration; quartz quality and correct equipment usage. These could be attributed to the larger errors in thickness measurements via PVD. However an error in calibration is the most likely cause as quartz quality was checked prior to usage, and operation of the evaporator was supervised by a trained technician.

Next, knowing ρ_a, ρ_c, and t_c, the Young's modulus of the film material can be extracted from the expression for D/D_0 [Tamayo06] see Figure 4.3(c). For the copper films on the ultrasmall cantilevers, the quality factors are more difficult to interpret because of the additional mass of an AFM tip on these cantilevers. Therefore the Young's modulus E_a is determined by an alternative procedure, which compares the data points to the "mass & rigidity" prediction and adjusts E_a to achieve the best match (Figure. 4.3(d)). The thus determined Young's moduli vary from ~0% for isolated copper islands to ~80% of the bulk copper value for more homogeneous coverages.

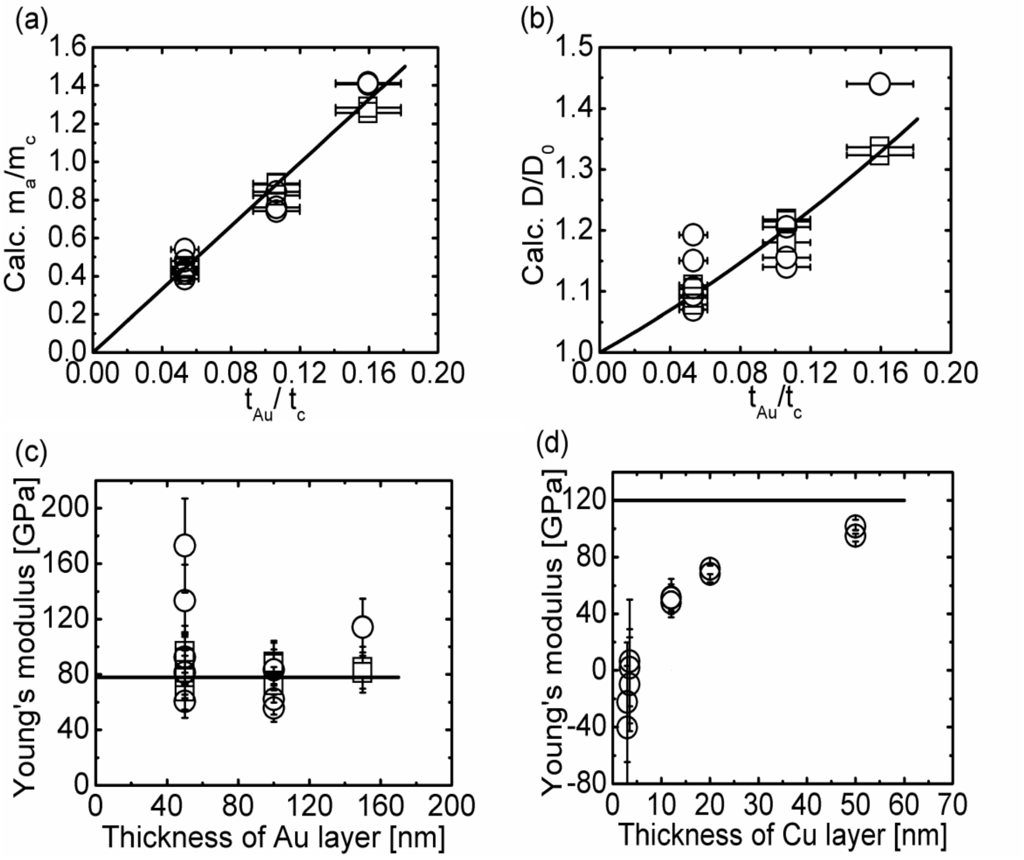

Figure 4.3 *[(a) and (b)] Calculated mass and rigidity from $f^{(n)}$ and $Q^{(n)}$ for different gold thicknesses, compared to expected values. [(c) and (d)] Young's moduli of the gold film on the cantilever arrays and of the copper film on the ultrasmall cantilevers. The horizontal lines represent the literature values for the bulk material. Circles and squares refer to the first and second modes of oscillation, as previously.*

4.6 Summary and Conclusions

The results in Figure 4.3 demonstrate two important findings: (i) The adsorbate mass can be accurately determined by combining resonance frequencies and quality factors of micromechanical resonators, also when the resonator response results from a combination of added mass and rigidity. (ii) Such measurements can be used to measure both adsorbate mass and elastic properties. This is particularly useful to determine how the properties of thin films deviate from bulk behaviour [Figure 4.3(d)]. More generally, such measurements enable simultaneous measurement of the presence of adsorbate and elastic interactions within it. Watari *et.al.*[Watari08] have demonstrated that, at the molecular level, such interactions also underlie the surface stress change induced by binding of antibiotics to bacterial cell wall peptides, causing the static bending of the cantilevers [Ndieyira08, Sushko08, Watari08]. These interactions have general applicability to biosensing and disease diagnostic applications of cantilever technology [McKendry02].

In this chapter, difficulties in interpreting the response of micromechanical resonators to nanoscale adsorbates is discussed, along with how to deconvolve the effects of added mass and added rigidity. Interestingly, the method applied makes use of damping of the cantilever by the surrounding medium, which is usually regarded as a problem, rather than an asset for micromechanical sensing.

In chapter five these ideas are developed, utilising metallic thin-film systems as described here, but now further investigating the hydrodynamic loading effects. The thermal noise spectrums in Figure 3.1 (a) and (b) illustrates the differing resonance effects between increasing layer mass upon operating the cantilever in air and water. Upon resonance in air, increasing adsorbate mass produces a reduction in resonance frequency, analogous to the harmonic oscillator model.

Crucially, this situation is reversed in water, where a higher adsorbate mass produces a higher resonance frequency. From this it can be seen that fluid mass and fluid density have a significant influence on the sensor response. Considerations when operating a cantilever in water include increased effective cantilever mass due to the additional liquid mass being dragged as the beam resonates, and viscous damping suppressing the sensor’s resonant behaviour. This increased complexity in disentangling adsorbate mass and stiffness effects is investigated, developing cantilever resonance measurements in fluid from 20-150 nm metallic films, to nm-thick self-assembled monolayers, and finally antibiotic sensing using vancomycin.

CHAPTER 5

Stiffness and Mass in Cantilever Sensing in Solution

5.1 Chapter Overview

Micro and nanomechanical cantilever sensors are effective, label-free sensors of analytes in liquid. However the sensor response is dependent on counteracting changes in mass and stiffness upon analyte adsorption, complicating its interpretation and reducing sensitivity. This demonstrates a key disadvantaging in dynamic sensing, as for nanometer-scale coverage, mass and stiffness can only be guessed. Experiments to solve this problem and disentangle the sensor response in liquid are presented in this chapter. Measurements begin with metal layer coverage, ranging from 20-150nm. Work is then extended to molecular overlayers, via the adsorption of SAMs and antibiotic sensing using vancomycin. Such systems complicate sensing and analysis, as instead of the nm thick layers seen in the metal coatings, these layers are significantly thinner, ~1nm thick. This in turn will test the cantilever's sensitivity as adsorbate masses are significantly reduced. In addition, the molecular packing of such overlayers is significantly more complex than metal film structure, implying the presence of a wider range of structural phenomena and rearrangements to be probed.

As all experiments are conducted in liquid, additional fluid loading effects also need to be accounted for. This is achieved via the use of the hydrodynamic function [Sader98]. Additional complications arise from operating the cantilever in liquid, as the quality factor is significantly reduced.

5.2. Introduction

Micromechanical resonators are well established and highly sensitive adsorbate mass and stiffness sensors [Ilic04, Tamayo06, Lachut07, Ramos07]. When operating the cantilever in static-mode, the beam is sensitive to changes in surface stress upon analyte adsorption, causing the cantilever to bend [Fritz00, McKendry02, Arntz03, Mukhopadhyay05, Mertens08]. However surface stress is strongly dependent on the exact surface structure and chemistry of the adsorbate-cantilever interface, complicating interpretation of the sensor response.

When operated in dynamic mode, the cantilever can be thought of as a mechanical oscillator, with the resonance characteristics being dependent on the adsorbate [Tamayo06, Grüter10] and the viscoelastic properties of the medium [Paxman12]. The cantilever resonance can be characterised via its resonance frequency and its quality factor. These two parameters provide complementary data regarding interactions between the sensor, environment and adsorbate. Dynamic, as opposed to static, sensing also demonstrates a lower sensitivity towards drift and can be operated at a higher resonance frequency, making such devices highly sensitive in detecting adsorbate effects.

Previous theoretical work has predicted considerable adsorbate effects of both added mass and changes in rigidity on measured frequency shifts [Tamayo06, Grüter10]: Whilst adsorbate stiffness increases cantilever flexural rigidity, giving a positive contribution to the resonant frequency shift, added mass effects produce an opposing, negative effect.

This chapter examines which affect, that of mass or that of stiffness, has a dominating influence on the dynamic sensor response when operated in solution. A method to deconvolve these two effects is presented and first applied to nm-thick metallic films as in chapter 4. Next, self-assembled monolayers (SAMs) are used as a sample to demonstrate the application to molecular adsorbates, and finally vancomycin-mucopeptide interactions to demonstrate the potential for biomedical sensing.

5.3 Self-Assembled Monolayers

SAMs provide a convenient, adaptable, and simple system in which to tailor the interfacial properties of metals, metal oxides, and semiconductors. They are organic systems, created by the adsorption of a surfactant molecule onto the surface of a solid or liquids. Adsorbate organisation occurs spontaneously into crystalline (or semicrystalline) structures. The molecules forming the monolayer have a chemical functionality, or ‘headgroup’, with a specific binding affinity to the substrate, with a number of headgroups that bind to specific metals, metal oxides, and semiconductors. One of the most extensively studied classes of SAMs is derived from the adsorption of alkanethiols on gold [Nuzzo83, Porter87, Poirie97]. SAMs of simple n-alkanethiols on Au(111), with an ordered and densely packed organic membrane, well-controlled surface chemistry and mechanical properties, provide a model for biomolecular surfaces.

For the sensing systems used in this work, the cantilever surface acts as a template for the formation of a well-defined functional layer. A schematic of SAM alkanethiols on gold is show in Figure 5.1.

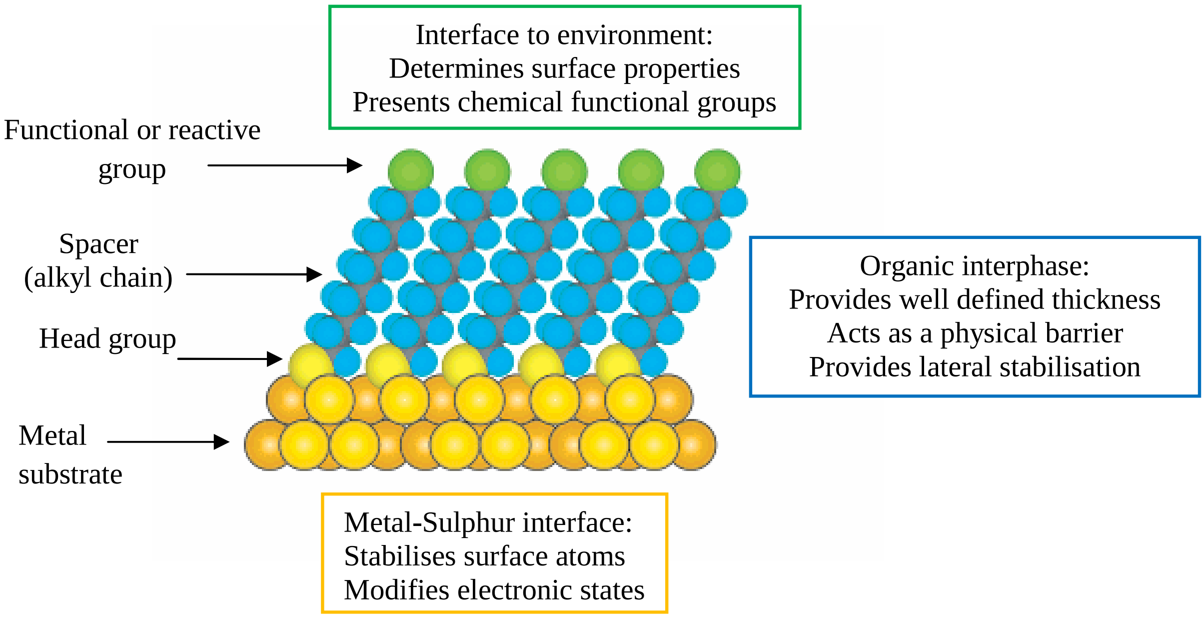

***Figure 5.1** Schematic of an ideal, single-crystalline SAM of alkanethiolates supported on a gold surface. The components and characteristics of the SAM are highlighted [Love05]. Permission to reproduce this figure has been granted by Professor Ralph Nuzzo, University of Illinois.*

The tilt angle of the described monolayer will vary depending on the spacing of the sulphur groups. At a low alkane-thiol surface coverage, when there is large sulphur-sulphur spacing, the chains can have a tilt angle as such so the molecules may lie flat on the gold surface (low tilt angle). As the chain length increases, it is thought that the tilt angle increases, minimising the free volume between the alkyl chains and maximising Van der Waals interactions. The exact bonding mechanism of the Au-S interaction is still subject of scientific debate and the involvement of a structural gold-atom has been proposed [Maksymovych10], nonetheless the bonding habit of high-coverage thiol phases on Au(111) is generally accepted to be based on a $(\sqrt{3} \times \sqrt{3})R30°$ overlayer.

The generation of surface stress during the formation of SAMs and its chain length dependence have been previously investigated [Berger97, Godin 04]. These studies agreed in that the formation of SAMs induced a compressive surface stress change. However, the chain length dependence was subject to controversy: while Berger reported a monotonic chain length dependence of the surface stress generated upon SAM formation, Godin found that the surface stress was generated independent of the chain length. Furthermore, the reported surface stress values varied over two orders of magnitude, that is, from -10^{-1} to -10^{1} N/m. Godin demonstrated that differences in the gold morphology alone can account for the discrepancies. Importantly, both studies used the cantilever itself as its own reference state, thus the sign and magnitude of the absolute stress remained uncertain.

One shortcoming of the structural model described in Figure 5.1 is the assumption of a flat, homogeneous gold layer in which the alkane-thiols anchor to, where in fact the surface is most likely to be more undulating. High resolution scanning tunnelling microscopy studies have investigated the molecular structure of SAMs, and reported that the majority of defects were generated at grain and domain boundaries [Poirier99]. Such studies suggested that SAMs at saturation coverage exhibited an equilibrium amount of domains and defects, rather than a single phase of close packed alkanethiols on Au(111). Furthermore, when assuming a homogeneous surface coverage, it is likely that one may underestimate the number of alkanethiol chains on the surface, as in fact the gold surface area is greater than it is being attributed. This may potentially impact on mass calculations.

Monomolecular films of organic amphiphiles are subject to a number of forces that influence their ordering dynamics and equilibrium structures. These forces include interactions of the amphiphile’s “head group” with the corrugated surface adlattice, van der Waals interactions between neighbouring alkyl chains, and interactions between the amphiphile “tail groups’). The nature of these interactions in liquid phase SAM adsorption has been previously investigated [Poirier94], where methyl-terminating SAMs of chain length C4, C6, C8 and C10 were adsorbed onto single crystalline Au(111) surfaces. These were then characterized via ultrahigh vacuum scanning tunnelling microscopy. Short-chain homologues (C4 and C6) exhibited a two-dimensional (2-D) liquid phase at room temperature, with facile mass transport of surface gold atoms also being observed in the presence of the liquid phase. The short-chain homologues exhibited slow desorption of surface thiolate which led to the nucleation and growth of ordered domains having a unit cell of $p \times \sqrt{3}$ ($8 \leq p \leq 10$). Furthermore, no 2-D liquid phase was observed for longer chain homologues (C8 and C10). The behaviour of C4 SAMs was found to sharply contrasts the behaviour of C8 and Cl0 SAMs, which formed a dense-packed, stable monolayers with a $c(4 \times 2)$ superlattice of a ($\sqrt{3} \times \sqrt{3}$) R30 lattice. From these results, a similar contrast between the C3 and C11-C16 chains investigated in this thesis can be expected.

5.3.1 Growth of SAMs

SAMs have been extensively studied using a variety of experimental procedures, such as spectroscopic techniques (e.g. x-ray photoelectron spectroscopy, ellipsometry) and scanning probe microscopy (scanning tunnelling microscopy and atomic force microscopy) [Schreiber00, Yang03]. Theoretical investigation into the mechanical properties of gold/alkanethiol films has been also been investigated [Sushko08]. At a very low surface coverage, the large distance between two alkanethiol molecules means there will be no interaction between the alkanethiols. This is referred to as the ‘lattice gas’ phase. The interaction between the alkanethiol molecules and the gold surface is steered by the strong Au-S bond (-50 kcal/mol [Nuzzo87]), and weak van der Waals physisorption of the alkyl chain onto the gold surface. Under these conditions the molecular axis of the physisorbed molecules is randomly distributed. Upon increasing the surface coverage, the distance between the alkanethiol molecules decreases, hence interactions between the alkanethiol molecules will increase.

Figure 5.2 illustrates the sequential phases of SAM formation. It is understood that thiols first form a dilute layer where the adsorbed molecules are lying flat on the substrate (lying-down phase, Figure 5.2(a)) [Love05].When the number of adsorbed thiols increases, islands with densely packed molecules are formed which grow until a complete monolayer is formed covering the whole substrate (standing-up phase, Figure 5.2(c)).

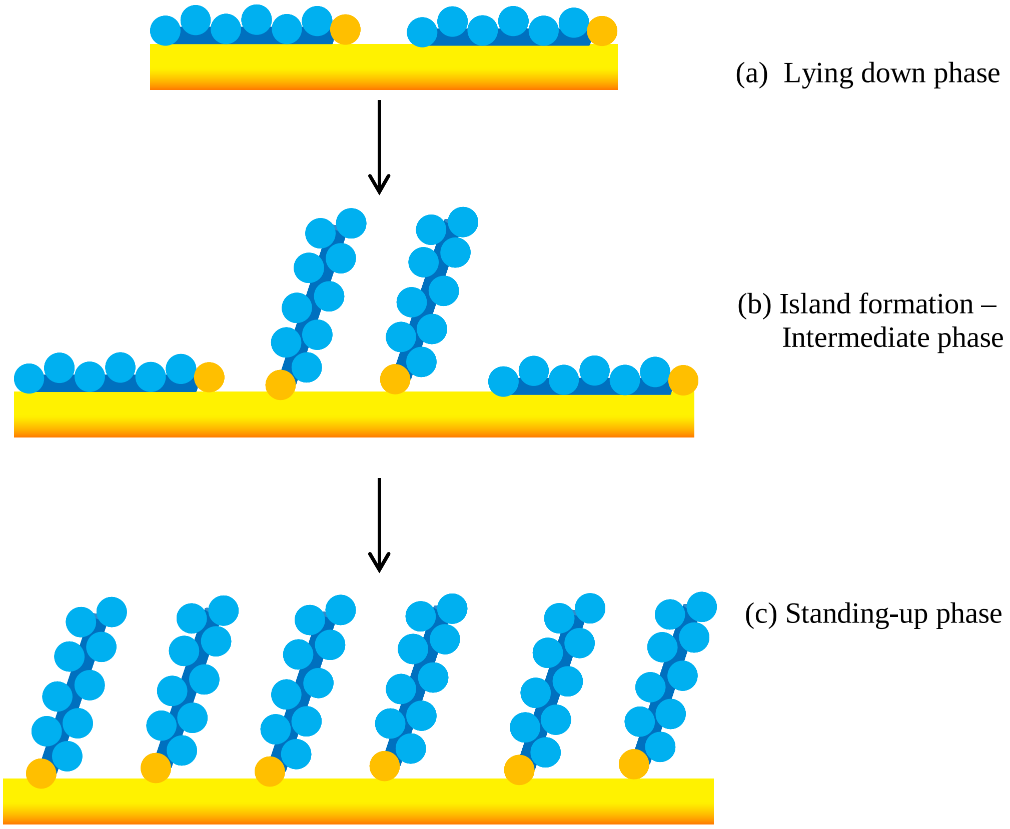

Figure 5.2 *Schematic illustrating the phases of SAM formation, moving from (a) lying down to (c) standing up phase.*

To what extent do these structural re-arrangements influence the resonant behaviour of the cantilever, and how sensitive is the sensor to these? We next apply the dynamic model discussed in previous chapters to help gain a more quantitative rationale of the sensor's behaviour

5.4 Methods

We consider a singly clamped rectangular cantilevers with a length *l* that is long compared to its width *w*, and wide compared to its bare thickness t_c. In a viscous medium of mass density ρ, the adsorption of a homogeneous film on the cantilever will change the natural frequency $f_{res}^{(n)}$ of its *n*-th mode of flexural oscillation according to

$$\left(\frac{f^{(n)}}{f_0^{(n)}}\right)^2 = \frac{1+\frac{\pi\rho w^2}{4\mu_0}\Gamma_r\left(f_0^{(n)}\right)}{\frac{\pi\rho w^2}{4\mu}\Gamma_r\left(f^{(n)}\right)} \times \frac{D/D_0}{\mu/\mu_0}, \qquad 5.1$$

where $f_0^{(n)}$ is the natural frequency of the unloaded (bare) cantilever [Sader98, Tamayo06, Grüter10] *D* is the flexural rigidity of the cantilever and μ its mass per unit length; *D* and μ can be normalised to their respective values $\mu_0 = \rho_c t_c w$ and D_0 for the unloaded cantilever, where ρ_c is the mass density of the cantilever material (the corresponding masses follow from $m = \mu l$). D/D_0 is a function of the respective thickness and Young's modulus of the adsorbate and of the cantilever [Tamayo06]. Γ is the hydrodynamic function for a rectangular beam, which in its simplest form depends on the frequency and the width of the cantilever, and on the density and the viscosity of the medium [Sader98, Eysden09]. Subscripts *r*,*i* are used to denote the real and imaginary part of Γ respectively. Given a simple function for Γ [Sader98] this implicit equation for $f_{res}^{(n)}$ can be solved numerically.

The real part of the hydrodynamic function, now included in Equation 5.1, accounts for the added mass effect of the surrounding fluid, an effect neglected for the analysis of measurement in air (Chapter 4, Equation 4.1). A further description of this can be found in section 2.5. Adsorbate mass and rigidity effects are included in Equation 5.1, via Equations 2.10 and 2.5 respectively, permitting simultaneous calculated of such effects in fluid. This was executed using a numerical nonlinear least squares regression algorithm in Mathematica (Wolfram Research Inc. IL, USA). Details of this are provided in Appendix F. More complex formulations for Γ are available [Eysden09], extending Sader [Sader98] to 3-D, accounting for increasing mode numbers.

Once $f_{res}^{(n)}$ is known, calculation of the corresponding quality factor is straightforward (since for pressures above 10^{-2} mbar, it is uniquely determined by the interaction of the cantilever with the surrounding medium [Yang02]). Both Equations 5.2 and 4.2 include the imaginary part of the hydrodynamic function, however the real part is only accounted for in Equation 5.2. This accounts for the surrounding fluid, as the imaginary part represents the fluid damping, while the real part represents the added mass effect of the surrounding fluid.

$$\frac{Q^{(n)}}{Q_0^{(n)}} = \frac{\dfrac{4\mu}{\pi\rho w^2} + \Gamma_r\left(f^{(n)}\right)}{\dfrac{4\mu_0}{\pi\rho w^2} + \Gamma_r\left(f_0^{(n)}\right)} \times \frac{\Gamma_i\left(f_0^{(n)}\right)}{\Gamma i\left(f^{(n)}\right)}\ , \qquad 5.2$$

where $Q^{(n)}$ and $Q_0^{(n)}$ are the quality factors of n-th mode of the loaded and unloaded cantilever, respectively [Sader98]. The left hand part of Equation 5.2 accounts for the beam's mass per unit length (μ), fluid density and cantilever width, not included in Equation 4.1, again accounting for fluid effects. Solving Equation. 5.1 will extract the resonance frequency, which can then be used in Equation. 5.2, providing the theoretical relations for the resonant properties of the cantilever act as a function of adsorbed material. Additionally, Equations. 5.1 and 5.2 can be solved to calculate the cantilever response to hypothetical adsorbates that only change the mass (i.e., $m \neq m_0$ and $D = D_0$) or stiffness (i.e., $D \neq D_0$ and $m = m_0$) of the cantilever.

Within the same framework [Sader98], it is possible to derive an inverse relation that enables us to determine the adsorbed mass $\Delta m = m - m_0$, based on measured changes in the natural frequency and in the quality factor. Equation 5.3 extends on Equations 2.7, 2.8 and 4.1 and 4.2 which relate changes in resonance frequency and quality factor as a function of adsorbate mass respectively. Equations 2.7 and 2.8 account for oscillating the cantilever in a viscous medium, including the real and imaginary parts of the hydrodynamic function.

$$\frac{\Delta m}{m_0} = \alpha^{(n)} \frac{\Delta Q^{(n)}}{Q_0^{(n)}} + \alpha^{(n)} \frac{Q^{(n)}}{Q_0^{(n)}} \frac{\Delta\Gamma_i(f^{(n)}, f_0^{(n)})}{\Gamma_i(f_0^{(n)})} - (\alpha^{(n)} - 1) \frac{\Delta\Gamma_r(f^{(n)}, f_0^{(n)})}{\Gamma_r(f_0^{(n)})}, \qquad 5.3$$

where $\Delta Q^{(n)} = Q^{(n)} - Q_0^{(n)}$, $\Delta\Gamma_{r,I}(f^{(n)}, f_0^{n}) = \Gamma_{r,i}(f^{(n)}) - \Gamma_{r,i}(f_0^{(n)})$, $\alpha = (f_{0,vac}^{(n)}/f_0^{(n)})^2 = \frac{\pi\rho w^2}{4\mu_0} +$

$\Gamma_r\ (f_0^{n})$ is the ratio between the effective mass (including displaced liquid) and the real mass of the cantilever (which was assumed 1 for the measurements in air in chapter 4), and $f_{0,vac}^{(n)}$ is the natural frequency of the bare cantilever in vacuum. $\alpha^{(n)}$ defines the square of the ratio between the unloaded cantilever resonance frequency in vacuum, and the resonance frequency of the unloaded cantilever in the measurement medium.

Since $f_{0,vac}^{(n)} \approx f_{0,air}^{(n)}$ this ratio can be assumed unity in air and easily be measured for denser and/or more viscous liquids. Similarly, the change in flexural rigidity $\Delta D = D - D_0$ follows from

$$\frac{\Delta D}{D_0} = \left(\frac{f^{(n)}}{f_0^{(n)}}\right)^2 \frac{Q^{(n)}}{Q_0^{(n)}} \frac{\Gamma_i\left(f^{(n)}\right)}{\Gamma_i\left(f_0^{(n)}\right)} - 1, \tag{5.4}$$

Fit results for experimental rigidity data were calculated from Equation 2.5, Chapter 2 [Tamayo06].

nm-thick metal films were evaporated onto one side of the cantilever via electron beam evaporation, operated at a base pressure of approximately 10^{-7} mbar (BOC Edwards A500, U.K). Tipless single-crystal silicon cantilevers with dimensions 500 × 100 × 0.9 μm^3 were used in all measurements (IBM) [Ghatkesar07]. For gold coatings, a 2nm titanium adhesion layer was also required. The evaporation rates for copper, gold and titanium deposition were 0.01nm/sec, 0.09nm/sec and 0.04nm/sec respectively. For thiol-functionalisation, the evaporated cantilevers were sealed under argon and functionalised with the required SAMs within 24-hours following evaporation. The cantilevers were incubated for 20 minutes in a parallel array of eight glass microcapillaries. These are filled in random order of approximately 2 mM ethanolic solution of the thiols, then rinsed in pure ethanol and deionised water. Dr. Moyu Watari is acknowledged for functionalising the cantilevers with the SAMs.

For antibiotic experiments, DAla is used as a mucopeptide analogue to form the sensing layer. This is present in the cell walls of Vancomycin-sensitive Enterococci (VSE), taking the chemical form $HS(CH_2)_{11}(OCH_2CH_2)_3O(CH_2)(CO)NH(CH_2)_5(CO)$-L-Lys-(□-Ac)-D-Ala-D-Ala. □ refers to the linkage of the acetyl molecules. Reference cantilevers are functionalized with a thiol terminating triethylene glycol, $HS(CH_2)_{11}(OCH_2CH_2)_3OH$, abbreviated to PEG.

Surfaces coated with polyethylene glycol are known to minimise biomolecule adsorption [Shu07, Knowles08], so should show only slight changes in cantilever deflection upon injection of vancomycin solution.

For measuring resonance frequency and quality factor, the cantilever is mounted in a commercial atomic force microscope (Nanowizard I, JPK Instruments, Berlin, Germany) and submerged in 100–200 µL of deionised (milliQ) water. The dynamic properties of the cantilever were determined from their thermal noise spectrum, with no other sources of external actuation. Cantilever oscillations were monitored using standard optical beam deflection, with a laser being focused on the free end of the cantilever and reflected back onto the Position Sensitive Detector (PSD), as described in Section 3.3.1. Cantilever motion will consequently change the laser position on the photodiode and therefore the light intensity on each cell. Prior to measurement, the laser spot is aligned in the centre of the PSD, so each segment has equal levels of illumination. Between 3-13 repeat measurements were performed for all coatings.

The resonance behaviour of the cantilever is determined from the digitally calculated and averaged Fourier spectrum of the thermal noise of the cantilever. The thermal noise spectrum is then fitted with a simple harmonic oscillator model, via which $f_{res}^{(n)}$ and $Q^{(n)}$ are determined. Because of the broadness of the peaks, different modes of oscillation are not strictly separated any more in the frequency domain. To enhance the accuracy of the fitting procedure, we subsequently fit the different modes (up to $n = 3$) in the thermal noise spectrum, starting with the first (fundamental) mode, and for each higher mode fit the thermal noise spectrum after subtracting the fit(s) of the lower mode(s) from the experimental data. This prevents the tails of the lower modes from polluting the fits to the higher modes of oscillation. Further details of the fitting procedure are given in section 3.4. The fitting procedure is implemented in Mathematica, and outlined in Appendix F. All measurements were carried out at 20.5 °C.

5.5 Results

5.5.1 Thermal Noise Spectrum

Figure 5.3 shows the thermal noise spectrum for the second oscillatory mode of a cantilever coated with different length CH_3-terminating SAMs. The nomenclature C3, C8, C11 and C16 is used to denote the varying alkane-thiol carbon chain length (n), with C3 denoting a 3-carbon chain, C8 8-carbons and so forth. C3 chains are seen to produce the highest resonance frequency, in comparison to the other thiol-chain lengths. A smaller frequency is seen in the C16, C11 and C8 chains. Importantly, the observed frequency differences are about 10~20%, while the mass changes are expected to be less than 0.1% of the cantilever mass. This indicates that other factors, such as rigidity, are crucial for determining the resonant response of the cantilever to such molecular overlayers.

The mechanical properties for gold/SAM films can be interpreted as follows: The hydrocarbon molecules form a dense monolayer on the gold surface, with its structure is determined by the interplay of the interactions between the molecules of the gold substrate and intermolecular forces. As the gold substrate expands, the molecules anchoring the sulphurs are driven further apart. Consequently this shifts the balance of surface/intermolecular interactions. The system has to find a new energy minimum, which leads to the change in the tilt angle of the molecules. These structural changes are larger for short molecules with weak intermolecular Van der Waals forces in the SAM.

As chain length changes, so does the alkane-thiol chain positioning, thus affecting the monolayer’s mechanical properties. In the case of C3 chains, a monolayer as presented in Figure 5.2 (a) may not always form, and a situation where chains are constantly attaching and desorbing from the cantilever surface may occur. In such cases, the substrate stiffness may affect the monolayer’s mechanical properties, impacting on the Young’s modulus evaluations. This may be one of the reasons why such a higher Young’s modulus is observed in the C3 chains. This situation is less likely to occur in C8, C11 and C16 layers as packing is denser, therefore the cantilever substrate is more covered.

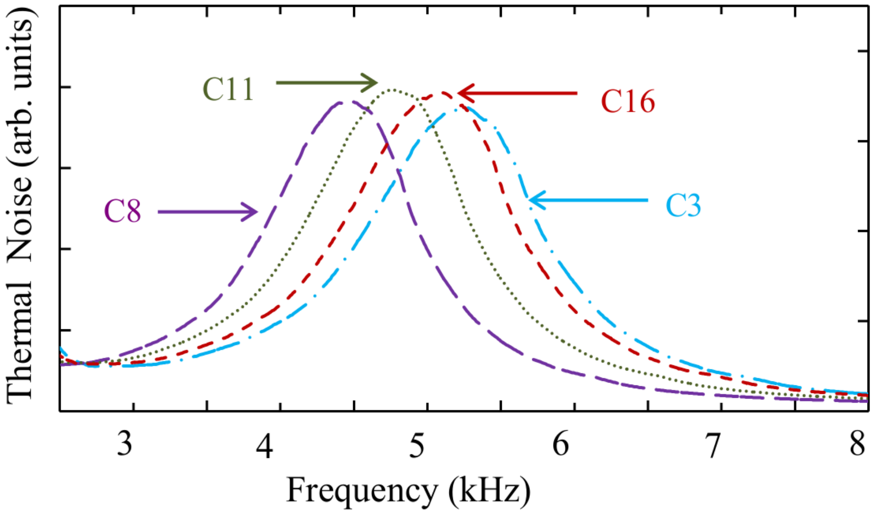

Figure 5.3 *Thermal noise spectrum for a cantilever coated with methyl terminating alkanethiol self-assembled monolayers in water, at oscillatory mode 2. Carbon chain lengths of n = 3,8,11 and 16 used, denoted by C3, C8 etc. Resonance frequencies vary by ≥10% for subnanometer changes in adsorbate thickness Data is taken from the same cantilever array, with frequency variations being ~0.015kHz. The measurement peak obtained from the thermal noise spectrum is more asymmetric than the shape of the peak shown, as the x-axis range applied here has been*

selected in order to highlight the frequency shift between chains C3-C16. Such detail would be lost under a wider x-axis range. A wider frequency range (particularly below 3kHz) would greater demonstrate the asymmetric nature of the resonance peak, as the 'tails' of the mode 1 peak would be visible. The peaks here are an averaged measurement, producing a smoother curve compared to those obtained straight from the measurements obtained via the Veeco Scentris.

5.5.2 Metal Layers

Figures 5.4(a) and 5.4(b) show the relative resonance frequency ($(\Delta f / f_0^{(n)}) = (f^{(n)} - f_0^{(n)}) / f_0^{(n)}$) and quality factor shifts ($(\Delta Q / Q_0^{(n)}) = (Q^{(n)} - Q_0^{(n)}) / Q_0^{(n)}$) for cantilevers coated with gold, copper or titanium nm-thick films. The relative change in mass, areal layer density and rigidity effects are given in Figures 5.4(c) and 5.4(d). Results from the second and third oscillatory modes are denoted by open and closed symbols respectively. As expected, an increase in layer thickness produces an increase in frequency and quality factor shifts. The theoretical predictions for the cantilever response were calculated via Equation. 5.1 for the frequency response and Equation. 5.2 for changes in $Q^{(n))}$, and are illustrated by dashed lines. Using the changes in natural resonance frequency and quality factor, along with Equation. 5.3, changes in adsorbed mass can be quantified, as shown in 5.4(c). Here, the solid line denoted the linear fits for each metal, taking the form $\Delta m/m_0 = (\rho_a \times t_a)/ (\rho_c \times t_c)$, restricted to go through the origin. Subscripts *a* and *c* indicate adsorbate and cantilever respectively, with mass density values for silicon, copper, gold and titanium taken from the literature [Hayes10]. Changes in flexural rigidity (5.4(d)) are fitted based on Equation 2.5 [Tamayo06]. A 10% error in metal layer thickness is included, with both horizontal and vertical errors taken into account when fitting. Fit results are then used to determine the experimental mass density and Young's modulus, the results of which are shown in Table 5.1.

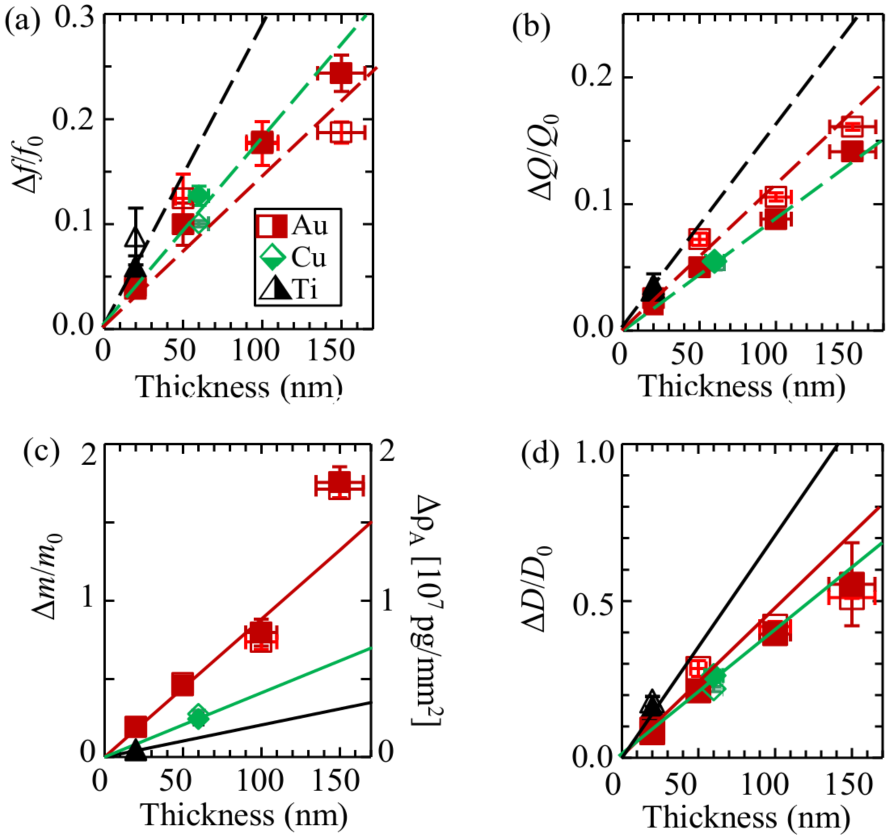

Figure 5.4 *(a) $\Delta f/f_0$ as a function of layer thickness, as determined via QCM. Red, green and black symbols denote gold, copper and titanium coatings respectively. Open and filled symbols represent the second and third oscillatory modes respectively. Dashed lines illustrate the theoretical frequency shift, as calculated via Equation 5.1. (b) $\Delta Q/Q_0$ as a function of layer thickness, the dashed-line theoretical response calculated via Equation 5.2. (c) metal layer mass*

as a function of layer thickness. The left-hand axis represents the relative change in mass, whilst the right-hand axis is the metal's areal mass density. (d) $\Delta D/D_0$ *as a function of layer thickness. Solid line denotes the fit of rigidity change, as calculated in Equation 2.5 [Tamayo06]. Fit results are determined via a root finder procedure, performed in Mathematica, with parameters accounting for both horizontal and vertical error bars.*

Material	$\rho_{lit.}$ **[10^3kg/m^3]**	$\rho_{exp.}$ **[10^3kg/m^3]**	**$E_{lit.}$ [GPa]**	**$E_{lit.}$ [GPa]**
Au	19	19.3±1.0	78	89 ±13
Ti	4	4.5 ±0.3	116	121 ±6
Cu	9	9.3 ±0.4	120	130 ±11
Si	2.3	-	150	-

Table 5.1 *Comparison of theoretical and experimentally determined mass density (ρ) and Young's modulus (E) for gold, copper and titanium films. The literature value for the mass density and Young's modulus of Silicon is also provided for comparative purposes. Literature [Haynes10] and experimental values denoted by subscript lit. and exp. respectively. Error ranges are also included, calculated via standard deviation of repeat experiments.*

A comparison of experimental and literature values for metal mass density and Young's modulus is shown in Table 5.1. The fit results demonstrate the described procedure can be successfully applied to extract the experimental adsorbate mass and Young's modulus of nm-thick metallic films in liquid, with results lying within experimental error for expected, literature values. The slightly larger deviation for the titanium mass density may be due to oxidation of the material or a systematic error in the film thickness measurement.

5.5.3 Self-assembled monolayers

To study (bio)molecular sensing applications, the dynamic model is next applied to self-assembled monolayers. In contrast to inherently complex biomolecules, which have multiple functional and zwitterionic groups, alkanethiols form well-defined SAMs on gold surfaces, where the surface properties are controlled by the chain length and terminal group. In particular, the acid-base properties of carboxylic acid terminating SAMs, which can be controlled via the pH of the aqueous environment, offer an ideal system for fundamental studies with broad applicability to colloidal science and membrane biophysics.

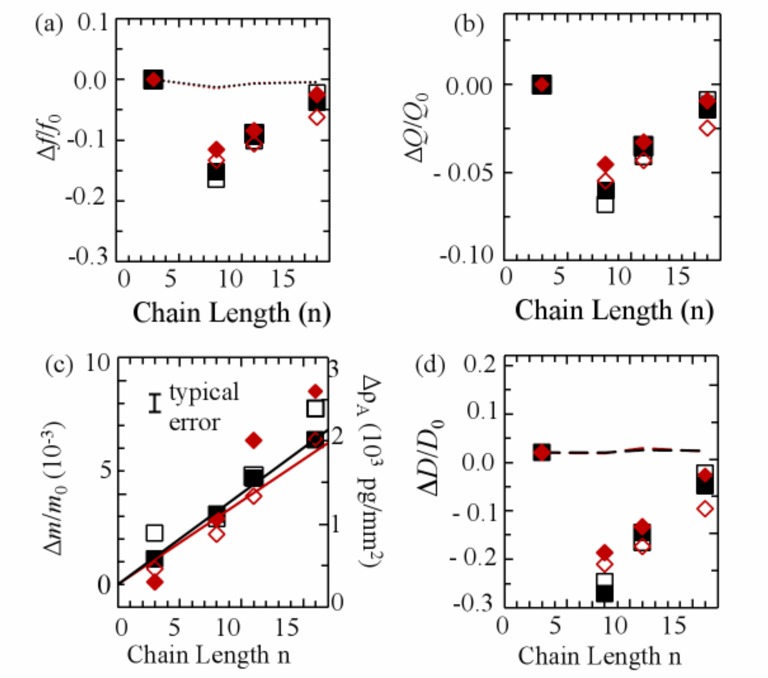

Figure 5.5 *Alkane-thiol chain length of n=3 used as reference (a) $\Delta f/f_0$ as a function of thiol chain length. Black and red symbols denote methyl and acid terminating chains respectively. Open and filled symbols represent the 2nd and 3rd oscillatory modes respectively. Dashed line denotes the theoretical frequency shift, as determined via Equation 5.6 [Lachut07]. (b) $\Delta Q/Q_0$ as a function of chain length. (c) $\Delta m/m_0$ as a function of chain length, with areal*

density illustrated on the right-hand x-axis. Solid lines represent the linear fit. (d) $\Delta D/D_0$ *as a function of chain length. Dashed lines denote theoretical prediction, calculated via Equation 2.5, with thiol Young's modulus based on data in Sushko et.al.[Sushko08] and SAM layer thickness determined via ellipsometry. Individual* D_n *are calculated for each thiol chain length, and from this* $\Delta D/D_0$ *(i.e.* $(D_n\text{-}D_3/)D_3$*) can be calculated. Error bars have been removed as they are too small to displayed*

Figure 5.5(a) and 5.5(b) show the relative frequency and quality factor shift for both methyl and acid terminating chains, upon increasing chain length. Here, $f^{(n)}$ and $Q^{(n)}$ from $n = 3$ are applied as the reference, i.e. $f_0^{(n)}$ and $Q_0^{(n)}$. The choice of appropriate reference was less straight forward, as each thiol chain length had differing influences on the cantilever's rigidity. To examine this, the chain length $n = 16$ was also examined and cross-checked against $n = 3$. The dotted line in Figure 5.4(a) denotes the frequency shift due to stress effects alone, based on cantilever deflection data and calculated via Equation 2.2 [Lachut07].

Stress effects appear to have minimal influence on frequency shifts so can be disregarded in terms of effect on cantilever response. Figure 5.5(b) illustrates the changes in quality factor upon increasing chain length, mimicking previous adsorbate stiffness trends. Figure 5.5(c) shows the change in mass upon increasing chain length, with areal density shown on the secondary *x*-axis, with the linear fit $y = Ax + B$, where A is the intercept and B is the slope. By adding a fit, we are able to examine the where results are deviating from the measured points, and to what extent. From Figure 5.5(c), the greatest degree of deviation comes from the longer chain lengths, in particular the acid-terminating chains. The least deviation between data points and the fit is seen for the C3 and C8 chains. The slope's gradient is similar for both the methyl and acid terminating chains, indicating both to undergo a similar extent of relative mass addition. Changes in flexural rigidity are shown in Figure 5.5(d), with fits calculated according to Equation 2.5 [Tamayo06]. For example, when $n = 3$ is applied as the reference, a theoretical rigidity at this chain length is first determined. From this the other rigidity predictions can be calculated (Equation 2.5). Alkane-thiol layer thicknesses have been previously investigated via ellipsometry [Watari08]. These were determined to be 0.6 nm, 1.2 nm, 1.6 nm and 2.0 nm for C3, C8, C11 and C16 chain lengths respectively, for both acid and methyl terminating groups [Sushko08]. A cantilever's Young's modulus of 150 GPa is applied [Hayes10], with E_a for the alkane-thiols having been previously determined [Sushko08].

Adsorbate Young's modulus predictions are based on previous theoretical calculations [Grüter10] and adsorbate thickness determined via ellipsometry measurement on similarly prepared surfaces. Both vertical and horizontal errors are included in fitting.

In both methyl and acid terminating chains, the 8-carbon chains have previously been calculated as having the lowest biaxial Young's modulus, with respect to C3, C11 and C16 chains [Sushko08]. The difference between the Young's modulus and biaxial Young's modulus is that biaxial elastic modulus is equal to Young's modulus divided by 1-v (v is the Poisson's ratio, which is ≈ 0.5). This means that for SAMs on gold, the Young's modulus will be about two times smaller than corresponding biaxial elastic modulus.

In these atomistic calculations, the biaxial elastic modulus was calculated to increase between C8-C16, ranging from approximately 300 GPa for methyl and acid terminating C16 chains, to 440 GPa (acid terminating) and 636 GPa (methyl terminating) in C3 chains. This trend in biaxial elastic modulus (i.e. C16→C11→C8→C3, lowest → highest GPa) is also reflected our thermal noise results for identical chains (Figure 5.3).

From Figure 5.3, C3 appears as an outlier, relative to the C8, C11 and C16 results. Reasons for such a variation in C3 results could be due to the short-chain alkane-thiols exhibiting a slow desorption of surface thiolate. Previous results [Tamayo06] have found the specific positioning of adsorbates to determine whether a mass or stiffness effect is exhibited, with adsorbates closer to the clamped end displaying greater stiffness effects. As adsorption/desorption is a dynamic process, one cannot assume the cantilever has a homogeneous coverage (and a potential ‘lying-down phase as described in Figure 5.2) at all times of deflection measurement. Once chain length increases, and consequently Van der Waals forces increase, this desorption becomes less, therefore a more homogeneous alkanethiol coverage is obtained.

These results from sub-nanometer layers demonstrate the importance adsorbate stiffness effects have on the cantilever sensor response in solution. Crucially, the results also demonstrate that increasing the SAM layer thickness by only a few methyl groups gives detectable change in cantilever resonance.

Experiments in Figure 5.5 were repeated, but with $f_0^{(n)}$ and $Q_0^{(n)}$ determined from chain length n=16. This chain length is taken as the individual reference for the acid and thiol terminating chains, with results shown in Figure 5.6.

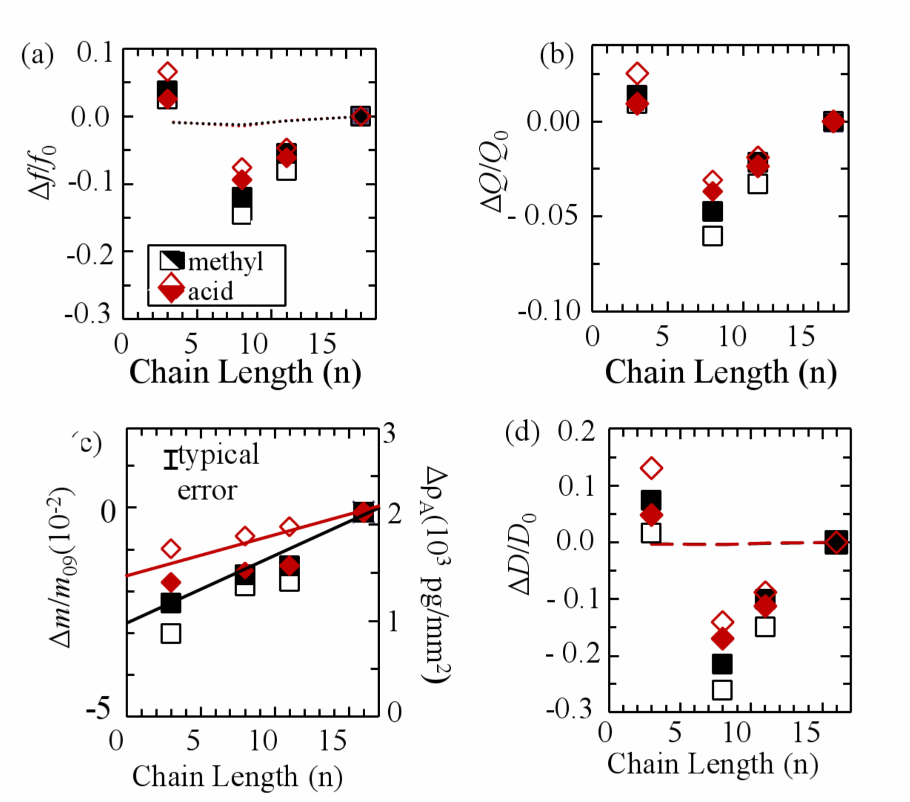

Figure. 5.6 *Alkane-thiol chain length of n=16 used as reference. (a) $\Delta f/f_0$ as a function of thiol chain length. Black and red symbols denote methyl and acid terminating chains respectively. Open and filled symbols represent the 2nd and 3rd oscillatory modes respectively. Dashed line denotes the theoretical frequency shift, as determined via Equation 5.6 [Lachut07] (b) $\Delta Q/Q_0$ as a function of chain length. (c) $\Delta m/m_0$ as a function of chain length, with areal density illustrated on the right-hand x-axis. Solid lines represent the linear fit. (d) $\Delta D/D_0$ as a function of chain length. Dashed lines denote theoretical prediction, calculated via Equation. 2.5 with thiol*

Young's modulus based on data in Sushko et.al. [Sushko08] and SAM layer thickness determined via ellipsometry. Individual D_n *are calculated for each thiol chain length, and from this* $\Delta D/D_0$ *(i.e.* $(D_n-D_{16}/)D_{16}$*) can be calculated. Error bars have been removed as they are too small to display.*

CHAPTER 5. STIFFNESS AND MASS IN CANTILEVER SENSING IN SOLUTION

Dr. Moyu Watari has previously investigated the molecular basis of stress generation in aqueous environments focusing on the pH titration of model mercaptohexadecanoic acid SAMs [Watari07]. Differential surface stress titration measurements conducted here demonstrated the sensitivity to detect attractive in-plane forces associated with ionic hydrogen bond formation at the apparent surface $pK_{1/2}$ and the electrostatic repulsion between deprotonated carboxylic acid groups at elevated pH. This work also highlighted the dominant role counterions have in the generation of in-plane mechanochemical forces, which controls both the magnitude and direction of cantilever deflection. For future work, it would be interesting to investigate this last point further, alternating a solution's pH to direct cantilever motion. As Watari's work has focussed on static mode measurement [Watari07], it would be interesting to see how this pH-switching method translates into the dynamic mode, and whether dynamic mode cantilevers display the sensitivity necessary to respond to minimal changes in a solution's pH.

Reference	Terminating group	A	B
n=3	CH_3	0.0017 (±0.0010)	0.0306 (±0.025)
n=16	CH_3	0.0040 (±0.00090)	0.031 (±0.021)
n=3	COOH	0.0010 (±0.00090)	0.0179 (±0.029)
n=16	COOH	0.0025 (±0.00011)	0.0201 (±0.028)

***Table 5.2** Mass analysis of SAMs, for n=3 and n=16 references and acid and methyl terminating chains.*

$A \cdot m_0 = (N_{n\geq 3} - N_{n=3})(m_{HS} - m_{CH_2} + m_x) - 3N_{n=3} \cdot m_{CH_2} + (N_{n\geq 3} \cdot m_{CH_2})n$ *and*

$B \cdot m_0 = (N_{n\geq 3} \cdot m_{CH_2})n$. *With m and N denoting mass and number of molecules respectively. Masses are determined from the relative molecular mass, for example* m_{COOH} = *45Da (12+16+16+1). 1 Da=*1.66^{-24}*g.*

If we assume $n = 3$ as the reference, Δm = (*number of molecules*) × ($mass_{n\geq 3} - mass_{n=3}$), A more applicable definition can be written as

$$\Delta m = (N_{n\geq 3} - N_{n=3})(m_{HS} - m_{CH_2} + m_X) - 3N_{n=3} \times m_{CH_2}) + (N_{n\geq 3} \times m_{CH_2})n\,, \qquad 5.5$$

$\Delta m/m_0$ can be defined as $\Delta m/m_0 = A + Bn$, with the exact definitions of A and B given in the caption of Table 5.2. From the mass analysis in Table 5.2 A = $(\Delta N/area) \times m_{n=3}$ and B = $(N_{n\geq 3}/area) \times m_{CH_2}$. For the IBM cantilevers used here, the cantilever area is 500,000 nm^2 × 100,000 nm^2 = 5^{10} nm$^{2.}$

In column A, we can see that, between identical terminating groups, the change in the number of molecules per area is greater when $n = 16$ is used as a reference, compared to $n = 3$. Similarly, column B shows more molecules per area when $n = 16$, for chains of identical terminating group. The difference between these results highlights the importance of selecting a suitable reference. To examine this, n = 16 and n = 3 references have been crossed checked against one another, as shown in Table 5.2.

When comparing results between the same reference but different terminating groups, column A shows the change in the number of molecules per area to be greater in methyl-terminated chains, compared to the acid. (E.g. when $n = 3$, A = 0.0017 for CH_3 and 0.0010 for COOH). When performing a similar comparison in column B, we see a larger number of molecules per area for methyl terminating chains in both $n = 3$ and $n = 16$ references (e.g. when $n = 16$, B = 0.031 for CH_3, but is 0.0201 for COOH). These results could be due to differences in packing between the two chains, as methyl groups are smaller than acid groups, so more chains may fit on to the surface area of the cantilever as the molecules can pack more closely together.

Our results from molecular-systems thus far continue to show adsorbate stiffness having the greatest influence on cantilever sensor response, when operated in liquid. Changes in alkane chain length of 2/3 methyl groups significantly affects cantilever stiffness, giving detectable changes in resonance.

Appendix C details the experimental results for all alkane-thiol cantilever measurements. From the results displayed in this appendix, the measurement values are within a precision of better than 0.1%, with is very high for measurements of this nature (a normal error is in the range of ±2-3%, as seen in Appendix A and B). Due to the complexity of the measurement procedure and analytical methods applied, calculating the error in such experiments is less straight forward, with no one given method accepted as best. The error presented in Appexdix C is based on the standard deviation between results. Whilst this is a well-used method of error analysis, different methods may present a differing, and most likely larger, spread of results.

Can we exploit large changes in stiffness as demonstrated on the SAM, for example to sense the presence and modes of operation of antibiotics? Experiments are extended to vancomycin-mucopeptide systems; where previous work [Ndieyira08] has shown that cantilevers are able to such detect drug-target interactions. The use of nanomechanical cantilever sensors to study this particular binding interaction of interest because glycopeptide antibiotics are thought to disrupt the bacterial cell wall, a mechanical phenomenon. Previous work has demonstrated that, at the molecular level, adsorbate and elastic interactions direct surface stress changes brought about by antibiotics binding to the bacterial cell wall, causing static bending of the cantilevers [Watari06, Ndieyira08, Sushko08]. Cantilevers are coated with either DAla the analogue to the mucopeptide present in the cell walls of VSE (Vancomycin-sensitive Enterococci) strains, or PEG, a thiol terminating in triethylene glycol. This acts as a reference coating and will not bind with the vancomycin.

5.5.4 Vancomycin-mucopeptide complexes

Figure 5.7(a) illustrates the change in cantilever resonance frequency as a function of alkyl-chain length, with the dashed line denoting the stress-related frequency shift prediction, calculated using the same Lachut-Sader equation as previously applied (Equation 2.2) [Lachut07]. In the case of DAla, the relative frequency is shown to increase, up to 100µM vancomycin concentration, after which the response plateaus. At this concentration most accessible vancomycin binding sites are occupied, consistent with binding equilibrium. This increase and plateau trend is in agreement with previous data [Ndieyira08], also occurring at similar concentrations. PEG, known to resist biomolecule adsorption on surfaces [Prime93, Lahiri99] is used as a reference. As binding between vancomycin and PEG does not occur, the relative frequency shift remains minimal. This remains the case in Figures 5.7(b)-(d). Figure 5.7(b) shows the change in quality factor, as a function of vancomycin concentration, with a similar trend observed as in Figure 5.7(a). The error bar for DAla at 500µM vancomycin concentration is seen to be larger compared to other concentrations, due to one outlying quality-factor measurement. From Equation 5.3, it can be seen that any small change in $\Delta Q/Q_0$ will have a large effect on mass determination. At 500 µM [vancomycin], the average $\Delta Q/Q_0$ is 0.028 (Appendix D), with one result for in chip G05 giving a $\Delta Q/Q_0$ of 0.0022 (Appendix D). This factor of 10 difference is reflected in the error bar of the 500µM data point at 500 µM [vancomycin] being larger than those at lower concentrations.

The relative change in mass is shown in Figure 5.7(c), and calculated using Equation 5.3 and shows an increase in DAla mass upon increased vancomycin concentration. Whilst a mass increase is detected upon an increase in vancomycin concentration, we cannot exclude that this trend may be the result of an artefact. A correlation between relative mass change and vancomycin concentration is detected, but this is not necessarily a causative one. The use of smaller, thinner cantilevers is one possible method of increasing the cantilever’s sensitivity to mass, however, as bare gold surface are notoriously problematic due to contamination artefacts, completely overcoming such obstacles remains problematic.

Rigidity results (5.7(d)) again show rigidity to increase up to approximately 100 µM vancomycin concentration and then plateau as the vancomycin-mucopeptide complex reaches saturation. Increases in adsorbate stiffness as vancomycin concentration increases are significant and easily detectable. Vancomycin is approximately 3 × 2 nm (height × width) [Cauda08], with a formula weight of 1.449×10^{-12} nanograms. Considering it's relatively small size and weight, compared to the cantilever, it is worth noting that changes in vancomycin concentration between 10-500 µM bring such detectable changes in cantilever stiffness. This offers a new method of adsorbate detection. Due to their low Young's modulus, dynamic sensors fabricated in the photoresist polymer SU-8, where E_c = 4.0 GPa [Tamayo06], could be potential candidates for resonating sensors with enhanced sensitivity based on molecule stiffness

For all vancomycin data, a Langmuir adsorption isotherm was fitted (Equation 5.6) [Langmuir18]. This model describes the concentration dependent adsorption of molecules on a solid surface and uses the assumption that target-probe binding is independent and unaffected by surface coverage. Assuming the cantilever bending is proportional to surface coverage, the model can be used to describe the concentration dependent surface stress on cantilevers [McKendry02]

$$\Delta\sigma_{eq} = \frac{a \cdot [Vancomycin]}{K_d + [Vancomycin]} , \tag{5.6}$$

where $\Delta\sigma_{eq}$ is the change in cantilever surface stress upon analyte binding. The subscript *eq* denotes equilibrium signals are measured, *a* is the maximum surface stress when all accessible DAla s are bound to a vancomycin molecule, *[Vancomycin]* is the vancomycin solution concentration and K_d is equilibrium dissociation constant on the cantilever surface. By applying Equation 5.6 to the vancomycin- DAla binding experiments, it is possible to calculate K_d, measuring the binding affinity of the antibiotic to the bacterial cell wall peptides on the cantilever surface.

The K_d fit results in Figures 5.7 are: 34 µM for graph (a), 61 µM in graph (b), 20 µM in graph (c) and 49 in graph (d) µM, giving an average of 41 µM and a standard deviation of ±17.83 µM. Previous results have given a vancomycin- DAla a K_d of approximately 1 µM [Nieto71, Cooper00], as well as prior static deflection measurements [Ndieyira08]. Any disruption in vancomycin fluid flow during measurement could reduce binding in the complex, giving a misleading result. For example, if there were an undetected reduction in flow rate, fewer vancomycin molecules than expected would be available to bind onto the receptor. In such an event, a higher vancomycin concentration would be needed in order to create a similar binding (and therefore deflection) effect as seen at a higher flow-rate. As binding constants have an exponential dependence on temperature ($K = e^{-\Delta G / RT}$), any deviations in this during measurements could have a significant impact on binding. Given the factor of 40 discrepancy between the K_d's detected here and those of the literature [Nieto71, Cooper00], it is likely that not just one, but a combination of events contributed to the misalignment in concentrations. More precise temperature controls may be necessary, along with a test of the flow-system within the Veeco Scentris.

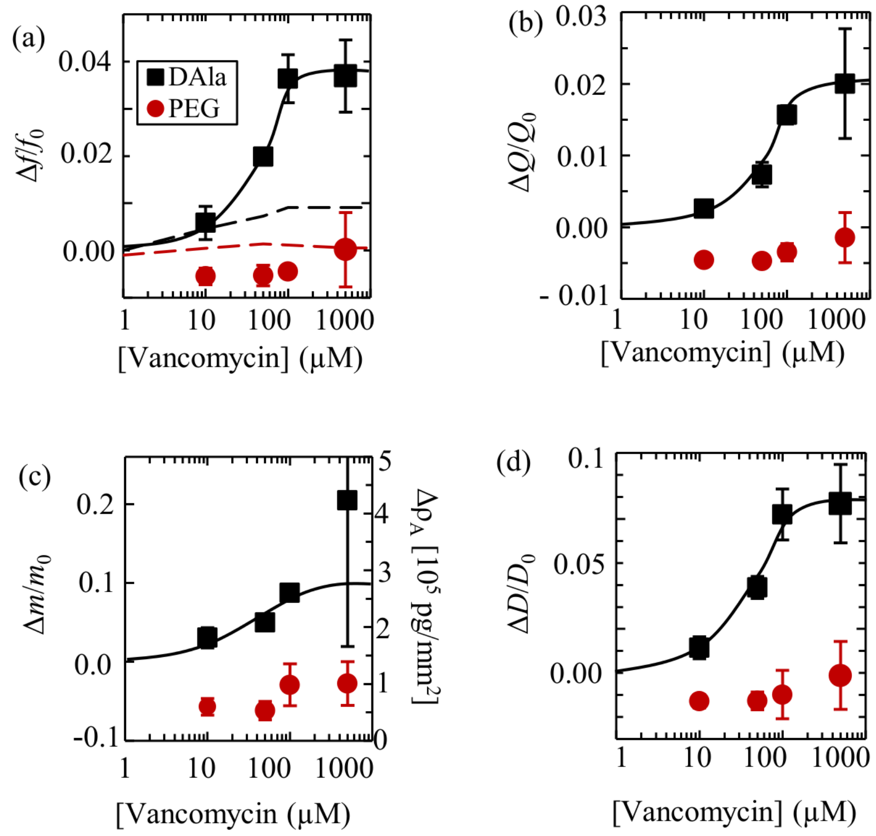

Figure 5.7 *(a) $\Delta f/f_0$ as a function of log Vancomycin concentration. Black and red symbols represent DAla and PEG respectively. Dashed line denotes the theoretical frequency shift, as determined via Equation 5.4 Lachut et. al. [Lachut07].(b) $\Delta Q/Q_0$ as a function of log*

vancomycin concentration. (c) $\Delta m/m_0$ *as a function of chain length, with areal density displayed on the right-hand x-axis. (d)*$\Delta D/D_0$ *as a function of log vancomycin concentration. Langmuir isotherm fits for* DAla *data are represented by a solid line.*

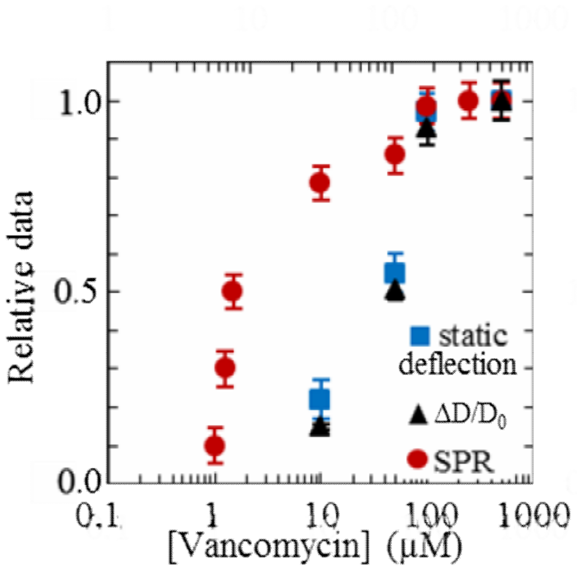

Figure 5.8 *Comparison of normalised SPR, static deflection and rigidity data, as a function of vancomycin concentration. SPR measurements performed by Dr. Manuel Vögtli, past-PhD student of Dr. McKendry's group. Data is normalised to the value at 500 µM vancomycin concentration. for comparison, with values at 500 µM vancomycin being: 200 nm static deflection; 1400 Response Units (pg/mm^2) for SPR and 0.0769 for* $\Delta D/D_0$. *For example, the 10 µM data point at* $\Delta D/D_0$ *= the value for* $\Delta D/D_0$ at *10 µM / the value for* $\Delta D/D_0$ at *500 µM Data at lower [Vancomycin] have not been performed as measurements were initially aiming to investigate the cantilever's sensitivity to mass, and not* K_d, *therefore only higher concentrations were measured.*

A mismatch is apparent between the rigidity data and static deflection here on one side, and SPR data and earlier static deflection data [Ndieyira08] on the other. The typical deflection for 10µM vancomycin- DAla complexes in earlier measurements was approximately 70 nm [Ndieyira08], greater than the 46 nm recorded here at the same concentration. The reduced deflection suggests less binding between vancomycin and DAla has occurred. To achieve deflection closer to the typical levels, a higher concentration of vancomycin would be needed, which in turn would help increase binding. This is consistent with results from Figure 5.7, where a higher concentration is needed in this work in order to produce the same deflection as previous work [Ndieyira08].

As with K_d results discussed from Figure 5.7, this could be due to disruptions in fluid flow and/or temperature effects. Static deflection measurements are to be repeated, however due to time-constraints, this will be done after the submission of this thesis.

5.6 Summary and Conclusions

This chapter presents a method to resolve the sensitivity problems of dynamic-mode cantilever sensors, providing a method to deconvolve adsorbate mass and stiffness effects for cantilevers oscillating in liquid.

Investigation began with determination of the Young’s modulus and mass density in metal layers (Figure 5.4) adsorbed onto the cantilever. Whilst these results demonstrate the application of this model in a simple system, we next examined whether the same dynamic model still holds for adsorbate determination of molecular overlayers, where nanometer-scale coverage can only be guessed, rather than derived from independent measurements.

Previous work has demonstrated the interplay of interactions in influencing the formation and structure of SAMs monolayers [Sushko08]. Alkanethiol systems provide an ideal basis for further testing our dynamic model, as they form well-defined SAMs on gold surfaces, where the surface properties are controlled by the chain length and terminal group [Nuzzo83, Bain89]. Strikingly, we see that only small changes in chain length are needed to produce significant changes in relative cantilever stiffness (Figures 5.5(d) and 5.6(d. This is reflected in the thiols thermal noise spectrum, Figure 5.3. Again results demonstrate the dominance of stiffness over mass in cantilever resonance. It is also important to note that results demonstrate the detection of small mass changes between thiol chain lengths.

The natural progression of these experiments was to continue increasing the complexity of the adsorbed layer, now via the nanomechanical detection of vancomycin. The relative frequency and quality factor shifts for DAla -coated cantilevers increased up to approximately 100 µM [vancomycin], after which the response plateaus as binding sites become occupied. This response was also seen in relative mass and rigidity results. Whilst the mass results demonstrate an expected trend between relative mass increase and increasing vancomycin concentration, this could also be due artefacts. The change in relative rigidity was greater than that of relative mass, demonstrating adsorbate stiffness to dominate the sensor response.

Unfortunately K_d results were not consistent with those previously described, with some experiments needing to be repeated. However results do demonstrate the described method's high sensitivity of to changes in layer stiffness. This offers new potential candidates for future resonating sensors, using materials with a lower Young's modulus than Silicon (i.e. <150 GPa), as these would offer an enhanced sensitivity based on adsorbate stiffness. Polymer cantilevers, made of SU-8, for example [Thaysen02, Calleja05, Tamayo06, Nordstrom08], could therefore be used as a valuable alternative.

In general, thinner cantilevers could be used to achieve a higher sensitivity compared to the beams used here.

CHAPTER 6

Using Cantilevers Sensors to Measure Rheological Properties and Alcohol Content of Model Solutions and Commercial Beverages

6.1 Chapter Overview

Micromechanical resonators provide a small-volume and potentially high-throughput method to determine rheological properties of fluids. In this chapter, the accuracy in measuring mass density and viscosity of ethanol-water and glycerol-water model solutions is discussed. A simple and easily implemented model is applied to deduce the hydrodynamic effects on resonating cantilevers of various length-to-width aspect ratios. Measurements are then extended to determine the alcohol percentage of both model solutions and commercial beverages such as beer, wine and liquor. This demonstrates how micromechanical resonators can be used for quality control of every-day drinks.

CHAPTER 6. USING CANTILEVER SENSORS TO MEASURE RHEOLOGICAL PROPERTIES AND ALCOHOL CONTENT OF MODEL SOLUTIONS AND COMMERCIAL BEVERAGES

6.2 Introduction

The dynamic characteristics of cantilever beams strongly depend on the rheological properties of the fluid in which the beams are immersed. Initial investigation into such fluid effects, using millimeter-sized cantilevers, dates back to the 1960s [Lindholm65]. Following the advent of atomic force microscopy (AFM) twenty years later [Binnig86] and the resulting increase in microcantilever production, these investigations were extended to micro-scale sensors. The resonant behaviour of such microcantilevers is directly related to the fluid viscosity and density, a property which has been used in the measurement of rheological properties [Oden96, Bergaud00, Chon00, Ahmed01, Boskovic02, Hennemeyer08, Dufour11]. Microcantilever or microresonator devices offer the advantage of fast, miniaturized and localized monitoring, using only µL sample requirements, thus providing a valuable means of fluid control whilst also helping to overcome existing measurement problems such as blockages, time consuming calibration processes, expensive equipment costs and sensitivity to vibrations [Steffe96, van den Berg97, Mattos98].

Studies into the density and viscosity of petroleum and silicon oils have demonstrated the commercial potential of micromechanical resonators for rheological measurements [Goodwin06, Belmiloud08, Etchart08, Youssry10]. '*In-situ*' fluid experiments [Goodwin06, Etchart08,] using singly-clamped devices have successfully measured the density and viscosity of petroleum fluids [Goodwin06], with results lying within a ±0.35% and ±3% degree of uncertainty, respectively. Micromechanical resonators have also been used to measure the density and viscosity of glycerol and ethanol solutions [Bergaud00, Ahmed01], calculating a measured ultrapure ethanol of in a measured viscosity of $(1.05 \pm 0.31) \times 10^{-3}$ kg m^{-1} s^{-1} (compared to the expected 1.35×10^{-3} kg m^{-1} s^{-1}) [Bergaud 2000], using Sader's model [Sader98] to relate the cantilever resonance frequency and quality factor to rheological properties.

Density and viscosity measurements have also been demonstrated by Ghatkesar [Ghatkesar08], where the Newtonian fluids (glycerol and ethylene glycerol) were examined. This was achieved via simultaneous measurement of the cantilever's peakfrequency, eigenfrequency and damping due to the surrounding medium. The main findings from this study were: (1) changes in density contribute to the frequency factor shift, which is more prominent at higher modes (Q remains unaffected) and, (2) higher viscosities increases the shear force between liquid layers, and consequently the virtual mass. Such viscosity changes cannot be neglected at higher modes, due to the cantilever's mesoscopic dimensions. Whilst this work studied both density and viscosity effects, this was carried out independently – i.e. one parameter was kept constant whilst the other was changed. Work in this chapter describes the use of microcantilevers to simultaneously measure and independently extract changes in viscosity and density – i.e. both parameters changing at the same time but defined separately.

Biological applications of nanomechanical rheological sensors have also been investigated, for example in characterising sugar solutions [Hennemeyer08] and in monitoring DNA hydrolysis [Ahmed01]. Hennemeyer successfully monitored the change in cantilever resonant frequency and quality factor as a function of increasing sucrose, fructose and glucose solution at biologically relevant concentration, with viscosities determined within an error of less than 5% [Hennemeyer08]. The monitoring of viscosity changes upon the hydrolysis of double stranded DNA by DNase I demonstrates another successful biological sensing application of cantilevers [Ahmed01].

One as yet unexplored application of micromechanical resonators is the measurement of ethanol concentration, density and viscosity of alcoholic beverages. Such measurements form an essential component of product analysis and quality control procedures. A variety of techniques are available for drinks analysis [Cullen00, Wang00], with the requirements associated with real-time, industrial rheological characterisation of fluids being numerous and complex [Cullen00]. These include exposure to aggressive process conditions and high cleanliness requirements. Ideally, sensors should have minimal possibility of fouling and be easily cleaned *in-situ*. In addition, they should offer a fast read-out and require a low sample volume [Cullen00], which is a particular attractiveness of using micromechanical resonators.

Previous studies have investigated to what extent fluid properties and cantilever-length–to-width ratio (aspect ratio) influence the rheological calculations [Chon00, Sader98]. Sader [Sader98] presented the first general theoretical model of the cantilever resonance frequency for a beam of arbitrary cross section, immersed in fluid and excited by an arbitrary driving force. Unlike previous formulations, this model quantitatively accounts for cantilever geometry and additional fluid loading, therefore allowing the frequency response of the beam to be determined based on cantilevers properties and the fluid viscosity and density alone. A key assumption in this model is that the length of the beam must greatly exceed its width, *i.e.*, it has a high aspect ratio. Chon [Chon00] examined this model using a range of cantilevers, each of varying dimensions, immersed in acetone, water, CCl4 and 1-butanol. They found the model to correctly reproduce the frequency response of the cantilevers within an error of 10% for aspect ratio ranges of $l/w = 4 – 14$.

CHAPTER 6. USING CANTILEVER SENSORS TO MEASURE RHEOLOGICAL PROPERTIES AND ALCOHOL CONTENT OF MODEL SOLUTIONS AND COMMERCIAL BEVERAGES

This chapter focuses on the accuracy of such measurements to determine mass density and viscosity of fluids, and in particular to their application for the characterisation of commercial beverages. In that context, one of the key parameters is the alcohol percentage. Different aspect ratios of rectangular cantilevers clamped at one end are first compared, using identical solutions and experimental set-up, to examine the extent by which aspect ratio influences the measurement of density and viscosity. To demonstrate their potential for real-time drinks analysis, measurements are extended to density and viscosity measurements on a range of commercial drinks, comparing previous results to simple aqueous ethanol solutions. Data is then used to determine alcohol content, comparing it to the specifications by the manufacturers. The validity of current theory on more viscous liquids is also investigated, using aqueous glycerol solutions at differing concentrations.

6.3 Binary Water-Alcohol Solutions

As a first examination of the model, simple binary water-ethanol solutions are used at a range of concentrations, from pure water to pure ethanol. Prior studies [Soper93, Dixit02] have indicated that microscopic phase separation and cluster formation dominate the mixing in alcohol–water systems. A schematic of this is shown in Figure 6.1, where amphiphile concentration gradually increases, and clusters (micelles).

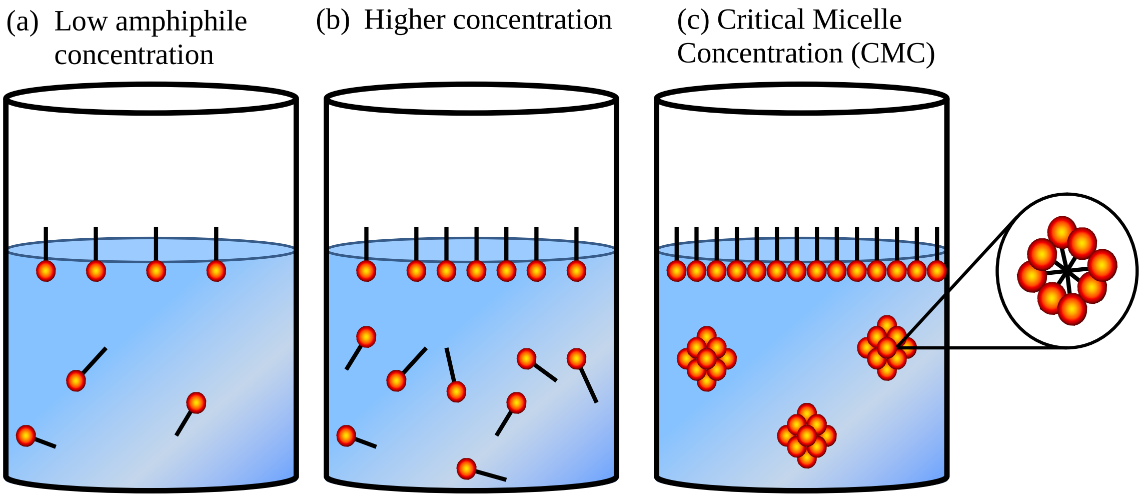

Figure 6.1 *Schematic of increasing amphiphile concentration (e.g. ethanol) from a low concentration (a) to critical micelle concentration (c), where micelle clusters formation occurs.*

The literature values describe the maximum viscosity of water-ethanol solutions being reached at a solution of 42% ethanol, 58% water [Haynes10]. After this point, the viscosity proceeds to decrease, with 0.5% and 100% solutions not varying greatly in their viscosity

(0.001228 kg m^{-1} s^{-1} and 0.001203 kg m^{-1} s^{-1} respectively). The mass density of such solutions is more straightforward, with a decrease from 1000 kg m^3 for 100% water, to 789.3 kg m^3 for 100% ethanol. The sensitivity of microcantilevers to the non-linear behaviour of ethanol viscosity has been demonstrated [Vančura07], where Q initially decreased up to 60% ethanol content, then increasing again up to 100% ethanol solution. This effect was independent of cantilever geometry, where a variety of widths were examined, ranging from186-50μm. Length and thickness remained constant, at 200μm and 8.2μm respectively.

6.4 Current Beverage Analysis Techniques

Measurements of the ethanol content, density and viscosity of alcoholic drinks are essential for drinks analysis and quality control procedures. The food processing environment poses a number of challenges to obtaining rheological measurements. The complex rheological nature of typical fluid foods (including elastic, shear thinning, particulate and highly viscous) calls for robust and innovative sensor designs. Exposure to hostile processing conditions, such as plant vibrations, fouling, cleaning agents and dust pose an additional challenge to instrument design. Ideally, sensors should have minimal possibility of fouling and be easily cleaned *in-situ*. In addition, they should offer a fast read-out and require a low sample volume [Steffe96].

6.4.1 Rheology Analysis

A wide range of methods are available viscosity analysis [Steffe96, Cullen00, Wang03], each suitable to specific circumstances and liquids. Rotational, Vibrational and tube viscometers are the most common types of traditional measuring techniques based upon controlled deformation of the sample.

In rotational viscometery, a cylinder, cone or plate is rotated continuously in the sample liquid and the torque required for rotation at this rate is measured. Viscosity can then be related to the shear stress on the surface of the turning cylinder, divided by shear rate. Rotational viscometers are very sensitive, can operate at low shear rates and are able take precise viscosity measurements [Kawatra95]. However they do have some limitations, for example blockages can occur if particulates are present in the sample, particularly if the gap between the rotating and stationary parts is small.

Vibrational viscometers function by measuring the extent to which the surrounding fluid dampens probe vibration, in proportion to its viscosity and density. Micromechanical resonators can the considered to fit into this class of instrument. The relative simplicity of the probe design makes this technique attractive in viscometer design, proving to be robust, easy to clean *in-situ* and possessing the added advantage of no moving parts.

One of the most commonly applied methods is the glass capillary device, a variation on tube viscometers. Typically these consist of a U-shaped glass structure with a ball-shaped extension, the volume of which determines the quantity of the sample. The dynamic viscosity is obtained by measuring the duration of fluid flow between two points of a capillary of known radius. It is important to note that it is necessary to know the fluid density in order to calculate the viscosity in this manner. Despite their ease of operation and low cost, such methods are subject to observation errors, sample volume requirement of at least 5 ml, slow operation and difficulties with temperature calibration [Steffe96].

6.4.2 Ethanol Determination

Alongside viscosity measurements, the ethanol content of alcoholic drinks must also be accurately determined in order for the product to be sold commercially. Even slight variations in alcohol concentration can influence beverage taste, whilst exact knowledge of its content is also required for taxation purposes. Its content ranges from 7~21% (v/v), 20~50% (v/v), and 3~6% (v/v), in wine, liqueur, and beer respectively. Current methods include: oxidation of the distillate [Caputi69], gas chromatography (GC) [Naviglio01], near-infrared spectroscopy (NIR)[Berg97], high performance liquid chromatography (HPLC) [Kupina84] and flow injection analysis [Wagner 92, Mattos98]. Drawbacks of such methods include expensive equipment costs, comparatively low sensitivity [Steffe96] and time consuming calibration procedures.

6.5 Methods

Measurements are carried out on singly clamped rectangular cantilevers of length, l, width, w, and thickness t_c, oscillating in a viscous medium. The cantilever design and a typical thermal noise measurement are shown in Figure 6.2.

(a)

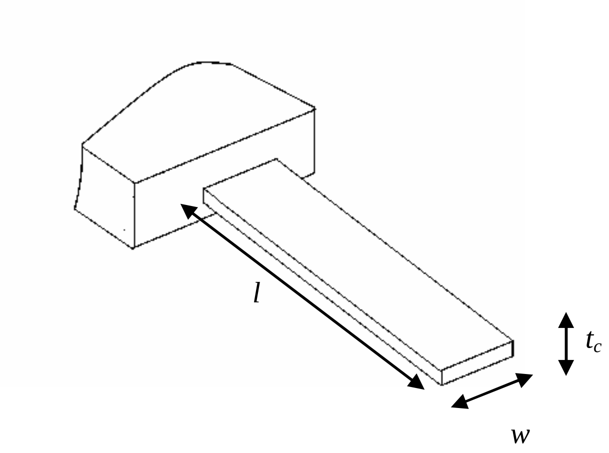
l
t_c
w

(b)

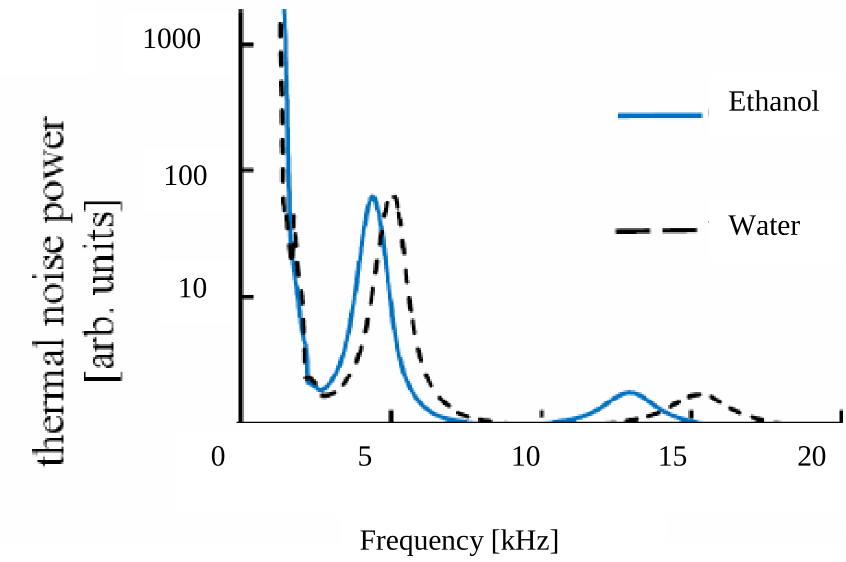
thermal noise power [arb. units]
1000
100
10
Ethanol
Water
0
5
10
15
20
Frequency [kHz]

Figure 6.2 *(a) Schematic of the cantilevers used in fluid measurements. (b) Thermal noise power spectrum for a cantilever of geometry 500 × 100 × 0.9 µm*^{3}*, oscillating in water (black, dashed) and ethanol (blue), plotted against a logarithmic scale. The second and third oscillatory modes are shown, with* $f_{med}^{(n)}$ *and* $Q_{med}^{(n)}$ *typically between 4–5 kHz and 1.5–2 for the second mode and 12–15 kHz and 2.5–3 for the third mode, respectively.*

CHAPTER 6. USING CANTILEVER SENSORS TO MEASURE RHEOLOGICAL PROPERTIES AND ALCOHOL CONTENT OF MODEL SOLUTIONS AND COMMERCIAL BEVERAGES

The relevant mathematical framework for describing the resonance behaviour of a cantilever with length greatly exceeding its width, and width greatly exceeding its thickness, has been developed by others [Sader98]. It is important to note that the model used is strictly valid only for $Q >> 1$. For this reason, the fundamental mode is not taken into consideration, as for the cantilevers used here, its $Q \approx 1$. The main two relevant equations are given in Equations 3.1 and 3.2, while referring to [Sader98] for the explicit form of the used hydrodynamic function $\Gamma(w,\ f_{med}^{(n)}, \rho_{med}, \eta)$.

When oscillated in a liquid of mass density ρ_m and viscosity η, the natural frequency, $f_{med}^{(n)}$, of *n*-th mode of flexural cantilever oscillation is given by (Equation 2.10)

$$f_{med}^{(n)} = f_{vac}^{(n)}\left(1+\frac{\pi\rho_{med}w}{4\rho_c t_c}\Gamma_r(w, f_{med}^{(n)}, \rho_{med}, \eta\right)^{-1/2}, \qquad 6.1$$

where $f_{vac}^{(n)}$ is the resonance frequency of the cantilever in vacuum, ρ_c is its mass density and Γ is the hydrodynamic function for a rectangular beam [Sader98]. This describes the hydrodynamic loading experienced by the cantilever. Subscripts *r* and *i* are used to denote the real and imaginary parts of Γ, respectively. In its simplest form, Γ depends on cantilever width, $f_{med}^{(n)}$ and the density and viscosity of the medium [Sader98]. It is important to note that there are more complex formulations available [Eysden09], extending [Sader98] to 3-D, accounting for increasing mode numbers. In the form used here [Sader98], its accuracy decreases as the mode number increases [Eysden09]. The extended model also includes a formulation for torsional modes, which typically exhibit a higher Q. Here analysis is restricted to the earlier model, since — if sufficiently accurate—it provides a solution with the advantage of simple and straightforward numerical implementation.

According to [Sader98] the effects of viscous damping on the quality factor are (Equations 2.8 and 2.10)

$$Q^{(n)}_{med} = \frac{\dfrac{4\rho_c t_c}{\pi\rho_{med} w} + \Gamma_r(w, f^{(n)}_{med}, \rho_{med}, \eta)}{\Gamma_i(w, f^{(n)}_{med}, \rho_{med}, \eta)} \quad , \qquad 6.2$$

Given the relative simplicity of Γ [Sader98], these set of two implicit equations can be solved numerically to yield the mass density and viscosity of the medium. This is executed using the numerical nonlinear least squares regression algorithm in Mathematica (Wolfram Wolfram Research Inc., Champaign, IL, USA). Calibration of the cantilever is needed to obtain the resonance frequency in vacuum $f^{(n)}_{vac}$ and cantilever thickness t_c with sufficient accuracy in Equations 6.1 and 6.2 [Sader99]. This procedure was outlined by Boskovic [Boskovic02], with air used as the reference medium of known density and viscosity, as done in the measurements presented in this work. When the inertial effects of the fluid are small compared to its dissipative effects (low Reynolds number), such as for soft cantilevers in aqueous solutions, this procedure was found to be less accurate.

Once the mass density and viscosity of the medium have been determined, model solution data can be mapped on the literature values for aqueous ethanol solutions [Haynes10] to find the ethanol (alcohol) percentage. This procedure is tested on pure aqueous ethanol solutions and on a range of beverages, of varying alcohol content. The beverages are measured as purchased, without any further treatment.

CHAPTER 6. USING CANTILEVER SENSORS TO MEASURE RHEOLOGICAL PROPERTIES AND ALCOHOL CONTENT OF MODEL SOLUTIONS AND COMMERCIAL BEVERAGES

For measuring, the cantilever is mounted in a commercial atomic force microscope (Nanowizard I, JPK Instruments, Berlin, Germany) and submerged in 100–200 μL of liquid, where it is subject to thermal fluctuations, which is the only actuation present in these measurements. Optical beam-deflection is employed to monitor cantilever deflections, owing to its relative simplicity and high lateral resolution. A laser is focused on the free end of the cantilever and reflected back onto the position sensitive detector (PSD). Cantilever motion will consequently change the laser position on the photodiode and therefore the light intensity on each cell. Prior to measurement, the laser spot is aligned in the centre of the PSD, so each segment has equal levels of illumination. Ethanol (ACS reagent, ≥99.5%) and glycerol (ACS reagent, ≥99.5%) used to make the required solutions were obtained from Sigma Aldrich (St. Louis, MO, USA). The resonance behaviour of the cantilever is determined from the digitally calculated and averaged Fourier spectrum of the thermal noise of the cantilever. The thermal noise spectrum is then fitted with a simple harmonic oscillator model, via which $f_{med}^{(n)}$ and $Q_{med}^{(n)}$ are determined. Due to the broadness of the peaks, different modes of oscillation are not strictly separated any more in the frequency domain. To enhance the accuracy of the fitting procedure (as described in chapter 2.8), the different modes (up to $n = 3$) are subsequently fitted in the thermal noise spectrum, starting with the first (fundamental) mode, and for each higher mode, fit the thermal noise spectrum after subtracting the fit(s) of the lower mode(s) from the experimental data. This prevents the tails of the lower modes from polluting the fits to the higher modes of oscillation. The fitting procedure is implemented in Mathematica. All measurements are carried out at a temperature of 20.5 °C.

Tipless uncoated single-crystal silicon cantilevers are used, with dimensions: 500 × 100 × 0.9 μm^3, aspect ratio 1:5 [Ghatkesar07] (IBM); 350 × 35 × 1 μm^3, aspect ratio 1:10 (NSC12 tipless cantilevers, MikroMasch, Tallin, Estonia); and 400 × 30 × 2 μm^3, aspect ratio ~1:13 (CLFC-NOBO tipless cantilevers, Bruker Probes, Santa Barbara, CA, USA).

The applicability of the described method in determining the density and viscosity of aqueous ethanol and glycerol solutions, alcoholic drinks and also their alcohol percentage is examined. Investigation also includes the influence of differing aspect ratios in the accuracy of the calculation. Success of this method in determining gas properties has been previously reported [Oden96] so work concentrated on measurements in liquid only. Error bars show the standard deviation between repeat experiments (using different cantilevers of the same type) throughout. Typically, there were five repeats for each condition.

6.6. Results

6.6.1 Ethanol solutions

Figure 6.2 shows the density and viscosity results for the second and third mode of oscillation in aqueous ethanol solutions of 0% (milliQ water), 20%, 40%, 60%, 80% and 100%. Whereas the density simply decreases as the EtOH percent increases, the pattern is less straight forward in the case of viscosity. At first an increase up to around 40% EtOH(aq) solution concentration is seen, followed by a reduction between 40% and 100% EtOH(aq), with experimental data mimicking this pattern. Studies into the non-ideal mixing behaviour of these solutions can be found in the literature [Soper06, Pradhan08]. Our results show identical trends to those expected from literature values [Haynes10], validating the model for detecting changes in fluid properties. As outlined by Sader [Sader98] the length of the beam must greatly exceed its nominal width, an approximation implemented in the theoretical model. It is therefore not surprising that the success of the calculation reduces as the aspect ratio reduces, as seen in *CHAPTER 6. USING CANTILEVER SENSORS TO MEASURE RHEOLOGICAL PROPERTIES AND ALCOHOL CONTENT OF MODEL SOLUTIONS AND COMMERCIAL BEVERAGES*

the measurements. Only for aspect ratios ≥10 do the measured data correspond to the literature values within the experimental accuracy. From Figure 6.3, it can be seen that the low mode numbers used here (n = 2 and n = 3) yield equivalent accuracy.

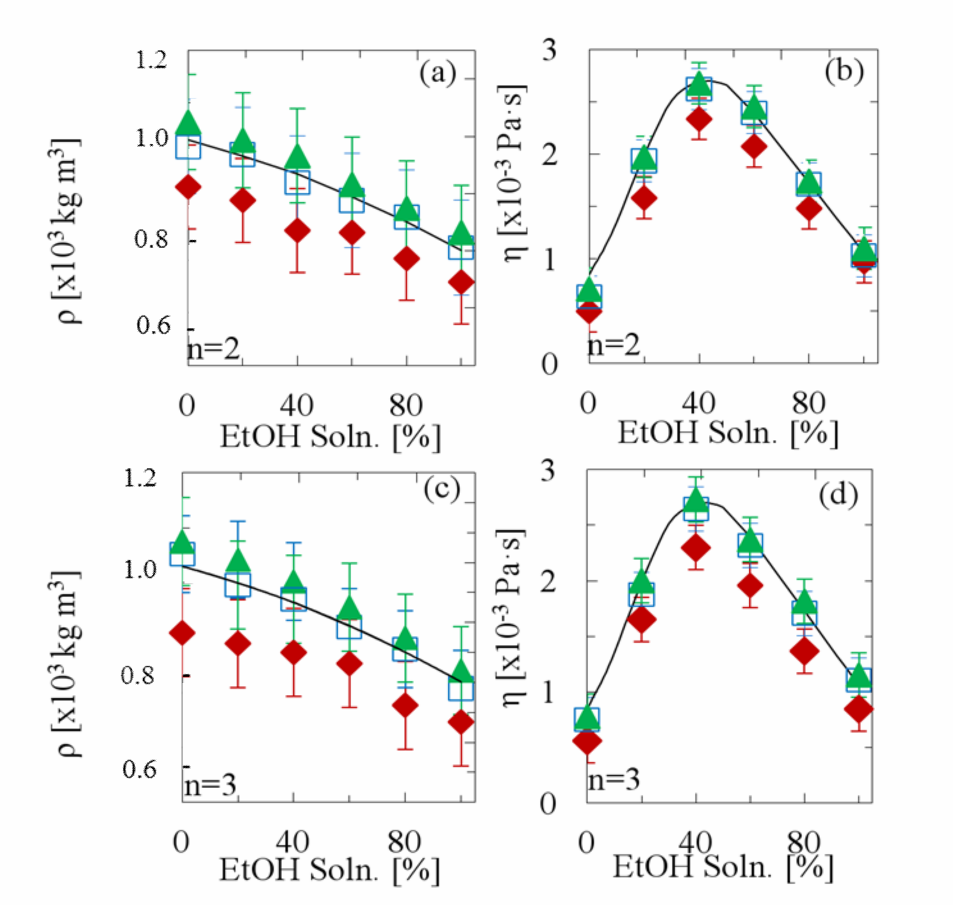

Figure 6.3 *(a) Mass density and (b) viscosity of water-ethanol mixtures, as a function of ethanol volume percentage, determined from the second mode (n = 2) of flexural cantilever oscillation. (c) and (d) show the corresponding results for the third mode (n = 3) of oscillation. The solid line denotes the literature values [Haynes10] at 20 °C. Triangles, squares and diamonds denote aspect ratios of 13:1, 10:1 and 5:1, respectively.*

6.6.2 Glycerol Solutions

The described procedure is repeated for glycerol solutions of the same percentage concentration up to 80%, the results of which are shown in Figure 6.4.

Above 80% concentration, the solution was too viscous for any resonance behaviour to be observed in the thermal noise. Again, the cantilever measurements reproduce the trend expected from the literature values and— in agreement with previous findings [Boskovic02, Sader98] — the lower aspect ratio beam again yields the poorest match. Overall, only for the highest aspect ratio (13:1) do the experimental values and literature values show reasonable agreement within the experimental uncertainty. Interestingly, this agreement is still good for viscosities up to 0.002 kg m^{-1} s^{-1} at 60% glycerol concentration, indicating that—for high aspect ratios—the procedure is reasonably accurate up to the point where viscous damping completely suppresses the resonant behaviour of the cantilever. Nevertheless, the larger viscosity implies a greater infringence on the assumption $Q >> 1$ in analysis, which may be the reason for the slightly larger deviation of measured mass densities and viscosities from the literature values, as compared to the water-ethanol results.

CHAPTER 6. USING CANTILEVER SENSORS TO MEASURE RHEOLOGICAL PROPERTIES AND ALCOHOL CONTENT OF MODEL SOLUTIONS AND COMMERCIAL BEVERAGES **Error! Not a valid link.*****Figure*** *(a) Mass density and (b) viscosity of water-glycerol mixtures, as a function of glycerol volume percentage, determined from the second mode (n = 2) of flexural cantilever oscillation. (c) and (d) show the corresponding results for the third mode (n = 3) of oscillation. The solid line denotes the literature values [Hayes10] at 20 °C. Triangles, squares and diamonds denote aspect ratios of: 13:1, 10:1 and 5:1 accordingly.*

CHAPTER 6. USING CANTILEVER SENSORS TO MEASURE RHEOLOGICAL PROPERTIES AND ALCOHOL CONTENT OF MODEL SOLUTIONS AND COMMERCIAL BEVERAGES

6.6.3 Commercial Beverages

Following on from this, the procedure is applied to the analysis of commercially available non-alcoholic and alcoholic beverages. As previous results have demonstrated the importance of a high (length-to-width) aspect ratio for the cantilever, we only use cantilevers where the length-to-width ratio is 10:1. For smaller aspect ratios, measurements for both mass density and viscosity will become increasingly inaccurate, as can be observed in Figure 6.3.

Figure 6.5 shows density and viscosity measurements for a range of drinks. These are: beer, non-alcoholic beer, white wine, vodka, whisky and gin. We then use these values to determine the alcohol content. Upon application to alcoholic drinks, we find a good agreement between experimental and interpolated water/ethanol solution values for density and viscosity. By comparing the thus determined rheological properties to values for ideal water-ethanol solutions as measured previously, we determine the alcohol percentage in the beverages, and find these in good agreement with the manufacturers' specifications (Figure 6.5). The alcohol content could be determined from the mass density and from the viscosity separately, though the uncertainties are such that the viscosity is a far more accurate indicator of alcohol content for these beverages. Deviations from the expected values could be due to the interplay of other components within the drink, for example glycerol content, of which ranges from 5–7 g/L in wine [Mattick70], 0.9–2 g/L in beer [Oliveira06] and higher in spirits, where the alcohol percentage is greater.

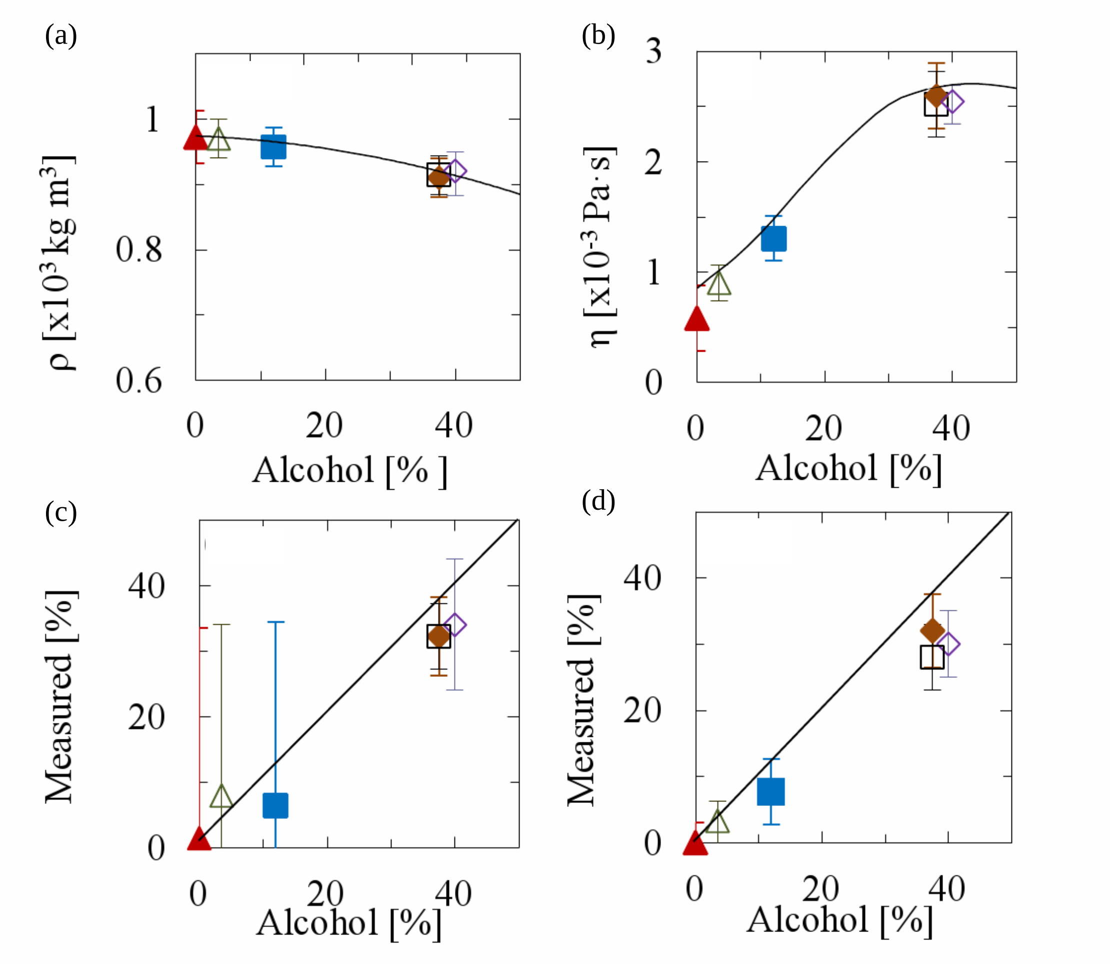

Figure 6.5 *(a) Measured mass density and (b) viscosity of commercial beverages as a function of specified alcohol content. (c) and (d): Alcohol percentage determined from the measured mass density (c) and viscosity (d) as a function of specified alcohol content. Symbols: triangle—non-alcoholic beer; open triangle—3.5% beer; square—12.5% white wine; open square—37.5% gin; diamond—37.5% vodka; open diamond—40% whisky. Solid lined denotes interpolated water/ethanol data from Figure 6.3.*

6.7 Summary and Conclusions

In summary, we have experimentally demonstrated the use of micromechanical cantilever sensors to extract the density and viscosity of simple binary laboratory solutions and of more complex commercial drinks. We have also demonstrated that alcohol content in beverages can be determined from such measurements. As expected, the accuracy of the measurements decreases with decreasing (length to width) aspect ratio of the cantilever. This is important when considering industrial applications, where margin for error is minimal.

The accuracy of the technique could be further improved by using cantilevers of a higher aspect ratio. Figures 6.3 and 6.4 illustrate the importance of this, showing a clear variation across geometries. The differences between experimental mass densities and literature values is on average 16% for 5:1 aspect ratio cantilevers; however this is significantly reduced to 4% for the longer beams. A similar scenario is seen with the viscosity measurements, where the differences between literature and experimental values for the 5:1 and 13:1 aspect ratios are 25% and 6%, respectively. On the other hand, the results in Figure 6.5 show that such deviations can be avoided by calibrating the mass density and viscosity measurements in model solutions. The main uncertainty would thus be in variations in the curve fitting, temperature and cantilever geometry, for all of which there is large scope for improvement by standardisation and repeat measurements, as well as by fitting both amplitude and phase of the resonance response to external actuation (as opposed to thermal fluctuations) The main scope for improvement in the described technique lies within the read-out method. Here cantilever deflection is measured via an optical read-out system, limiting the technique to transparent liquids and also reducing its use as a portable device. This could be overcome via the use of piezoelectric or piezoresistive cantilevers, or other schemes that bypass the need of optical detection.

CHAPTER 7

Conclusions and Outlook

This thesis investigates the nature and applications of resonant cantilever sensing. By gaining a greater understanding of the sensor response, we are able to turn apparent disadvantages of dynamic mode sensing into potential assets.

As a first model to investigating the sensor response, nm-thick metallic films were evaporated onto the cantilever surface. The comparison of the thermal noise spectrums before and after coating yielded the important result that the sensor response to identical adsorbates fundamentally differs for cantilevers oscillated in air and in water. In air, the sensor response to the added mass was that expected for a harmonic oscillator: an increase in added mass reduced the cantilever's resonance frequency. However this situation was reversed in water, where the observed resonance frequency *increased* upon mass addition. This initial result demonstrated that the sensor response is not simply due to increased mass effects alone, but is in fact a convolution of mass, rigidity and the nanoscale heterogeneity of adsorbates. In order to optimise the use of cantilevers as sensors, it is essential to disentangle this complex sensor response, turning a disadvantage of current sensing procedures into an asset by enabling simultaneous measurement of more than mass alone.

In disentangling the sensor response in fluid, its sensitivity to the mass density and to viscosity of the surrounding medium was also investigated. The ability to quantify these properties has been presented, along with how this is influenced by cantilever geometry. Their application in determining the alcoholic content of everyday alcoholic drinks has also been shown, a procedure vital in industrial analysis, production and quality control.

This chapter summarises key results from this thesis, along with scope for future investigation.

7.1 Disentanging Mechanical and Mass Effects of Metallic Thin Film Adsorbates on Nanomechanical Resonators Operated in Air

When gold-coated cantilevers were operated in air, experimental data were found to deviate from the predicted response due to the added-mass only. They perfectly matched, however, the theoretical curves for added mass *and* changed rigidity. In water, the effective mass of the bare cantilevers is increased [Ghatkesar08] due to added fluid mass. This reduces the relative importance of the added gold mass and thus causes the cantilever to respond as if the gold films only influence the cantilever rigidity, without increasing its mass.

In the case of copper films in air, the cantilever response was dominated by mass effects for films formed of isolated islands. On increasing film thickness, the islands coalesced, causing the frequency shifts deviate from the mass-only prediction, and finally reaching the mass and rigidity prediction for a homogeneous copper coverage. This is because at a lower coverage, the copper islands do not interact, therefore the layer will not influence the stiffness of the resonator and only the mass.

Two important findings are presented in this chapter: (i) adsorbate mass can be accurately determined by combining the resonance frequencies and quality factors of micromechanical resonators, also when the resonator response results from a combination of added mass and rigidity, and (ii) such measurements can be used to measure both adsorbate mass and elastic properties. This is particularly useful in determining how the properties of thin films deviate from bulk behaviour. Such measurements also enable simultaneous measurement of the presence of adsorbate and elastic interactions within it.

7.2 Stiffness and Mass in Cantilever Sensing in Solution

Chapter five extends upon the ideas of chapter four, now investigating the effects of metal and molecular adsorbates for cantilevers oscillated in liquid.

The thermal noise spectrum for metal-coated cantilevers in water showed an increase in layer thickness to produce changes in resonance frequencies and quality factors. The inclusion of a simplified hydrodynamic function [Sader98] permitted the implicit equation for $f_{res}^{(n)}$ (Equation 5.1) to be solved numerically via a nonlinear least squares regression algorithm.

Once $f_{res}^{(n)}$ was determined, calculation of the corresponding quality factor was relatively straightforward. The thus calculated predictions were verified by comparison to the experimental results. Next, a reverse procedure was developed to determine the a-priori unknown mass and elastic properties of the adsorbate. The results in this thesis demonstrate that the described procedure can be successfully applied to extract the experimental adsorbate mass and Young’s modulus of nm-thick metallic films, with results lying within experimental error for expected literature values [Haynes10].

Molecular sensing applications of micromechanical sensors were next investigated, applying the outlined dynamic model to SAMs and vancomycin-mucopeptide complexes.

The influence of adsorbate stiffness on cantilever resonance can be clearly observed in the thermal noise spectrum of methyl-terminated alkane-thiol chains of varying length. The C3 chain showed the highest resonance frequency, when compared to the C8, C11 and C16 chain lengths. A theory to explain this phenomenon is also presented in this chapter, with the structure of the hydrocarbon layer being determined by the interplay of the interactions between the molecules of the gold substrate and intermolecular forces. As was the case for the metal films, the effect of stiffness changes due to the adsorbed SAMs was shown to greatly dominate mass effects when in water. This was reflected in the frequency and quality factor shifts following identical trends as the Young's modulus upon increasing alkane-thiol chain length. In both methyl and acid terminating chains, the 8-carbon chains have been calculated as having the lowest Young's modulus, with respect to C3, C11 and C16 chains [Sushko08], with the Young's modulus increasing between C8-C16. Experimental results presented in this chapter follow an identical trend, demonstrating the overriding and surprisingly large influence of rigidity effects.

Vancomycin-mucopeptide systems were next invested. The relative frequency and quality factor shifts for DAla -coated cantilevers were seen to increase up to approximately 100µM vancomycin concentration, after which the response plateaus. This suggests that at this concentration, most accessible vancomycin binding sites are occupied. PEG, known to resist biomolecule adsorption [Prime93, Lahiri99] was used as a reference, as binding between vancomycin and PEG does not occur. These trends in DAla and PEG were also observed in the relative mass and rigidity shift results.

With regards to mass detection, results demonstrated that whilst the mass change is too small to be calculated accurately, for the DAla results, a mass increase is clearly present as vancomycin concentration increases. A greater change in relative rigidity was seen between 10 – 500 µM vancomycin concentrations, compared to changes in relative mass. This further confirms previous results of adsorbate stiffness dominating sensing.

Calculation of the dissociation constant gave a K_d greater than expected. A mismatch was also apparent between the static deflection measurements on one side, and SPR and earlier static deflection data on the other. Such a deviation could be due to disruption in vancomycin fluid flow during measurement. This in turn could reduce binding in the complex, giving a misleading result. Furthermore, as binding constants have an exponential dependence on temperature, any deviations in this during measurements could have a significant impact on binding. These measurements are therefore to be repeated.

Overall the results show changes in cantilever stiffness due to monolayer adsorption dominate resonance, giving detectable changes. Results also demonstrate how small changes in molecular structure, such as the addition/removal of a few methyl groups from the alkane-thiol chain, can produce significant changes in the thiol's mechanical properties. It would be interesting to gain a more quantitative understanding of this phenomenon and this is one area where there is scope for future work.

7.2.1 Future Work

For the molecular monolayers tested, the interface elastic properties differ from bulk properties, as cantilever bending suggests molecular rearrangement and not only a variation in bond lengths. It would be interesting to gain a greater understanding into the origins surrounding the large effects on rigidity caused by per-thousand changes in overall cantilever thickness.

Our analysis in terms of simple beam theory has produced large values for the axial elastic modulus (Young's modulus). It would be interesting to compare these results with the numerical values for the (axial) Young's modulus. One method of calculating this would be via an atomistic model, as used to quantify the biaxial elastic modulus of the gold surface with chemisorbed SAMs by Sushko *et. al.* [Sushko08]. Here calculations were performed using 2D boundary conditions with molecular mechanics and molecular dynamics methods.

It would also be of use to determine the elastic energy density as a function of vertical (perpendicular to cantilever surface) position, for a small cantilever bending, coated with the n=3, 8, 11 and 16 and COOH and CH3 terminal groups. This could help provide a more quantitative argument surrounding the relative importance of chain-chain interactions and chain-surface interactions.

These questions are currently being investigated in collaboration with Dr. Maria Sushko, a previous researcher at the LCN. The addition of such analysis will help provide a more quantitative understanding into the physics of nanomechanical biosensing.

7.3 Using Cantilevers Sensors to Measure Rheological Properties and Alcohol Content of Model Solutions and Commercial Beverages

The application of dynamic cantilever sensors in determining the density and viscosity of ethanol and glycerol solution further exemplifies the versatility of this technology.

An example of the sensitivity of resonating cantilevers to the surrounding medium was illustrated in their response to changing ethanol concentrations. In the literature, [Haynes10] ethanol viscosity is described to first increase, up to approximately 40% EtOH concentration. After this point the viscosity reduces until ethanol concentration is 100%. This trend in viscosity was reproduced in calculations outlined in chapter six, validating the procedure’s application and sensitivity in detecting of changes in fluid properties.

Oscillation of the cantilever beam in glycerol solutions of various concentrations found the experimentally determined values for fluid density and viscosity to once again match well with the literature [Hayes10]. The larger viscosity of this solution, compared to ethanol, implies a greater infringence on the assumption $Q >> 1$ in analysis. This may help explain the occurrence of slightly larger deviations between the literature values and measured mass density and viscosity in the case of these solutions.

Application of the same fluid-analysis procedure to alcoholic drinks gave a good agreement between experimental and interpolated water/ethanol solution values for density and viscosity. By comparing the thus determined rheological properties to values for ideal water-ethanol solutions as measured previously, the alcohol percentage for a range of drinks was successfully determined, and found to be in good agreement with the manufacturers' specifications.

A further aim of these experiments was to study the effects of changing aspect ratio ($l : w$) in influencing the accuracy of determining the fluid's properties. The accuracy of the results was found to decrease upon decreasing aspect ratio. As outlined by Sader [Sader98] the length of the beam must greatly exceed its nominal width, an approximation implemented in the theoretical model applied in chapter six. It is therefore not surprising that the success of the calculation reduces as the aspect ratio does so. For ethanol solutions, an aspect ratio of ≥10 was needed in order for the measured data to correspond to the literature values, within experimental accuracy. In in the case of glycerol, only the highest aspect ratio (13:1) displayed a reasonable agreement between the experimental and literature values. This agreement still held for viscosities up to 0.002 kg m^{-1} s^{-1} at 60% glycerol concentration, indicating that—for high aspect ratios—the procedure applied is suitably accurate up to the point where viscous damping fully suppresses cantilever's resonant behaviour.

7.3.1 Future Work

Results have shown cantilever aspect ratio to significantly influence the accuracy of determining a fluid's properties. Therefore the use of cantilevers with a higher aspect ratio is one key area for future investigation. Such a problem will also be enhanced if the beams become thinner, a further way of improving sensor sensitivity.

The main source of uncertainty in these measurements include: fitting of the thermal noise curve; temperature and cantilever geometry. Each of these offer some scope for improvement by standardization and repeat measurements, along with fitting both amplitude and phase of the resonance response to external actuation, as opposed to thermal fluctuations.

Thermal fluctuations are measured via optical deflection with a position sensitive detector. This offers the main scope for improvement in the described technique, as analysis is restricted to transparent liquids. The nature of thermal fluctuations also prevents the device from being portable. In order to maximise this technologies potential, it would be essential to overcome this, typically via the use of piezoelectric or piezoresistive cantilevers, or other schemes that bypass the need of optical detection.

Bibliography

[Ahmed01]	N. Ahmed, D. F. Nino, and V. T. Moy, Measurement of solution viscosity by atomic force microscopy, *Review of Scientific Instruments*, 72(6): 2731 – 2734, 2001.
[Albert00]	K. J. Albert, N. S. Lewis, C. L. Schauer, G. A. Sotzing, S. E. Stitzel, T. P. Vaid, and D. R. Walt. Cross-Reactive Chemical Sensor Arrays, *Chemical Review*, 100(7): 2595–2626, 2000.
[Antonelli94]	A. Antonelli. Ethanol determination by packed GLC: a quick method with small sample amount and high sensitivity. *Viticulture and Enology Science* 49: 165-167, 1994.
[Arntz03]	Y. Arntz, J. D. Seelig, H-P. Lang, J. Zhang, P. Hunziker, J. P. Ramseyer, E. Meyer, M. Hegner and C. Gerber. Label-free protein assay based on a nanomechanical cantilever array. *Nanotechnology*, 14(1): 89-90, 2003.
[Backmann05]	N. Backmann, C. Zahnd, F. Huber, A. Bietsch, A. Plückthun, H-P. Lang, H-J. Güntherodt, M. Hegner and C. Gerber. A label-free immunosensor array using single-chain antibody fragments. *Proceedings of the National Academy of Sciences of the United States of America*, 102(41): 14587-14592, 2005.

[Bain89] C. D. Bain, H. A. Biebuyck, and G. M. Whitesides. Comparison of self-assembled monolayers on gold: co-adsorption of thiols and disulfides. Langmuir, 5:723–727, 1989.

[Belmiloud08] N. Belmiloud, I. Dufour, A. Colin and L. Nicu. Rheological behaviour probed by vibrating microcantilevers. *Applied Physics Letters*, 92(4): 041907-1 - 041907-3, 2008.

[Benouattas06] N. Benouattas, A. Mosser, A. Bouabellou. Surface morphology and reaction at Cu/Si interface—Effect of native silicon suboxide. *Applied Surface Science*, 252(20): 7572–7577, 2006.

[Berg97] F. W. J van den Berg, W. A. van Osenbruggen, A. K. and Smilde. Process analytical chemistry in the distillation industry using near-infrared spectroscopy, *Process Control and Quality*, 9: 51-57, 1997.

[Bergaud00] C. Bergaud and L. Nicu. Viscosity measurements based on experimental investigations of composite cantilever beam eigenfrequencies in viscous media. *Review of Scientific Instruments*, 71(6): 2487 – 2491, 2000.

[Berger97] R. Berger, Ch. Gerber, H.P. Lang and J.K. Gimzewski. Micromechanics: A toolbox for femtoscale science: ‘Towards a laboratory on a tip’. *Microelectronic Engineering*, 35(1-4): 373-379, 1997.

[Betts00] T. A Betts, C. A Tipple, M. J Sepaniak and P. G. Datskos. Selectivity of chemical sensors based on micro-cantilevers coated with thin polymer films. *Analytica Chimica Acta*, 422(1): 89-99, 2000.

[Binning86] G. Binning, C. F. Quate and C. Gerber. Atomic Force Microscope. *Physical Review Letters*, 56(9): 930-933, 1986.

[Braun05] T. Braun, V. Barwich, M. K. Ghatkesar, A. H. Bredekamp, C. Gerber, M. Hegner and H-P. Lang. Micromechanical mass sensors for biomolecular detection in a physiological environment. *Physical Review E: Statistical, Non-Linear and Soft Matter Physics*, 72(3): 031907-1 - 031907-9, 2005.

[Braun09] T. Braun, M. K. Ghatkesar, N. Backmann, W. Grange, P. Boulanger, L. Letellier, H-P. Lang, A. Bietsch, C. Gerber and M. Hegner. Quantitative time-resolved measurement of membrane protein–ligand interactions using microcantilever array sensors. *Nature Nanotechnology,* 4(3): 179-185, 2009.

[Bruckstein85] S. Bruckenstein and M. Shay. Experimental aspects of use of the quartz crystal microbalance in solution. *Electrochimica Acta*, 30(10): 1295-1300, 1985.

[Burg03] T. P. Burg and S. R. Manalis, Suspended microchannel resonators for biomolecular detection. *Applied Physics Letters*, 83(13): 2698 – 2700, 2003.

[Burg07] T. P. Burg, M. Godin, S. M. Knudsen, W. Shen, G. Carlson, J. S. Foster, K. Babcock and S. R. Manalis. Weighing of biomolecules, single cells and single nanoparticles in fluid. *Nature*, 446(7139): 1066-1069, 2007.

[Burikov10] S. Burikov, T. Dolenko, S. Patsaeva, Y. Starokurov and V. Yuzhakov. Raman and IR spectroscopy research on hydrogen bonding in water–ethanol systems. *Molecular Physics*, 108(18): 2427-2436, 2010.

[Calleja05] M. Calleja, M. Nordström, M. Álvarez, J. Tamayo, L.M. Lechuga and A. Boisen. Highly sensitive polymer-based cantilever-sensors for DNA detection. *Ultramicroscopy,* 105(1): 215-222, 2005.

[Caputi69] A. Caputi Jr. and D. Wright, D., Collaborative study of the determination of ethanol in wine by chemical oxidation. *Journal - Association of Official Analytical Chemists*, 52, 85–88, 1969.

[Carey86] W. P. Carey, K. R. Beebe, B. R. Kowalski, D. L. Illman and T. Hirschfeld. Selection of adsorbates for chemical sensor arrays by pattern recognition. *Analytical Chemistry*, 58(1): 149-153, 1986.

[Cauda08] V. Cauda, B. Onida, B. Platschek, L. Mühlstein and T. Bein. Large antibiotic molecule diffusion in confined mesoporous silica with controlled morphology. *Journal of Material Chemistry*, 18(48): 5888-5899

[Chapman07] P. J. Chapman, F. Vogt, P. Dutta, P. G. Datskos, G. L. Devault and M. J. Sepaniak. Facile Hyphenation of Gas Chromatography and a Microcantilever Array Sensor for Enhanced Selectivity. *Analytical Chemistry*, 79(1): 364-370, 2007.

[Chen94] G. Y. Chen, R. J. Warmack, T. Thundat, D. P. Allison and A. Huang. Resonance response of scanning force microscopy cantilevers. *Review of Scientific Instruments*, 65(8): 2532-2537, 1994.

[Chen95] G. Y. Chen, T. Thundat, E. A. Wachter and R. J. Warmack. Adsorption-induced surface stress and its effects on resonance frequency of microcantilevers, *Journal of Applied Physics*, 77(8): 3618-3622, 1995.

[Chon00] J. M. W. Chon, P. Mulvaney and J. Sader. Experimental validation of theoretical models for the frequency response of atomic force microscope cantilever beams immersed in fluids. *Journal of Applied Physics*, 87(8): 3978-3988, 2000.

[Chu63] W. H. Chu, South-West Research Institute Technical Report 2 (1963).

[Cleveland93] J. P. Cleveland, S. Manne, D. Bocek and P. K. Hansma. A nondestructive method for determining the spring constant of cantilevers for scanning force microscopy. *Review of Scientific Instruments*, 64(2): 403-405, 1993.

[Cooper00] M. A. Cooper, M. T. Fiorini, C. Abell, and D. H. Williams. Binding of vancomycin group antibiotics to -alanine and -lactate presenting self-assembled monolayers. *Bioorganic & Medicinal Chemistry*, 8:2609–2616, 2000.

[Cullen00] P. J. Cullen, A. P. Duffy, C. P. O'Donnell and D. J. O'Callaghan, Process viscometry for the food industry. *Trends in Food Science and Technology*, 11(12): 451-457, 2000.

[Datskos01] P.G Datskos, M.J Sepaniak, C.A Tipple and N Lavrik. Photomechanical chemical microsensors, *Sensors and Actuators B: Chemical*, 76(1-3): 393-402, 2001.

[Davis00] Z. J. Davis, G. Abadal, O. Kuhn, O. Hansen, F. Grey, and A. Boisen. Fabrication and characterisation of nanoresonating devices for mass detection. *Journal of vacuum science & technology. B, Microelectronics and nanometer structures processing, measurement and phenomena*, 18(2): 612-616, 2000.

[Dickenson98] T. A Dickinson, J. White, J. S Kauer and D. R Walt. Current trends in 'artificial-nose' technology. *Trends in Biotechnology*, 16(6): 250-258, 1998.

[Dintenfass69] L. Dintenfass and A. Sharp. Dynamic blood coagulation, thrombus formation and degradation in patients with peripheral vascular disease (arteriosclerosis, including diabetic): an in vitro study. *Annals of Surgery*, 170(6): 984–995, 1969.

[Dohn05] S. Dohn, R. Sandberg, W. Svendsen and Anja Boisen. Enhanced functionality of cantilever based mass sensors using higher modes. *Applied Physics Letters*, 86(23): 233501-01 – 233501-03, 2005.

[Dorignac06] J. Dorignac, A. Kalinowski, S. Erramilli and P. Mohanty. Dynamical Response of Nanomechanical Oscillators in Immiscible Viscous Fluid for *In Vitro* Biomolecular Recognition. *Physical Review Letters*, 96(18): 186105-01 - 186105-04, 2006.

[Dostálek05] J. Dostálek, H. Vaisocherová, J. Homola, Multichannel surface plasmon resonance biosensor with wavelength division multiplexing. *Sensors and Actuators B: Chemical*, 108(1): 758-764, 2005.

[Dueck 10] B. Dueck. Robust Optical Diffractive Technique to Read Out Cantilever Detection. Ph.D. thesis, University College London, 2010.

[Dufour11] I. Dufour, A. Maali, Y. Amarouchene, C. Ayela, B. Caillard, A. Darwiche, M. Guirardel, H. Kellay, E. Lemaire, F. Mathieu, C. Pellet, D. Saya, M. Youssry, L. Nicu and A. Colin. The Microcantilever: A Versatile Tool for Measuring the Rheological Properties of Complex Fluids. *Journal of Sensors*, Article ID 719898, 1-9, 2011.

[Elmer97] F.-J. Elmer and M. Dreier. Eigenfrequencies of a rectangular atomic force microscope cantilever in a medium. *Journal of Applied Physics*, 81(12): 7709-7714, 1975.

[Escovitz75] W. H. Escovitz, T. R. Fox and R. Levi-Setti. Scanning Transmission Ion Microscope with a Field Ion Source. *Proceedings of the National Academy of Sciences of the United States of America*, 72(5): 1826-1828, 1975.

[Etchart08] I. Etchart, H. Chen, P. Dryden, J. Jundt, C. Harrison, K. Hsu, F. Marty and B. Mercier. MEMS sensors for density–viscosity sensing in a low-flow microfluidic environment *Sensors and Actuators A: Physical*. 141(2): 266-275, 2008.

[Eysden09] C. A. Van Eysden and J. E. Sader. Frequency response of cantilever beams immersed in compressible fluids with applications to the atomic force microscope. *Journal of Applied Physics*, 106(9): 094904-01 – 094904-08, 2009.

[Finot08] E. Finot, A. Passian and T. Thundat. Measurement of Mechanical Properties of Cantilever Shaped Materials. *Sensors*, 8(5): 3497-3541, 2008.

[Fritz00] J. Fritz, M. K. Baller, H-P. Lang, H. Rothuizen, P. Vettiger, E. Meyer, H-J. Güntherodt, C. Gerber and J. K. Gimzewski. Translating Biomolecular Recognition into Nanomechanics. *Science*, 288(5464): 316-318, 2000.

[Ftitz00b] J. Fritz, M. K. Baller, H. P. Lang, T. Struntz, E. Meyer, H-J. Güntherodt, E. Delamarche, C. Gerber and J. K. Gimzewski. Stress at the solid-liquid interface of self-assembled monolayers on gold investigated with a nanomechanical sensor. *Langmuir*, 16(25): 9694-9696, 2000.

[Fritz02] J. Fritz, E. B. Cooper, S. Gaudet, P. K. Sorger and S. R. Manalis, Electronic detection of DNA by its intrinsic molecular charge. *Proceedings of the National Academy of Sciences of the United States of America*, 99(22): 14142-14146, 2002.

[Gfeller05] K. Y. Gfeller, N. Nugaeva and Martin Hegner. Micromechanical oscillators as rapid biosensor for the detection of active growth of Escherichia coli. *Biosensors and Bioelectronics*, 21(3): 528-533. 2005.

[Ghatkesar04] Murali K. Ghatkesar, V. Barwich, T. Braun, A.H. Bredekamp, U. Drechsler, M. Despont, H. P. Lang, M. Hegner, and C. Gerber. Real-Time Mass Sensing by Nanomechanical Resonators in Fluid. *Proceedings of IEEE, Sensors*, 4(2): 1060 – 1063, 2004.

[Ghatkesar07] M. K. Ghatkesar, V. Barwich, T. Braun, J-P. Ramseyer, C. Gerber, M. Hegner, H-P. Lang, U. Drechsler and M. Despont. Higher modes of vibration increase mass sensitivity in nanomechanical microcantilevers, *Nanotechnology*, 18(44): 445502-01 – 445502-08, 2007.

[Ghatkesar08] M. K. Ghatkesar, T. Braun, V. Barwich, J-P. Ramseyer, C. Gerber, M. Hegner, and H-P. Lang. Resonating modes of vibrating microcantilevers in liquid. *Applied Physics Letters*, 92(4): 043106-01 – 043106-03, 2008.

[Gimzewski94] J. K. Gimzewski, C. Gerber, E. Meyer and R. R. Schlittler. Observation of a chemical reaction using a micromechanical sensor. *Chemical Physics Letters*, 217(5): 589-584, 1994.

[Goodwin06] A. R. H. Goodwin, A. D. Fitt, K. A. Ronaldson and W. A. Wakeham. A Vibrating Plate Fabricated by the Methods of Microelectromechanical Systems (MEMS) for the Simultaneous Measurement of Density and Viscosity: Results for Argon at Temperatures Between 323 and 423K at Pressures up to 68 MPa. *International Journal of Thermophysics*, 27(6): 1650-1676, 2006.

[Grate91] J. W. Grate and M. H. Abraham. Solubility interactions and the design of chemically selective sorbent coatings for chemical sensors and arrays. *Sensors and Actuators B: Chemical*, 3(2): 85-111, 1991.

[Grate93] J. W. Grate, S. J. Martin and R. M. White. Acoustic wave microsensors. *Analytical Chemistry*, 65(21): 940-948, 1993.

[Grüter10] R. R. Grüter, Z. Khan, R. Paxman, J. W. Ndieyira, B. Dueck, B. A. Bircher, J. L. Yang, U. Drechsler, M. Despont, R. A. McKendry and B. W. Hoogenboom. Disentangling mechanical and mass effects on nanomechanical resonators. *Applied Physics Letters*, 96(2): 023113-1 – 023113-3, 2010.

[Godin04] M. Godin, P. J.Williams, V. Tabard-Cossa, O. Laroche, L. Y. Beaulieu, R. B. Lennox, and P. Grütter Surface stress, kinetics, and structure of alkanethiol self-assembled monolayers. *Langmuir*, 20(17): 7090-7096, 2004.

[Goeders08] K. M. Goeders, J. S. Colton and L. A. Bottomley. Microcantilevers: Sensing chemical interactions via mechanical motion. *Chemical Review*, 108(2): 522–542, 2008.

[Gupta06] A. K. Gupta, P. R. Nair, D. Akin, M. R. Ladisch, S. Broyles, M. A. Alam and R. Bashir. Anomalous resonance in a nanomechanical biosensor. *Proceedings of the National Academy of Sciences of the United States of America*, 103(36): 13362-13367, 2006.

[Haug93] M. Haug, K. D. Schierbaum, G. Gauglitz and W. Göpel. Chemical sensors based upon polysiloxanes: comparison between optical, quartz microbalance, calorimetric, and capacitance sensors. *Sensors and Actuators B: Chemical*. 11(1-3): 383-391, 1993.

[Haynes10] W. M. Haynes. *CRC Handbook of Chemistry & Physics,* CRC Press. 91st edition, 2010. ISBN 978-1439820773.

[Helm05] M. Helm, J. J. Servant, F. Saurenbach, and R. Berger. Read-out of micromechanical cantilever sensors by phase shifting interferometry. *Applied Physics Letters*, 87(6):064101-01 - 064101-1 -03, 2005.

[Hennemeyer08] M. Hennemeyer, S. Burghardt and R. W. Stark. Cantilever Micro-rheometer for the Characterisation of Sugar Solutions. *Sensors*, 8(1): 10-22, 2008.

[Hoogenboom05] B. W. Hoogenboom, P. L. T. M. Frederix' J. L. Yang, S. Martin, Y. Pellmont, M. Steinacher, S. Zäch, E. Langenbach, H-J. Heimbeck, A. Engel and H. J. Hug. A Fabry–Perot interferometer for micrometer-sized cantilevers, *Applied Physics Letters*, 86(7): 074101-1 - 074101-3, 2005.

[Ilic01] B. Ilic, D. Czaplewski, M. Zalalutdinov, H. G. Craighead, P. Neuzil, C. Campagnolo, and C. Batt. Single cell detection with micromechanical oscillators. *Journal of vacuum science & technology. B, Microelectronics and nanometer structures processing, measurement and phenomena*, 19(6): 2825-2828, 2001.

[Ilic04] B. Ilic, Y. Yang and C. Craighead. Virus detection using nanoelectromechanical devices. *Applied Physics Letters*, 85(13): 2604-2606, 2004.

[Ilic05] B. Ilic,Y. Yang, K. Aubin, R. Reichenbach, S. Krylov and H. G. Craighead. Enumeration of DNA Molecules Bound to a Nanomechanical Oscillator. *Nano Letters*, 5(5): 925–929, 2005.

[Itoh94] T. Itoh and T. Suga. Force sensing microcantilever using sputtered zinc oxide thin film. *Applied Physics Letters*, 64(1): 37-39, 1994.

[Iwasaki79] K. Iwasaki and T. Fujiyama. Light-scattering study of clathrate hydrate formation in binary mixtures of tert-butyl alcohol and water. (2) Temperature effect. *Journal of Physical Chemistry*, 83(4): 463–468, 1979.

[Kawatra10] S. K. Kawatra and A. K. Bakshi. On-Line Viscometry in Particulate Processing. Mineral Processing and Extractive Metallurgy Review. 14(3-4): 249-273, 1995.

[Kelling09] S. Kelling, F. Paoloni, J. Huang, V. P. Ostanin, and S. R. Elliott. Simultaneous readout of multiple microcantilever arrays with phase-shifting interferometric microscopy. *Review of Scientific Instruments*, 80(9): 093101-01 – 093101-08, 2009.

[Khlebarov92] Z. P. Khlebarov, A. I. Stoyanova and D. I. Topalova. Surface acoustic wave gas sensors. *Sensors and Actuators B: Chemical*, (8)1: 33-40, 1992.

[King64] W. H. King. Piezoelectric Sorption Detector. *Analytical Chemistry*, 36(9): 1735-1739, 1964.

[Knowles08] T. P. J. Knowles, W. Shu, F. Huber, H. P. Lang, C. Gerber, C. M. Dobson, and M. E.Welland. Label-free detection of amyloid growth with microcantilever sensors. *Nanotechnology*, 19(38): 384007 1-7, 2008.

[Kupina84] S.A Kupina, A simultaneous quantitation of glycerol, acetic acid and ethanol in grape juice by high performance liquid chromatography. *America Journal of Enology and Viticulture*. 35(2): 59-62, 1984.

[Laibinis91] P. E. Laibinis, M. A. Fox, J. P. Folkers, and G. M. Whitesides. Comparisons of self-assembled monolayers on silver and gold: mixed monolayers derived from HS(CH2)21X and HS(CH2)10Y (X, Y = CH3, CH2OH) have similar properties. *Langmuir*, 7:3167–3173, 1991.

[Lachut07] M. J. Lachut and J. E. Sader. Effect of surface stress on the stiffness of cantilever plates. *Physical Review Letters*, 99(20): 206102-206105, 2007.

[Lagowski75] J. Lagowski, H. C. Gatos and E. S. Sproles. Surface stress and the normal mode of vibration of thin crystals: GaAs. *Applied Physics Letters*, 26(9): 493-495, 1975.

[Lahiri99] J. Lahiri, L. Isaacs, J. Tien and George M. Whitesides. A Strategy for the Generation of Surfaces Presenting Ligands for Studies of Binding Based on an Active Ester as a Common Reactive Intermediate: A Surface Plasmon Resonance Study. *Analytical Chemistry*, 71(4): 777-790, 1999.

[Lang07] H. P. Lang and C. Gerber. *Topics in Current Chemistry*. Springer Berlin, 285, 1-27, 2008. ISBN 978-3-540-78394-7.

[Langmuir18] I. Langmuir. The adsorption of gases on plane surfaces of glass, mica and platinum. *Journal of the American Chemical Society*, 40(9):1361–1403, 1918.

[Larvik03] N. V. Lavrik and P. G. Datskos. Femtogram mass detection using photothermally actuated nanomechanical resonators**.** *Applied Physics Letters*, 82(16): 2697-2699, 2003.

[Lavrik04] N. V. Lavrik, M. J. Sepaniak and P. G. Datskos. Cantilever transducers as a platform for chemical and biological sensors. *Review of Scientific Instruments*, 75(7): 2229-2253, 2004.

[Li07] M. Li, H. X. Tang and M. L. Roukes. Ultra-sensitive NEMS-based cantilevers for sensing, scanned probe and very high-frequency applications. *Nature Nanotechnology*, 2(2): 114-120, 2007.

[Lindholm65] U. S. Lindholm, D. D. Kana, W-H, Chu and H. N Abramson. Elastic vibration characteristics of cantilever plates in water. *Journal of Ship Research,* 9: 11-22.

[Love05] J. C. Love, L. A. Estroff, J. K. Kriebel, R. G. Nuzzo, and G. M. Whitesides. Self-Assembled Monolayers of Thiolates on Metals as a Form of Nanotechnology. *Chemical Reviews*, 105:1103–1170, 2005.

[Maksymovych10] P. Maksymovych, O. Voznyy, D. B. Dougherty, D. C. Sorescu, and J. T. Yates Jr. Gold adatom as a key structural component in self-assembled monolayers of organosulfur molecules on Au (111). *Progress in Surface Science*, 85(5-8):206–240, 2010.

[Marx03] K. A. Marx. Quartz Crystal Microbalance:□ A Useful Tool for Studying Thin Polymer Films and Complex Biomolecular Systems at the Solution−Surface Interface. *Biomacromolecules*, 5(4): 1099-1120, 2003.

[Mattick70] L. R. Mattick and A. C. Rice. Quantitative Determination of Lactic Acid and Glycerol in Wines by Gas Chromatography. *American Journal of Enology and Viticulture*, 21(4): 205-212, 1970.

[Mattos98] I. L. Mattos, R. P. Sartini, Elias A. G. Zagatto, B. F. Reis and M. F. Gine. Spectrophotometric Flow Injection Determination of Ethanol in Distilled Spirits and Wines Involving Permeation through a Silicon Tubular Membrane. *Analytical Sciences*, 14(5): 1005-1008, 1998.

[McCallum89] J. J. McCallum. Piezoelectric devices for mass and chemical measurements: an update. *Analyst*, 114(10): 1173-1189, 1989.

[McFarland05]	A. W. McFarland, M. A. Poggi, M. J. Doyle, L. A. Bottomley and J. S. Colton. Influence of surface stress on the resonance behaviour of microcantilevers. *Applied Physics Letters*, 87(5): 053505-01 - 053505-1-03, 2005.
[McKendry02]	R. McKendry, J. Zhang, Y. Arntz, T. Strunz, M. Hegner, H-P. Lang, M. K. Baller, U. Certa, E. Meyer, H-J. Güntherodt and C. Gerber. Multiple label-free biodetection and quantitative DNA-binding assays on a nanomechanical cantilever array. *Proceedings of the National Academy of Sciences of the United States of America*, 99(15): 9783-9788, 2002.
[Mertens08]	J. Mertens, C. Rogero, M. Calleja, D. Ramos, J. A. Martín-Gago, C. Briones and J. Tamayo. Label-free detection of DNA hybridisation based on hydration-induced tension in nucleic acid films. *Nature Nanotechnology*, 3(5): 301-307, 2008.
[Meyer88]	G. Meyer and N. M. Amer. Novel optical approach to atomic force microscopy. *Applied Physics Letters*, 53(12):1045-1047, 1988.
[Mukhopadhyay05]	R. Mukhopadhyay, V. V. Sumbayev, M. Lorentzen, J. Kjems, P. A. Andreasen and F. Besenbacher. Cantilever sensor for nanomechanical detection of specific protein conformations. *Nano Letters*, 5(12): 2385-2388, 2005.
[Muratsugu93]	M. Muratsugu , F. Ohta , Y. Miya , T. Hosokawa , S. Kurosawa, N. Kamo and H. Ikeda. Quartz crystal microbalance for the detection of microgram quantities of human serum albumin: relationship between the frequency change and the mass of protein adsorbed. *Analytical Chemistry*, 65(20): 2933-2937, 1993.
[Nagle98]	H. T. Nagle, R. Gutierrez-Osuna and S. S. Schiffman. The how and why electronic noses. *IEEE Spectrum*, 35(9): 22-31, 1998.

[Naviglio01]	D. Naviglio, R. Romano and G. Attanasio, Rapid determination of ethanol content in spirits and in beer by high resolution gas chromatography. Italian Food and Beverage Technology, 24: 19-21, 2001.
[Ndieyira08]	J. W. Ndieyira, M. Watari, A. D. Barrera, D. Zhou, M. Vögtli, M. Batchelor, M. A. Cooper, T. Strunz, M. A. Horton, C. Abell, T. Rayment, G. Aeppli and R. A. McKendry. Nanomechanical detection of antibiotic–mucopeptide binding in a model for superbug drug resistance. *Nature Nanotechnology*, 3(11): 691 – 696, 2008.
[Nieto71]	M. Nieto and H. R. Perkins. Modifications of the acyl-D-alanyl-D-alanine terminus affecting complex-formation with vancomycin. *Biochemical Journal*, 123:789–803, 1971.
[Nordstrom08]	M. Nordstrom, S. Keller, M. Lillemose, A. Johansson, S. Dohn, D. Haefliger, G. Blagoi, M. Havsteen-Jakobsen and A. Boisen. SU-8 cantilevers for bio/chemical sensing; Fabrication, characterisation and development of novel read-out methods. *Sensors,* 8(3): 1595-1612, 2008.
[Norton43]	F. J. Norton, *US Patent No. 2-307-800*, 1943.
[Nuzzo83]	R. G. Nuzzo and D. L. Allara. Adsorption of bifunctional organic disulfides on gold surfaces. Journal of the American Chemical Society, 105: 4481–4483, 1983.
[Nuzzo87]	R. G. Nuzzo, B. R. Zegarski, and L. H. Dubois. Fundamental studies of the chemisorption of organosulfur compounds on gold (111). Implications for molecular self-assembly on gold surfaces. Journal of the American Chemical Society, 109:733–740, 1987.
[Oden96]	P. I. Oden, G. Y. Chen, R. A. Steele, R. J. Warmack, and T. Thundat, Viscous drag measurements utilizing microfabricated cantilevers. *Applied Physics Letters*, 68(26): 3814-3816, 1996.

[Oden98] P.I. Oden. Gravimetric sensing of metallic deposits using an end-loaded microfabricated beam structure. *Sensors and Actuators B: Chemical*, 53(3): 191-196, 1998.

[Oliveira06] M. H. Oliveira, M. A. Segundo, J. Lima, V. Grassi and E, Zagatto. Kinetic Enzymatic Determination of Glycerol in Wine and Beer Using a Sequential Injection System with Spectrophotometric Detection. *Journal of Agricultural and Food Chemistry*, 54(12): 4136-4140, 2006.

[O'Sullivan98] C. K. O'Sullivan and G. G. Guilbault. Commercial quartz crystal microbalances – theory and applications. *Biosensors and Bioelectronics*, 14(8-9): 663-670, 1998.

[Pálinkás91] G. Pálinkás, E. Hawlicka and K. Heinzinger. Molecular dynamics simulations of water-methanol mixtures. *Chemical Physics*, 158(1): 65-76, 1991.

[Patel98] N. Patel, M.C. Davies, R.J. Heaton, C.J. Roberts, S.J.B. Tendler and P.M. Williams. A scanning probe microscopy study of the physisorption and chemisorption of protein molecules onto carboxylate terminated self-assembled monolayers. *Applied Physics A: Materials Science & Processing*, 66(1): 569-574, 1998.

[Paxman12] R. Paxman, J. Stinson, A. Dejardin, R. A. McKendry and B. W. Hoogenboom. Using Micromechanical Resonators to Measure Rheological Properties and Alcohol Content of Model Solutions and Commercial Beverages. *Sensors*, 12(5): 6497-6507, 2012.

[Pearce03] T. C. Pearce, S. S. Schiffman, H. T. Nagle and J. W. Gardner. *Handbook of Machine Olfaction: Electronic Nose Technology*, Wiley-VCH, 2002. ISBN: 978-3-527-60563-7

[Pohl00] A. Pohl, A review of wireless SAW sensors. *IEEE transactions on ultrasonics, ferroelectrics, and frequency control*, 47(2): 317-322, 2000.

[Poirier94] G. E. Poirier , M. J. Tarlov , H. E. Rushmeier, Two-Dimensional Liquid Phase and the px.sqroot.3 Phase of Alkanethiol Self-Assembled Monolayers on Au(111). *Langmuir*, 10 (10): 3383–3386, 1994.

[Poirier97] G. Poirier. Characterisation of Organosulfur Molecular Monolayers on Au(111) using Scanning Tunneling Microscopy. *Chemical Reviews*, 97:1117–1128, 1997.

[Poirier99] G. E. Poirier , T. M. Herne , C. C. Miller and M. J. Tarlov, Molecular-Scale Characterization of the Reaction of Ozone with Decanethiol Monolayers on Au(111). *Journal of the American Chemical Society*, 121 (41): 9703–9711, 1999.

[Porter07] T. L. Porter, T. L. Vail, M. P. Eastman, R. Stewart, J. Reed, R. Venedam, and W. Delinger. A solid-state sensor platform for the detection of hydrogen cyanide gas. *Sensors and Actuators B: Chemical*, 123(1):313–317, 2007.

[Pradhan08] T. Pradhan, P. Ghoshal and R. Biswas. Structural transition in alcohol–water binary mixtures: A spectroscopic study. *Journal of Chemical Sciences*, 120(2): 275–287, 2008.

[Prescesky92] S. Prescesky, M. Parameswaran, A. Rawicz, R. F. B. Turner and U. Reichl. Silicon micromachining technology for sub-nanogram discrete mass resonant biosensors. *Canadian Journal of Physics*, 70(10-11): 1178-1183, 1992.

[Prime93] K. L. Prime and G. M. Whitesides. Adsorption of proteins onto surfaces containing end-attached oligo(ethylene oxide): a model system using self-assembled monolayers. *Journal of the American Chemical Society*, 115(23): 10714–10721, 1993.

[Ramos07] D. Ramos, M. Calleja, J. Mertens, A. Zaballos and J. Tamayo. Measurement of the mass and rigidity of adsorbates on a microcantilever sensor. *Sensors*, 7(9): 1834-1845, 2007.

[Ramos08] D. Ramos, J. Tamayo, J.Mertens, M. Calleja, L.G. Villanueva and A. Zaballos. Detection of bacteria based on the thermomechanical noise of a nanomechanical resonator: origin of the response and detection limits. *Nanotechnology*, 19(3): 035503-01 – 035503-09. 2008.

[Ramos09] D. Ramos, M. Arroyo-Hernández, E. Gil-Santos, H. D. Tong, C. V. Rijn, M. Calleja and J. Tamayo. Arrays of Dual Nanomechanical Resonators for Selective Biological Detection. *Analytical Chemistry*, 81(6): 2274–2279, 2009.

[Raiteri00] R. Raiteri, H-J. Butt and M. Grattarola. Changes in surface stress at the liquid/solid interface measured with a microcantilever. *Electrochimica Acta.* 46(2-3): 157-163.

[Raiteri01] R. Raiteri, M. Grattarola, H-J. Butt and P. Skládal. Micromechanical cantilever-based biosensors. *Sensors and Actuators B: Chemical*, 79(2-3): 115-126, 2001.

[Roukes11] R. B. Karabalin, R. Lifshitz, M. C. Cross, M. H. Matheny, S. C. Masmanidis and M. L. Roukes. Signal Amplification by Sensitive Control of Bifurcation Topology. *Physical Review Letters,* 106: 094102-1 – 094102-4, 2011.

[Sader95] J. E. Sader, I. Larson, P. Mulvaney and L. R. White. Method for the calibration of atomic force microscope cantilevers. *Review of Scientific Instruments*, 66(7): 3789-3798, 1995.

[Sader97] C.A. Vam Eysden and J. E. Sader, Frequency response of cantilever beams immersed in viscous fluids with applications to the atomic force microscope: Arbitrary mode order. *Journal of Applied Physics,* 101(4): 044908-1 - 044908-11, 1997

[Sader98] J. E. Sader, Frequency response of cantilever beams immersed in viscous fluids with applications to the atomic force microscope. *Journal of Applied Physics*, 84(1): 64-76, 1998.

[Sandberg05] R Sandberg, K Mølhave, A Boisen and W Svendsen. Effect of gold coating on the *Q*-factor of a resonant cantilever. *Journal of Micromechanics and Microengineering*, 15(12): 2249–2253, 2005.

[Schaller98] E. Schaller, J. O. Bosset and F. Escher. Electronic noses and their application to food. *Lebensmittel-Wissenschaft und-Technologie*, 31(4): 305-316, 1998.

[Schreiber00] F. Schreiber. *Structure and growth of self-assembling monolayers*. Progress in Surface Science, 65:151–257, 2000.

[Seliger79] R. L. Seliger, J. W. Ward, V. Wang and R. L. Kubena. A high-intensity scanning ion probe with submicrometer spot size. *Applied Physics Letters*, 34(5): 310-312, 1979.

[Sepaniak02] M. Sepaniak, P. Datskos, N. Lavrik and C. Tipple. Microcantilever Transducers: A new Approach in Sensor Technology. *Analytical Chemistry*, 74(21): 568-575, 2002.

[Shu07] W. Shu, E. D. Laue, and A. A. Seshia. Investigation of biotin-streptavidin binding interactions using microcantilever sensors. *Biosensors and Bioelectronics*, 22(9-10):2003–2009, 2007.

[Soper93] A. K. Soper and J. L. Finney. Hydration of methanol in aqueous solution. *Physical Review Letters*, 71(26): 4346–4349, 1993.

[Soper06] A. K. Soper, L. Dougan, J. Crain and J. L. Finney. Excess Entropy in Alcohol−Water Solutions: A Simple Clustering Explanation. *Journal of*

Physical Chemistry - B. 110(8): 3472- 3476, 2006.

BIBLIOGRAPHY

[Steffe96] J. F. Steffe. *Rheological Methods in Food Process Engineering*. Freemen Press. 2nd Edition, 1996. ISBN 096-3203614.

[Stoney09] G. G. Stoney. The Tension of Metallic Films Deposited by Electrolysis. *Proceedings of the Royal Society A: Mathematical, Physical and Engineering Sciences*, 82(553): 172-175, 1909.

[Sushko08] M. L. Sushko, J. H. Harding, A. L. Shluger, R. A. McKendry and M. Watari. Physics of nanomechanical biosensing on cantilever arrays. *Advanced Materials*, 20(20): 3484-3853, 2008.

[Tan07] E. P. S. Tan, Y. Zhu, T. Yu, L. Dai, C. H. Sow, V. B. C. Tan and C. T. Lim. Crystallinity and surface effects on Young's modulus of CuO nanowires. *Applied Physics Letters*, 90(16): 163112-01 – 163112-03, 2007.

[Tamayo05] J. Tamayo. Study of the noise of micromechanical oscillators under quality factor enhancement via driving force control. *Journal of Applied Physics*, 97(4): 044903-01 – 044903-10, 2005.

[Tamayo06] J. Tamayo, D. Ramos, J. Mertens, and M. Calleja. Effect of the adsorbate stiffness on the resonance response of microcantilever sensors. *Applied Physics Letters*, 82(22): 224104-1 – 224104-3, 2006.

[Tatsuma99] T. Tatsuma, Y. Watanabe and N. Oyama. Multichannel quartz crystal microbalance. *Analytical Chemistry*, 71(17): 3632-3636, 1999.

[Thaysen02] J. Thaysen, A. D. Yalçinkaya, P. Vettiger and A. Menon. Polymer-based stress sensor with integrated readout. *Journal of physics. D, Applied physics, 35(21):* 2698 -2703, 2002.

[Thundat94] T. Thundat, R. J. Warmack, C. Y. Chen and D. P. Allison. Thermal and ambient-induced deflections of scanning force microscope cantilevers.

Applied Physics Letters, 64(21): 2894-2896, 1994.

BIBLIOGRAPHY

[Thundat95] T. Thundat, G. Y. Chen, R. J. Warmack, D. P. Allison and E. A. Wachter. Vapor Detection Using Resonating Microcantilevers. *Analytical Chemistry*, 67(3): 519-521, 1995.

[Timoshenko25] S.P. Timoshenko. Analysis of bi-methal thermostats. *Journal of the Optical Society of America*, 11(3): 233-255, 1925.

[Timoshenko53] S. P. Timoshenko. *History of strength of materials*. McGraw-Hill, 1953. ISBN 978-0486611877.

[Truesdell60] C. Truesdell. *The rational mechanics of flexible or elastic bodies*: *1638-1788*, Springer, 1960. ISBN 978-3-7643-1441-5.

[Ulman96] A. Ulman. Formation and structure of self-assembled monolayers. *Chemical Reviews*, 96:1533–1554, 1996.

[Vančura07] C. Vančura, I. Dufour, S. M. Heinrich, F. Josse and A. Hierlemann. Analysis of resonating microcantilevers operating in a viscous liquid environment. *Sensors and Actuators A: Physical*, 141(1): 43-51, 2007.

[Vettiger 00] P.Vettiger, M. Despont, U. Dreschsler, U. Durig, W. Haberle, M.I. Lutwyche, H. E. Rothuizen, R. Stutz, R. Widmer and G. K. Binnig. The ‘Millipede’—More than thousand tips for future AFM storage. *IBM Journal of Research and Development*, 44(3): 323-340, 2000.

[Waggoner07] P. S. Waggoner and H. G. Craighead. Micro- and nanomechanical sensors for environmental, chemical, and biological detection. *Lab on a Chip*, 7(10): 1238-1255, 2007.

[Wagner92] K. Wagner, U. Bilitewski and R. D. Schmid. Flow injection analysis of wine—Accomplishments and needs *Microchemical Journal*, 45(2): 114-120, 1992

[Wang03] M. L. Wang, Y. M. Choong, N. W. Su and M. H. Lee. A rapid method for determination of ethanol in alcoholic beverages using capillary gas chromatography. *Journal of Food and Drug Analysis*, 11(2): 133-140, 2003.

[Wanunu04] M. Wanunu, A. Vaskevich, and I. Rubinstein. Widely-Applicable Gold Substrate for the Study of Ultrathin Overlayers. *Journal of the American Chemical Society*, 126:5569–5576, 2004.

[Watari07] M. Watari, J. Galbraith, H-P. Lang, M. Sousa, M. Hegner, C. Gerber, M. A. Horton, and R. A. McKendry. Investigating the molecular mechanisms of in plane mechanochemistry on cantilever arrays. *Journal of the Americal Chemical Society*, 129(3):601–609, 2007.

[Watari08] M. Watari, J. Galbraith, H-P. Lang, M. Sousa, M. Hegner, C. Gerber, M. A.Horton and R. A. McKendry. Investigating the Molecular Mechanisms of In-Plane Mechanochemistry on Cantilever Arrays. *Journal of the American Chemical Society*, 129(3): 601–609. 2008.

[Wegener01] J. Wegener, A. Janshoff and C. Steinem. The quartz crystal microbalance as a novel means to study cell-substrate interactions in situ. *Cell Biochemistry and Biophysics*, 34(1): 121-151, 2001.

[Wehrmeister07] J. Wehrmeister, A. Fuss, F. Saurenbach, R. Berger and M. Helm. Readout of micromechanical cantilever sensor arrays by Fabry-Perot interferometry. *Review of Scientific Instruments*, 78(10): 104105–104109, 2007.

[Whitesides91] G. Whitesides, J. Mathias, and C. Seto. Molecular self-assembly and nanochemistry: a chemical strategy for the synthesis of nanostructures. *Science*, 254(5036):1312–1319, 1991.

[Whitesides02] G. M. Whitesides and B. Grzybowski. Self-assembly at all scales. *Science*, 295(5564):2418–21, 2002.

BIBLIOGRAPHY

[Wilfinger68] R. J. Wilfinger, P. H. Bardell and D. S. Chhabra, The Resonistor: A Frequency Selective Device Utilizing the Mechanical Resonance of a Silicon Substrate. *IBM Journal of Research and Development*, 12(1): 113-118, 1968.

[Yang02] J. Yang, T. Ono, and M. Esashi. Energy dissipation in submicrometer thick single-crystal silicon cantilevers, *Journal of Microelectromechanical Systems*, 11(6): 775 – 783. 2002.

[Yang03] G. Yang and G. Liu. New Insights for Self-Assembled Monolayers of Organothiols on Au(111) Revealed by Scanning Tunneling Microscopy. *Journal of Physical Chemistry B*, 107:8746–8759, 2003.

[Yang05] D. H. Yang, A. H. Bae, K. Koumoto, S-W. Lee, K. Sakurai, S. Shinkai. In situ monitoring of polysaccharide–polynucleotide interaction using a schizophyllan-immobilized QCM device. *Sensors and Actuators B: Chemical*, 105(2): 490-494.

[Yang06] Y. T. Yang, C. Callegari, X. L. Feng, K. L. Ekinci, and M. L. Roukes, Zeptogram-Scale Nanomechanical Mass Sensing, *Nano Letters*, 6(4): 583-586, 2006.

[Youssry10] M. Youssry, N. Belmiloud, B. Caillard, C. Ayela, C. Pellet and I. Dufour. A straightforward determination of fluid viscosity and density using microcantilevers: Analytical and experimental studies. *Procedia Engineering*, 5: 1035-1035, 2010.

APPENDIX A: Resonance frequency and quality factor data for metal coatings in AIR

Gold

Mode 1			**Frequency**			**Q**	
t_a [nm]	m_a/m_c	$f_0^{(n)}$ [kHz]	$f_{res}^{(n)}$ [kHz]	$\Delta f/f_o$	Q_0	Q	$\Delta Q/Q_o$
50	0.44	4.821	4.237	-0.1211	17.22	22.08	0.2822
50	0.44	4.812	4.232	-0.1205	16.9	22.12	0.3089
50	0.44	4.814	4.233	-0.1207	16.57	21.94	0.3241
50	0.44	4.913	4.331	-0.1185	16.5	22.65	0.3727
50	0.44	4.907	4.319	-0.1198	16.05	22.89	0.4262
100	0.88	4.829	3.907	-0.1909	18.05	27.67	0.5330
100	0.88	4.823	3.907	-0.1899	17.11	26.54	0.5511
100	0.88	4.822	3.901	-0.1910	17.08	27.70	0.6218
150	1.32	4.901	3.791	-0.2265	16.11	33.21	1.0615
150	1.32	4.896	3.781	-0.2277	16.06	33.18	1.0660

Gold

Mode 2			**Frequency**			**Q**	
t_a [nm]	m_a/m_c	$f_0^{(n)}$ [kHz]	$f_{res}^{(n)}$ [kHz]	$\Delta f/f_o$	Q_0	Q	$\Delta Q/Q_o$
50	0.44	30.56	26.75	-0.125	50.9	67.55	0.327
50	0.44	30.53	26.72	-0.125	51.26	67.31	0.313
50	0.44	30.53	26.72	-0.125	50.74	68.6	0.352
50	0.44	31.16	27.29	-0.124	52.38	70.36	0.343
50	0.44	31.12	27.26	-0.124	52.45	70.48	0.344
100	0.88	30.6	24.62	-0.195	51.5	83.8	0.627
100	0.88	30.6	24.59	-0.196	50.77	85.19	0.678
100	0.88	30.58	24.57	-0.197	50.04	84.21	0.683
150	1.32	31.08	23.8	-0.234	51.86	101.8	0.963
150	1.32	31.05	23.75	-0.235	51.48	102.2	0.985

APPENDIX A

Copper

Mode 1		**Frequency**			**Q**		
t_a [nm]	m_a/m_c	$f_0^{(n)}$ [kHz]	$f_{res}^{(n)}$ [kHz]	$\Delta f/f_o$	Q_0	Q	$\Delta Q/Q_o$
60	0.25	4.786	4.611	-0.0366	16.27	20.08	0.2342
60	0.25	4.791	4.619	-0.0359	16.38	19.69	0.2021
60	0.25	4.792	4.619	-0.0361	16.41	19.76	0.2041
60	0.25	4.798	4.628	-0.0354	16.68	19.83	0.1888
60	0.25	4.808	4.636	-0.0358	16.4	19.79	0.2067
60	0.25	4.814	4.639	-0.0364	16.69	19.91	0.1929

Copper

Mode 2		**Frequency**			**Q**		
t_a [nm]	m_a/m_c	$f_0^{(n)}$ [kHz]	$f_{res}^{(n)}$ [kHz]	$\Delta f/f_o$	Q_0	Q	$\Delta Q/Q_o$
60	0.25	30.37	29.17	-0.040	50.94	60.18	0.181
60	0.25	30.40	29.21	-0.039	50.68	60.24	0.189
60	0.25	30.41	29.22	-0.039	51.13	60.99	0.193
60	0.25	30.43	29.26	-0.038	51.69	60.11	0.163
60	0.25	30.47	29.29	-0.039	50.88	60.40	0.187
60	0.25	30.52	29.32	-0.039	51.39	60.38	0.175

APPENDIX B: Resonance frequency and quality factor data for metal coatings in LIQUID

Gold									
Mode 2	**Frequency**			**Q**					
	$f_0^{(n)}$ [kHz]	**$f_{res}^{(n)}$ [kHz]**	**$\Delta f/f_o$**	**Q_0**	**Q**	**$\Delta Q/Q_o$**	**$\Delta m/m_0$**	**$\Delta D/D_0$**	**$f_{vac}^{(n)}$ [kHz]**
	±0.14643	±0.11477	±0.01026	±0.08204	±0.08534	±0.0032	±0.00709	±0.01991	
Au 20nm	**4.940**	**5.128**	**0.0384**	**3.166**	**3.228**	**0.020**	**0.193**	**0.080**	**30**
Measurement 1	*4.980*	*5.203*	*0.0448*	*3.085*	*3.154*	*0.022*	*0.198*	*0.092*	*30*
Measurement 2	*5.121*	*5.240*	*0.0232*	*3.145*	*3.191*	*0.015*	*0.198*	*0.050*	*30*
Measurement 3	*4.879*	*5.080*	*0.0412*	*3.152*	*3.217*	*0.021*	*0.192*	*0.085*	*30*
Measurement 4	*4.778*	*4.990*	*0.0444*	*3.280*	*3.350*	*0.021*	*0.183*	*0.091*	*30*
	±0.00208	±0.03786	±0.00794	±0.001	±0.00643	±0.00153	±0.02721	±0.01514	
Au 50nm	**4.939**	**5.433**	**0.100**	**3.150**	**3.307**	**0.050**	**0.458**	**0.213**	**30**
Measurement 1	*4.941*	*5.390*	*0.091*	*3.149*	*3.300*	*0.048*	*0.506*	*0.195*	*30*
Measurement 2	*4.940*	*5.450*	*0.103*	*3.151*	*3.310*	*0.050*	*0.435*	*0.219*	*30*
Measurement 3	*4.937*	*5.460*	*0.106*	*3.150*	*3.312*	*0.051*	*0.435*	*0.224*	*30*
	±0.005	±0.01528	±0.00208	±0.00058	±0.00577	±0.00173	±0.08653	±0.00206	
Au 100nm	**4.950**	**5.833**	**0.178**	**3.146**	**3.423**	**0.088**	**0.796**	**0.395**	**30**
Measurement 1	*4.950*	*5.830*	*0.178*	*3.146*	*3.420*	*0.087*	*0.772*	*0.392*	*30*
Measurement 2	*4.955*	*5.850*	*0.181*	*3.147*	*3.420*	*0.087*	*0.724*	*0.397*	*30*
Measurement 3	*4.945*	*5.820*	*0.177*	*3.146*	*3.430*	*0.090*	*0.892*	*0.395*	*30*
	±0.00451	±0.14902	±0.03073	±0.00404	±0.00451	±0.01159	±0.09958	±0.13259	
Au 150nm	**4.950**	**6.156**	**0.244**	**3.140**	**3.583**	**0.141**	**1.757**	**0.553**	**30**
Measurement 1	*4.954*	*6.000*	*0.211*	*3.135*	*3.540*	*0.129*	*1.643*	*0.404*	*30*
Measurement 2	*4.945*	*6.170*	*0.248*	*3.142*	*3.590*	*0.143*	*1.801*	*0.597*	*30*
Measurement 3	*4.950*	*6.297*	*0.272*	*3.142*	*3.620*	*0.152*	*1.827*	*0.658*	*30*

Gold

Mode 3	**Frequency**			**Quality Factor**					
	$f_0^{(n)}$ **[kHz]**	$f_{res}^{(n)}$ **[kHz]**	$\Delta f/f_o$	Q_0	**Q**	$\Delta Q/Q_o$	$\Delta m/m_0$	$\Delta D/D_0$	$f_{vac}^{(n)}$ **[kHz]**
	±0.17292	±0.18348	±0.00428	±0.10197	±0.10258	±0.00173	±0.00954	±0.00854	
Au 20nm	**15.253**	**15.905**	**0.043**	**6.090**	**6.233**	**0.023**	**0.192**	**0.091**	**82**
Measurement 1	*15.210*	*15.860*	*0.0427*	*6.075*	*6.217*	*0.023*	*0.190*	*0.091*	*82*
Measurement 2	*15.240*	*15.890*	*0.0427*	*6.076*	*6.215*	*0.023*	*0.176*	*0.090*	*82*
Measurement 3	*15.310*	*15.965*	*0.0428*	*6.120*	*6.268*	*0.024*	*0.210*	*0.092*	*82*
	±0.01528	±0.15948	±0.01155	±0.02309	±0.00608	±0.0048	±0.02631	±0.02485	
Au 50nm	**15.203**	**17.133**	**0.127**	**5.967**	**6.358**	**0.070**	**0.472**	**0.280**	**82**
Measurement 1	*15.200*	*17.11*	*0.126*	*5.980*	*6.37*	*0.0686*	*0.473*	*0.277*	*82*
Measurement 2	*15.220*	*16.95*	*0.114*	*5.980*	*6.34*	*0.0632*	*0.458*	*0.250*	*82*
Measurement 3	*15.190*	*17.34*	*0.142*	*5.940*	*6.365*	*0.0745*	*0.484*	*0.312*	*82*
	±0.02082	±0.09074	±0.00721	±0.007	±0.02517	±0.00317	±0.04891	±0.01582	
Au 100nm	**15.213**	**17.913**	**0.177**	**5.973**	**6.573**	**0.101**	**0.743**	**0.437**	**82**
Measurement 1	*15.230*	*18.07*	*0.186*	*5.970*	*6.58*	*0.1022*	*0.756*	*0.432*	*82*
Measurement 2	*15.190*	*17.62*	*0.160*	*5.981*	*6.59*	*0.1018*	*0.735*	*0.453*	*82*
Measurement 3	*15.220*	*18.05*	*0.186*	*5.968*	*6.55*	*0.0975*	*0.738*	*0.425*	*82*
	±0.03464	±0.04583	±0.00096	±0.01419	±0.02	±0.00267	±0.05962	±0.00153	
Au 150nm	**15.220**	**18.070**	**0.187**	**5.961**	**6.920**	**0.161**	**1.712**	**0.510**	**82**
Measurement 1	*15.240*	*18.11*	*0.1883*	*5.958*	*6.90*	*0.1581*	*1.646*	*0.509*	*82*
Measurement 2	*15.180*	*18.02*	*0.1871*	*5.976*	*6.94*	*0.1613*	*1.730*	*0.510*	*82*
Measurement 3	*15.240*	*18.08*	*0.1864*	*5.948*	*6.92*	*0.1634*	*1.761*	*0.512*	*82*

APPENDIX B

Titanium

	Frequency			**Q**					
Mode 2	$f_0^{(n)}$ **[kHz]**	$f_{res}^{(n)}$ **[kHz]**	$\Delta f/f_o$	Q_0	**Q**	$\Delta Q/Q_o$	$\Delta m/m_0$	$\Delta D/D_0$	$f_{vac}^{(n)}$ **[kHz]**
	±0.005	±0.12859	±0.02702	±0.00473	±0.02201	±0.00853	±0.00755	±0.03595	
Ti 20 nm	**4.950**	**5.244**	**0.0595**	**3.140**	**3.242**	**0.0327**	**0.048**	**0.159**	**30**
Measurement 1	*4.950*	*5.25*	*0.0606*	*3.145*	*3.22*	*0.0238*	*0.041*	*0.119*	*30*
Measurement 2	*4.945*	*5.37*	*0.0859*	*3.138*	*3.243*	*0.0335*	*0.056*	*0.171*	*30*
Measurement 3	*4.955*	*5.113*	*0.0319*	*3.136*	*3.264*	*0.0408*	*0.047*	*0.188*	*30*
Mode 3	±0.01	±0.13317	±0.00807	±0.01	±0.00808	±0.00304	±0.00058	±0.0165	
Ti 20 nm	**15.220**	**16.590**	**0.8850**	**5.910**	**6.125**	**0.0363**	**0.044**	**0.183**	**82**
Measurement 1	*15.210*	*16.470*	*0.0828*	*5.920*	*6.120*	*0.0338*	*0.049*	*0.168*	*82*
Measurement 2	*15.230*	*16.740*	*0.0991*	*5.900*	*6.134*	*0.0397*	*0.041*	*0.202*	*82*
Measurement 3	*15.220*	*16.560*	*0.0880*	*5.910*	*6.120*	*0.0355*	*0.043*	*0.178*	*82*

Copper

	Frequency			**Q**					
Mode 2	$f_0^{(n)}$ **[kHz]**	$f_{res}^{(n)}$ **[kHz]**	$\Delta f/f_o$	Q_0	**Q**	$\Delta Q/Q_o$	$\Delta m/m_0$	$\Delta D/D_0$	$f_{vac}^{(n)}$ **[kHz]**
	±0.00416	±0.04041	±0.00785	±0.00321	±0.01	±0.00317	±0.01127	±0.01752	
Cu 60 nm	**4.945**	**5.573**	**0.1270**	**3.138**	**3.310**	**0.0547**	**0.242**	**0.262**	**30**
Measurement 1	4.950	5.580	*0.1273*	3.142	3.310	*0.0535*	0.236	0.263	*30*
Measurement 2	4.944	5.610	*0.1347*	3.137	3.320	*0.0583*	0.255	0.279	*30*
Measurement 3	4.942	5.530	*0.1190*	3.136	3.300	*0.0523*	0.235	0.244	*30*
Mode 3	±0.01	±0.04	±0.00307	±0.00153	±0.01528	±0.00236	±0.02403	±0.00819	
Cu 60 nm	**15.230**	**16.773**	**0.1002**	**5.911**	**6.223**	**0.0527**	**0.273**	**0.216**	**82**
Measurement 1	15.220	16.800	*0.1003*	5.913	6.273	*0.0609*	0.262	0.221	*82*
Measurement 2	15.240	16.710	*0.0965*	5.910	6.190	*0.0474*	0.283	0.206	*82*
Measurement 3	15.230	16.810	*0.1037*	5.911	6.205	*0.0497*	0.273	0.221	*82*

APPENDIX C – Resonance and quality factor data for self-assembled monolayers in LIQUID

n=3 as reference

	Frequency			**Quality Factor**					
Mode 2	$f_0^{(n)}$ **[kHz]**	$f_{res}^{(n)}$ **[kHz]**	$\Delta f/f_o$	Q_0	**Q**	$\Delta Q/Q_o$	$\Delta m/m_0$	$\Delta D/D_0$	$f_{vac}^{(n)}$ **[kHz]**
		±0.00238	±0.00048		±0.00238	±0.00055	±0.001249	±0.00124	
$C3CH_3$	**5.313**	**5.313**	**0.000**	**3.363**	**3.363**	**0.000**	**0.001**	**0.000**	**30**
Measurement 1	*5.313*	*5.314*	*0.0002*	*3.363*	*3.364*	*0.0003*	*0.0072*	*0.0007*	*30*
Measurement 2	*5.313*	*5.311*	*-0.0004*	*3.363*	*3.361*	*-0.0006*	*-0.0144*	*-0.0012*	*30*
Measurement 3	*5.313*	*5.310*	*-0.0006*	*3.363*	*3.362*	*-0.0003*	*-0.0026*	*-0.0012*	*30*
Measurement 4	*5.313*	*5.315*	*0.0004*	*3.363*	*3.365*	*0.0006*	*0.0144*	*0.0012*	*30*
		±0.0359	±0.00675		±0.00959	±0.00285	±0.00126	±0.01108	
$C8CH_3$	**5.313**	**4.5093**	**-0.1513**	**3.363**	**3.1600**	**-0.0604**	**0.0029**	**-0.2665**	**30**
Measurement 1	*5.313*	*4.5580*	*-0.1421*	*3.363*	*3.1730*	*-0.056497*	*0.0037*	*-0.2514*	*30*
Measurement 2	*5.313*	*4.5130*	*-0.1506*	*3.363*	*3.1610*	*-0.060065*	*0.0028*	*-0.2653*	*30*
Measurement 3	*5.313*	*4.4900*	*-0.1549*	*3.363*	*3.1550*	*-0.06185*	*0.0040*	*-0.2724*	*30*
Measurement 4	*5.313*	*4.4760*	*-0.1575*	*3.363*	*3.1510*	*-0.063039*	*0.0012*	*-0.2767*	*30*
		±0.02329	±0.00441		±0.00591	±0.00176	±0.00087	±0.00403	
$C11CH_3$	**5.313**	**4.8265**	**-0.0916**	**3.363**	**3.2428**	**-0.0358**	**0.0045**	**-0.1660**	**30**
Measurement 1	*5.313*	*4.8120*	*-0.0943*	*3.363*	*3.2390*	*-0.036872*	*0.0040*	*-0.1707*	*30*
Measurement 2	*5.313*	*4.8390*	*-0.0892*	*3.363*	*3.2460*	*-0.03479*	*0.0051*	*-0.1619*	*30*
Measurement 3	*5.313*	*4.8280*	*-0.0913*	*3.363*	*3.2430*	*-0.035682*	*0.0032*	*-0.1655*	*30*
Measurement 4	*5.313*	*4.8270*	*-0.0915*	*3.363*	*3.2430*	*-0.035682*	*0.0057*	*-0.1658*	*30*
		±0.0068	±0.00128		±0.00158	±0.00047	±0.00115	±0.00265	
$C16CH_3$	**5.313**	**5.1136**	**-0.0375**	**3.363**	**3.3150**	**-0.0143**	**0.0064**	**-0.0686**	**30**
Measurement 1	*5.313*	*5.1140*	*-0.0375*	*3.363*	*3.3150*	*-0.014273*	*0.0054*	*-0.0695*	*30*
Measurement 2	*5.313*	*5.1180*	*-0.0367*	*3.363*	*3.3160*	*-0.013976*	*0.0056*	*-0.0682*	*30*
Measurement 3	*5.313*	*5.1220*	*-0.0359*	*3.363*	*3.3170*	*-0.013678*	*0.0057*	*-0.0668*	*30*
Measurement 4	*5.313*	*5.1090*	*-0.0384*	*3.363*	*3.3140*	*-0.01457*	*0.0077*	*-0.0658*	*30*
Measurement 5	*5.313*	*5.1050*	*-0.0391*	*3.363*	*3.3130*	*-0.014868*	*0.0076*	*-0.0726*	*30*

APPENDIX C

n=3 as reference									
	Frequency			**Quality Factor**					
Mode 3	$f_0^{(n)}$ **[kHz]**	$f_{res}^{(n)}$ **[kHz]**	**$\Delta f/f_o$**	**Q_0**	**Q**	**$\Delta Q/Q_o$**	**$\Delta m/m_0$**	**$\Delta D/D_0$**	$f_{vac}^{(n)}$ **[kHz]**
		±0.0.0223	±0.00138		±0.0278	±0.00404	±0.00133	±0.006	
$C3CH_3$	**16.200**	**16.200**	**0.00**	**6.8713**	**6.8713**	**0.00**	**0.000**	**0.000**	**82**
Measurement 1	*16.200*	*16.200*	0.0000	*6.8713*	*6.8900*	*0.0027*	*0.0697*	*0.0027*	*82*
Measurement 2	*16.200*	*16.235*	0.0021	*6.8713*	*6.9000*	*0.0042*	*0.0850*	*0.0075*	*82*
Measurement 3	*16.200*	*16.186*	-0.0009	*6.8713*	*6.8500*	*-0.0031*	*-0.0707*	*-0.0044*	*82*
Measurement 4	*16.200*	*16.180*	-0.0012	*6.8713*	*6.8450*	*-0.0038*	*-0.0831*	*-0.0056*	*82*
		±0.02059	±0.00127		±0.00411	±0.00055	±0.00159	±0.00207	
$C8CH_3$	**16.200**	**13.546**	**-0.1639**	**6.8713**	**6.4023**	**-0.0683**	**0.0024**	**-0.2915**	**82**
Measurement 1	*16.200*	*13.542*	*-0.1641*	*6.8713*	*6.4010*	*-0.068437*	*0.0003*	*-0.2919*	*82*
Measurement 2	*16.200*	*13.574*	*-0.1621*	*6.8713*	*6.4070*	*-0.067564*	*0.0003*	*-0.2887*	*82*
Measurement 3	*16.200*	*13.547*	*-0.1638*	*6.8713*	*6.4030*	*-0.068146*	*0.0045*	*-0.2913*	*82*
Measurement 4	*16.200*	*13.520*	*-0.1654*	*6.8713*	*6.3980*	*-0.068874*	*0.0047*	*-0.2940*	*82*
		±0.07736	±0.00479		±0.01425	±0.00201	±0.00125	±0.00834	
$C11CH_3$	**16.200**	**14.567**	**-0.1008**	**6.8713**	**6.5893**	**-0.0410**	**0.0047**	**-0.1850**	**82**
Measurement 1	*16.200*	*14.5310*	*-0.1030*	*6.8713*	*6.5830*	*-0.04195*	*0.0052*	*-0.1889*	*82*
Measurement 2	*16.200*	*14.5910*	*-0.0993*	*6.8713*	*6.5940*	*-0.040349*	*0.0063*	*-0.1824*	*82*
Measurement 3	*16.200*	*14.6620*	*-0.0950*	*6.8713*	*6.6060*	*-0.038603*	*0.0037*	*-0.1748*	*82*
Measurement 4	*16.200*	*14.4830*	*-0.1060*	*6.8713*	*6.5740*	*-0.04326*	*0.0037*	*-0.1941*	*82*
		±0.07053	±0.0043		±0.01332	±0.00171	±0.00082	±0.00811	
$C16CH_3$	**16.200**	**15.839**	**-0.0223**	**6.8713**	**6.8122**	**-0.0086**	**0.0079**	**-0.0422**	**82**
Measurement 1	*16.200*	*15.7790*	*-0.0260*	*6.8713*	*6.8020*	*-0.010078*	*0.0079*	*-0.0492*	*82*
Measurement 2	*16.200*	*15.7850*	*-0.0256*	*6.8713*	*6.8030*	*-0.009933*	*0.0078*	*-0.0485*	*82*
Measurement 3	*16.200*	*15.8010*	*-0.0246*	*6.8713*	*6.8060*	*-0.009496*	*0.0088*	*-0.0466*	*82*
Measurement 4	*16.200*	*15.9140*	*-0.0177*	*6.8713*	*6.8250*	*-0.006731*	*0.0078*	*-0.0335*	*82*
Measurement 5	*16.200*	*15.9150*	*-0.0176*	*6.8713*	*6.8250*	*-0.006731*	*0.0072*	*-0.0334*	*82*

APPENDIX C

n=3 as reference

	Frequency			Quality Factor					
Mode 2	$f_0^{(n)}$ **[kHz]**	$f_{res}^{(n)}$ **[kHz]**	**$\Delta f/f_o$**	**Q_0**	**Q**	**$\Delta Q/Q_o$**	**$\Delta m/m_0$**	**$\Delta D/D_0$**	$f_{vac}^{(n)}$ **[kHz]**
		±0.00054	±0.00013		±0.00356	±0.00107	±0.00139	±0.00117	
C3COOH	**5.2418**	**5.2418**	**0.000**	**3.343**	**3.343**	**0.000**	**0.000**	**0.000**	**30**
Measurement 1	*5.2418*	*5.2419*	*0.0000*	*3.343*	*3.341*	*-0.0006*	*-0.0198*	*-0.0006*	*30*
Measurement 2	*5.2418*	*5.2423*	*0.0001*	*3.343*	*3.346*	*0.0009*	*0.0282*	*0.0010*	*30*
Measurement 3	*5.2418*	*5.2418*	*0.0000*	*3.343*	*3.346*	*0.0009*	*0.0294*	*0.0009*	*30*
Measurement 4	*5.2418*	*5.2410*	*-0.0002*	*3.343*	*3.339*	*-0.0012*	*-0.0373*	*-0.0014*	*30*
		±0.00356	±0.00067		±0.0004	±0.00028	±0.00114	±0.00116	
C8COOH	**5.2418**	**4.6380**	**-0.1152**	**3.343**	**3.1913**	**-0.0454**	**0.0029**	**-0.2064**	**30**
Measurement 1	*5.2418*	*4.6330*	*-0.1161*	*3.343*	*3.1900*	*-0.045767*	*0.0027*	*-0.2081*	*30*
Measurement 2	*5.2418*	*4.6410*	*-0.1146*	*3.343*	*3.1920*	*-0.045169*	*0.0018*	*-0.2055*	*30*
Measurement 3	*5.2418*	*4.6400*	*-0.1148*	*3.343*	*3.1920*	*-0.045169*	*0.0045*	*-0.2058*	*30*
Measurement 4	*5.2418*	*4.6380*	*-0.1152*	*3.343*	*3.1913*	*-0.045378*	*0.0026*	*-0.2064*	*30*
		±0.00688	±0.00129		±0.00175	±0.00052	±0.00021	±0.00231	
C11COOH	**5.2418**	**4.8010**	**-0.0841**	**3.343**	**3.2338**	**-0.0327**	**0.0064**	**-0.1529**	**30**
Measurement 1	5.2418	*4.8020*	*-0.0839*	*3.343*	*3.2340*	*-0.032605*	*0.0061*	*-0.1525*	*30*
Measurement 2	5.2418	*4.8101*	*-0.0824*	*3.343*	*3.2361*	*-0.031977*	*0.0064*	*-0.1498*	*30*
Measurement 3	5.2418	*4.7980*	*-0.0847*	*3.343*	*3.2330*	*-0.032905*	*0.0063*	*-0.1539*	*30*
Measurement 4	5.2418	*4.7940*	*-0.0854*	*3.343*	*3.2320*	*-0.033204*	*0.0066*	*-0.1552*	*30*
		±0.15287	±0.00099		±0.01573	±0.00041	±0.00106	±0.00099	
C16COOH	**5.2418**	**5.1114**	**-0.0249**	**3.343**	**3.3119**	**-0.0093**	**0.0085**	**-0.0463**	**30**
Measurement 1	*5.2418*	*5.1140*	*-0.0244*	*3.343*	*3.3125*	*-0.009124*	*0.0077*	*-0.0454*	*30*
Measurement 2	*5.2418*	*5.1100*	*-0.0251*	*3.343*	*3.3116*	*-0.009393*	*0.0086*	*-0.0468*	*30*
Measurement 3	*5.2418*	*5.1080*	*-0.0255*	*3.343*	*3.3110*	*-0.009572*	*0.0075*	*-0.0475*	*30*
Measurement 4	*5.2418*	*5.1190*	*-0.0234*	*3.343*	*3.3140*	*-0.008675*	*0.0104*	*-0.0436*	*30*
Measurement 5	*5.2418*	*5.1060*	*-0.0259*	*3.343*	*3.3106*	*-0.009692*	*0.0084*	*-0.0482*	*30*

APPENDIX C

n=3 as reference									
	Frequency			**Quality Factor**					
Mode 3	$f_0^{(n)}$ **[kHz]**	$f_{res}^{(n)}$ **[kHz]**	$\Delta f/f_o$	Q_0	**Q**	$\Delta Q/Q_o$	$\Delta m/m_0$	$\Delta D/D_0$	$f_{vac}^{(n)}$ **[kHz]**
		±0.0439	0.00267		±0.00129	±0.00017	±0.001226	±0.01129	
C3COOH	**16.279**	**16.277**	**0.000**	**6.885**	**6.885**	**0.000**	**0.000**	**0.000**	**82**
Measurement 1	*16.279*	*16.249*	*-0.0018*	*6.885*	*6.883*	*-0.0003*	*0.0112*	*-0.0031*	*82*
Measurement 2	*16.279*	*16.282*	*0.0002*	*6.885*	*6.884*	*-0.0001*	*-0.0055*	0.000137	*82*
Measurement 3	*16.279*	*16.245*	*-0.0021*	*6.885*	*6.886*	*0.0001*	*0.0248*	*-0.0031*	*82*
Measurement 4	*16.279*	*16.330*	*0.0031*	*6.885*	*6.885*	*0.0000*	*-0.0315*	*0.0048*	*82*
		±0.20332	0.0015		±0.1419	±0.00066	±0.00079	±0.02001	
C8COOH	**16.277**	**14.1165**	**-0.1328**	**6.885**	**6.5078**	**-0.0547**	**0.0022**	**-0.2303**	**82**
Measurement 1	*16.279*	*14.0800*	*-0.1351*	*6.885*	*6.5010*	*-0.055705*	*0.0018*	*-0.2439*	*82*
Measurement 2	*16.279*	*14.1340*	*-0.1318*	*6.885*	*6.5110*	*-0.054252*	*0.0025*	*-0.2383*	*82*
Measurement 3	*16.279*	*14.1300*	*-0.1320*	*6.885*	*6.5100*	*-0.054398*	*0.0014*	*-0.2387*	*82*
Measurement 4	*16.279*	*14.1220*	*-0.1325*	*6.885*	*6.5090*	*-0.054543*	*0.0032*	*-0.2006*	*82*
		±0.05331	0.0015		±0.0097	±0.00067	±0.00101	±0.00266	
C11COOH	**16.277**	**14.5573**	**-0.1058**	**6.885**	**6.5878**	**-0.0431**	**0.0039**	**-0.1937**	**82**
Measurement 1	*16.279*	*14.5260*	*-0.1077*	*6.885*	*6.5820*	*-0.043939*	*0.0033*	*-0.1970*	*82*
Measurement 2	*16.279*	*14.5490*	*-0.1063*	*6.885*	*6.5860*	*-0.043358*	*0.0028*	*-0.1946*	*82*
Measurement 3	*16.279*	*14.5800*	*-0.1044*	*6.885*	*6.5920*	*-0.042487*	*0.0046*	*-0.1912*	*82*
Measurement 4	*16.279*	*14.5740*	*-0.1047*	*6.885*	*6.5910*	*-0.042632*	*0.0049*	*-0.1919*	*82*
		±0.01952	0.0019		±0.00404	±0.00077	±0.0012	±0.00342	
C16COOH	**16.277**	**15.2702**	**-0.0620**	**6.885**	**6.7143**	**-0.0247**	**0.0064**	**-0.1158**	**82**
Measurement 1	*16.279*	*15.2460*	*-0.0635*	*6.885*	*6.7101*	*-0.025332*	*0.0066*	*-0.1185*	*82*
Measurement 2	*16.279*	*15.3100*	*-0.0595*	*6.885*	*6.7210*	*-0.023749*	*0.0057*	*-0.1114*	*82*
Measurement 3	*16.279*	*15.2970*	*-0.0603*	*6.885*	*6.7190*	*-0.02404*	*0.0067*	*-0.1128*	*82*
Measurement 4	*16.279*	*15.2480*	*-0.0633*	*6.885*	*6.7100*	*-0.025347*	*0.0049*	*-0.1183*	*82*
Measurement 5	*16.279*	*15.2500*	*-0.0632*	*6.885*	*6.7112*	*-0.025172*	*0.0081*	*-0.1180*	*82*

APPENDIX C

n=16 as ref									
	Frequency			**Quality Factor**					
Mode 2	$f_0^{(n)}$ **[kHz]**	$f_{res}^{(n)}$ **[kHz]**	$\Delta f/f_o$	Q_0	**Q**	$\Delta Q/Q_o$	$\Delta m/m_0$	$\Delta D/D_0$	$f_{vac}^{(n)}$ **[kHz]**
		±0.00238			±0.00238		±0.01355	±0.00129	
$C3CH_3$	**5.1136**	**5.311**	**0.0372**	**3.317**	**3.363**	**0.0139**	**-0.0216**	**0.0735**	**30**
Measurement 1	*5.1136*	*5.314*	*0.0377*	*3.317*	*3.364*	*0.0142*	*-0.0153*	*0.0743*	*30*
Measurement 2	*5.1136*	*5.309*	*0.0368*	*3.317*	*3.361*	*0.0133*	*-0.0382*	*0.0724*	*30*
Measurement 3	*5.1136*	*5.308*	*0.0366*	*3.317*	*3.362*	*0.0136*	*-0.0251*	*0.0724*	*30*
Measurement 4	*5.1136*	*5.313*	*0.0376*	*3.317*	*3.365*	*0.0145*	*-0.0078*	*0.0750*	*30*
		±0.0359			±0.00959		±0.00212	±0.0119	
$C8CH_3$	**5.1136**	**4.5056**	**-0.119**	**3.317**	**3.160**	**-0.0473**	**-0.015**	**-0.214**	**30**
Measurement 1	*5.1136*	*4.554*	*-0.1094*	*3.317*	*3.1730*	*-0.0434*	*-0.0134*	*-0.1969*	*30*
Measurement 2	*5.1136*	*4.510*	*-0.1180*	*3.317*	*3.1610*	*-0.0470*	*-0.0173*	*-0.2116*	*30*
Measurement 3	*5.1136*	*4.486*	*-0.1227*	*3.317*	*3.1550*	*-0.0488*	*-0.0131*	*-0.2194*	*30*
Measurement 4	*5.1136*	*4.472*	*-0.1254*	*3.317*	*3.1510*	*-0.0500*	*-0.0167*	*-0.2240*	*30*
							3.0000		
		±0.02329			±0.00591		±0.0166	±0.00807	
$C11CH_3$	**5.1136**	**4.8353**	**-0.0549**	**3.317**	**3.245**	**-0.0214**	**-0.0127**	**-0.101**	**30**
Measurement 1	*5.1136*	*4.811*	*-0.0592*	*3.317*	*3.2390*	*-0.0235*	*-0.0207*	*-0.1095*	*30*
Measurement 2	*5.1136*	*4.838*	*-0.0539*	*3.317*	*3.2460*	*-0.0214*	*-0.0201*	*-0.0999*	*30*
Measurement 3	*5.1136*	*4.860*	*-0.0496*	*3.317*	*3.2530*	*-0.0193*	*-0.0051*	*-0.0918*	*30*
Measurement 4	*5.1136*	*4.832*	*-0.0550*	*3.317*	*3.2460*	*-0.0214*	*-0.0048*	*-0.1015*	*30*
		±0.0068			±0.00158		±0.01626	±0.00227	
$C16CH_3$	**5.1136**	**5.1136**	**0.00**	**3.317**	**3.317**	**0.00**	**0.00**	**0.00**	**30**
Measurement 1	*5.1136*	*5.130*	*0.0032*	*3.317*	*3.315*	*-0.0006*	*-0.0626*	*0.0042*	*30*
Measurement 2	*5.1136*	*5.118*	*0.0009*	*3.317*	*3.316*	*-0.0003*	*-0.0216*	*-0.0202*	*30*
Measurement 3	*5.1136*	*5.122*	*0.0016*	*3.317*	*3.319*	*0.0006*	*-0.0007*	*0.0031*	*30*
Measurement 4	*5.1136*	*5.101*	*-0.0025*	*3.317*	*3.317*	*0.0000*	*0.0323*	*-0.0037*	*30*
Measurement 5	*5.1136*	*5.097*	*-0.0032*	*3.317*	*3.316*	*-0.0003*	*0.0322*	*-0.0052*	*30*

APPENDIX C

n=16 as ref									
	Frequency			**Quality Factor**					
Mode 3	$f_0^{(n)}$ **[kHz]**	$f_{res}^{(n)}$ **[kHz]**	**$\Delta f/f_o$**	**Q_0**	**Q**	**$\Delta Q/Q_o$**	**$\Delta m/m_0$**	**$\Delta D/D_0$**	$f_{vac}^{(n)}$ **[kHz]**
		±0.0.0223			±0.0278		±0.01263	±0.05837	
$C3CH_3$	**15.838**	**16.2365**	**0.0252**	**6.8122**	**6.8763**	**0.0094**	**-0.0291**	**0.0170**	**82**
Measurement 1	*15.838*	*16.3500*	0.0323	*6.8122*	*6.8900*	*0.0114*	*0.0659*	*0.0470*	*82*
Measurement 2	*15.838*	*16.2300*	0.0248	*6.8122*	*6.9200*	*0.0158*	*-0.0050*	*0.0515*	*82*
Measurement 3	*15.838*	*16.1860*	0.0220	*6.8122*	*6.8500*	*0.0055*	*-0.0808*	*0.0396*	*82*
Measurement 4	*15.838*	*16.1800*	0.0216	*6.8122*	*6.8450*	*0.0048*	*-0.0964*	*-0.0703*	*82*
		±0.02059			±0.00411		±0.00135	±0.00215	
$C8CH_3$	**15.838**	**13.5593**	**-0.144**	**6.8122**	**6.4023**	**-0.060**	**-0.017**	**-0.259**	**82**
Measurement 1	*15.838*	*13.547*	*-0.1447*	*6.8122*	*6.4010*	*-0.0604*	*-0.0131*	*-0.2602*	*82*
Measurement 2	*15.838*	*13.600*	*-0.1413*	*6.8122*	*6.4070*	*-0.0595*	*-0.0295*	*-0.2551*	*82*
Measurement 3	*15.838*	*13.560*	*-0.1438*	*6.8122*	*6.4030*	*-0.0601*	*-0.0149*	*-0.2589*	*82*
Measurement 4	*15.838*	*13.530*	*-0.1457*	*6.8122*	*6.3980*	*-0.0608*	*-0.0124*	*-0.2620*	*82*
		±0.07736			±0.01425		±0.00514	±0.00869	
$C11CH_3$	**15.838**	**14.5665**	**-0.0803**	**6.8122**	**6.5893**	**-0.0327**	**-0.0167**	**-0.1492**	**82**
Measurement 1	*15.838*	*14.4800*	*-0.0857*	*6.8122*	*6.5830*	*-0.0336*	*-0.0173*	*-0.1581*	*82*
Measurement 2	*15.838*	*14.6200*	*-0.0769*	*6.8122*	*6.5940*	*-0.0320*	*-0.0237*	*-0.1436*	*82*
Measurement 3	*15.838*	*14.6610*	*-0.0743*	*6.8122*	*6.6060*	*-0.0303*	*-0.0045*	*-0.1384*	*82*
Measurement 4	*15.838*	*14.5050*	*-0.0842*	*6.8122*	*6.5740*	*-0.0350*	*-0.0214*	*-0.1565*	*82*
		±0.07053			±0.01332		±0.00066	±0.0085	
$C16CH_3$	**15.838**	**15.8380**	**0.000**	**6.8122**	**6.8122**	**0.000**	**0.000**	**0.000**	**82**
Measurement 1	*15.838*	*15.7780*	*-0.0038*	*6.8122*	*6.8020*	*-0.0015*	*0.0002*	*-0.0073*	*82*
Measurement 2	*15.838*	*15.7840*	*-0.0034*	*6.8122*	*6.8030*	*-0.0014*	*0.0001*	*-0.0066*	*82*
Measurement 3	*15.838*	*15.8000*	*-0.0024*	*6.8122*	*6.8060*	*-0.0009*	*0.0011*	*-0.0046*	*82*
Measurement 4	*15.838*	*15.9130*	*0.0047*	*6.8122*	*6.8250*	*0.0019*	*0.0001*	*0.0092*	*82*
Measurement 5	*15.838*	*15.9150*	*0.0049*	*6.812*	*6.8250*	*0.0019*	*-0.0012*	*0.0093*	*82*

APPENDIX C

n=16 as reference									
	Frequency			**Quality Factor**					
Mode 2	$f_0^{(n)}$ **[kHz]**	$f_{res}^{(n)}$ **[kHz]**	**$\Delta f/f_o$**	**Q_0**	**Q**	**$\Delta Q/Q_o$**	**$\Delta m/m_0$**	**$\Delta D/D_0$**	$f_{vac}^{(n)}$ **[kHz]**
		±0.00054			±0.00356		±0.03553	±0.00124	
C3COOH	**5.1114**	**5.2407**	**0.0253**	**3.313**	**3.343**	**0.0091**	**-0.0169**	**0.0481**	**30**
Measurement 1	*5.1114*	*5.2413*	*0.0254*	*3.313*	*3.341*	*0.0085*	*-0.0391*	*0.0474*	*30*
Measurement 2	*5.1114*	*5.2406*	*0.0253*	*3.313*	*3.346*	*0.0100*	*0.0140*	*0.0488*	*30*
Measurement 3	*5.1114*	*5.2407*	*0.0253*	*3.313*	*3.346*	*0.0100*	*0.0138*	*0.0488*	*30*
Measurement 4	*5.1114*	*5.2400*	*0.0252*	*3.313*	*3.339*	*0.0078*	*-0.0564*	*0.0464*	*30*
		±0.00356			±0.00094		±0.00118	±0.00121	
C8COOH	**5.1114**	**4.6367**	**-0.0931**	**3.313**	**3.1913**	**-0.0367**	**-0.0140**	**-0.1685**	**30**
Measurement 1	*5.1114*	*4.6370*	*-0.0928*	*3.313*	*3.1900*	*-0.0371*	*-0.0293*	*-0.1688*	*30*
Measurement 2	*5.1114*	*4.6385*	*-0.0926*	*3.313*	*3.1920*	*-0.0365*	*-0.0117*	*-0.1679*	*30*
Measurement 3	*5.1114*	*4.6370*	*-0.0928*	*3.313*	*3.1920*	*-0.0365*	*-0.0075*	*-0.1683*	*30*
Measurement 4	*5.1114*	*4.6344*	*-0.0943*	*3.313*	*3.1913*	*-0.0367*	*-0.0077*	*-0.1692*	*30*
		±0.00688			±0.00175		±0.02697	±0.00203	
C11COOH	**5.1114**	**4.7969**	**-0.0615**	**3.313**	**3.2338**	**-0.0235**	**-0.0176**	**-0.1113**	**30**
Measurement 1	*5.1114*	*4.7600*	*-0.0687*	*3.313*	*3.2230*	*-0.027166*	*-0.0166*	*-0.1264*	*30*
Measurement 2	*5.1114*	*4.8090*	*-0.0592*	*3.313*	*3.2361*	*-0.023212*	*-0.0107*	*-0.1091*	*30*
Measurement 3	*5.1114*	*4.7985*	*-0.0612*	*3.313*	*3.2330*	*-0.024147*	*-0.0152*	*-0.1129*	*30*
Measurement 4	*5.1114*	*4.8200*	*-0.0570*	*3.313*	*3.2370*	*-0.02294*	*-0.0311*	*-0.1058*	*30*
		±0.15287			±0.01573		±0.01628	±0.00453	
C16COOH	**5.1114**	**5.1114**	**0.000**	**3.313**	**3.313**	**0.000**	**0.003**	**0.000**	**30**
Measurement 1	*5.1114*	*5.1140*	*0.0005*	*3.313*	*3.3125*	*-0.000151*	*-0.0119*	*0.0006*	*30*
Measurement 2	*5.1114*	*5.1100*	*-0.0003*	*3.313*	*3.3119*	*-0.000332*	*-0.0078*	*-0.0007*	*30*
Measurement 3	*5.1114*	*5.1080*	*-0.0007*	*3.313*	*3.3140*	*0.0003018*	*0.0191*	*-0.0007*	*30*
Measurement 4	*5.1114*	*5.1190*	*0.0015*	*3.313*	*3.3170*	*0.0012074*	*0.0221*	*0.0035*	*30*
Measurement 5	*5.1114*	*5.1060*	*-0.0011*	*3.313*	*3.3110*	*-0.000604*	*-0.0069*	*-0.0022*	*30*

APPENDIX C

n=16 as reference	Frequency			Quality Factor					
Mode 3	$f_0^{(n)}$ [kHz]	$f_{res}^{(n)}$ [kHz]	$\Delta f/f_o$	Q_0	Q	$\Delta Q/Q_o$	$\Delta m/m_0$	$\Delta D/D_0$	$f_{vac}^{(n)}$ [kHz]
		±0.0439			±0.00129		±0.03041	±0.00474	
C3COOH	**15.2702**	**16.279**	**0.0661**	**6.1760**	**6.885**	**0.0253**	**-0.0088**	**0.1309**	**82**
Measurement 1	*15.2702*	*16.249*	*0.0641*	*6.7143*	*6.883*	*0.0251*	*0.0059*	*0.1274*	*82*
Measurement 2	*15.2702*	*16.282*	*0.0663*	*6.7143*	*6.884*	*0.0253*	*-0.0130*	*0.1311*	*82*
Measurement 3	*15.2702*	*16.245*	*0.0638*	*6.7143*	*6.886*	*0.0256*	*0.0212*	*0.1275*	*82*
Measurement 4	*15.2702*	*16.340*	*0.0701*	*6.7143*	*6.885*	*0.0254*	*-0.0493*	*0.1375*	*82*
		±0.20332			±0.1419		±0.00091	±0.00289	
C8COOH	**15.2702**	**14.1165**	**-0.0756**	**6.1760**	**6.5078**	**-0.0308**	**-0.0057**	**-0.1405**	**82**
Measurement 1	*15.2702*	*14.0800*	*-0.0779*	*6.7143*	*6.5010*	*-0.03177*	*-0.0062*	*-0.1448*	*82*
Measurement 2	*15.2702*	*14.1340*	*-0.0744*	*6.7143*	*6.5110*	*-0.03028*	*-0.0055*	*-0.1385*	*82*
Measurement 3	*15.2702*	*14.1300*	*-0.0747*	*6.7143*	*6.5100*	*-0.03043*	*-0.0067*	*-0.1390*	*82*
Measurement 4	*15.2702*	*14.1220*	*-0.0752*	*6.7143*	*6.5090*	*-0.03058*	*-0.0046*	*-0.1399*	*82*
		±0.05331			±0.0097		±0.00112	±0.00304	
C11COOH	**15.2702**	**14.5573**	**-0.0467**	**6.1760**	**6.5878**	**-0.0188**	**-0.0035**	**-0.0881**	**82**
Measurement 1	*15.2702*	*14.5260*	*-0.0487*	*6.7143*	*6.5820*	*-0.019704*	*-0.0042*	*-0.0919*	*82*
Measurement 2	*15.2702*	*14.5490*	*-0.0472*	*6.7143*	*6.5860*	*-0.019108*	*-0.0047*	*-0.0891*	*82*
Measurement 3	*15.2702*	*14.5800*	*-0.0452*	*6.7143*	*6.5920*	*-0.018215*	*-0.0027*	*-0.0853*	*82*
Measurement 4	*15.2702*	*14.5740*	*-0.0456*	*6.7143*	*6.5910*	*-0.018364*	*-0.0024*	*-0.0860*	*82*
		±0.01952			±0.00404		±0.00138	±0.00388	
C16COOH	**15.2702**	**15.2702**	**0.000**	**6.7143**	**6.7143**	**0.000**	**0.000**	**0.000**	**82**
Measurement 1	*15.2702*	*15.2460*	*-0.0016*	*6.7143*	*6.7101*	*-0.000626*	*0.0001*	*-0.0030*	*82*
Measurement 2	*15.2702*	*15.3100*	*0.0026*	*6.7143*	*6.7210*	*0.0009979*	*-0.0009*	*0.0050*	*82*
Measurement 3	*15.2702*	*15.2970*	*0.0018*	*6.7143*	*6.7190*	*0.0007*	*0.0002*	*0.0034*	*82*
Measurement 4	*15.2702*	*15.2480*	*-0.0015*	*6.7143*	*6.7100*	*-0.00064*	*-0.0019*	*-0.0029*	*82*
Measurement 5	*15.2702*	*15.2500*	*-0.0013*	*6.7143*	*6.7112*	*-0.000462*	*0.0018*	*-0.0025*	*82*

APPENDIX D – Resonance frequency and quality factor data for vancomycin-mucopeptide complexes

BI – *Before* injection of vancomycin, AI – *After* injection of vancomycin

G05: 10µM vancomycin concentration

Cantilever		$f_{res}^{(n)}$[kHz] BI	$f_{res}^{(n)}$[kHz] AI	$\Delta f/f_0$	Q (BI)	Q (AI)	$\Delta Q/Q_0$	$\Delta m/m_0$	$\Delta D/D_0$	$f_{vac}^{(n)}$ [kHz]
2	PEG	5.433	5.410	-0.0042	2.247	2.238	-0.0040	-0.0729	-0.0104	30
3	Dala	5.439	5.480	0.0075	2.254	2.261	0.0031	0.0071	0.0146	30
4	Dala	5.360	5.390	0.0056	2.249	2.255	0.0027	0.0167	0.0112	30
5	Dala	5.289	5.310	0.0040	2.244	2.247	0.0013	-0.0056	0.0074	30
6	PEG	5.310	5.270	-0.0075	2.291	2.280	-0.0048	-0.0616	-0.0161	30
7	Dala	5.287	5.320	0.0062	2.243	2.250	0.0031	0.0239	0.0126	30
8	PEG	5.367	5.342	-0.0047	2.264	2.253	-0.0049	-0.0964	-0.0119	30

G05: 50µM vancomycin concentration

Cantilever		$f_{res}^{(n)}$[kHz] BI	$f_{res}^{(n)}$[kHz] AI	$\Delta f/f_0$	Q (BI)	Q (AI)	$\Delta Q/Q_0$	$\Delta m/m_0$	$\Delta D/D_0$	$f_{vac}^{(n)}$ [kHz]
2	PEG	5.422	5.400	-0.0041	2.241	2.231	-0.0045	-0.0893	-0.0106	30
3	Dala	5.310	5.420	0.0207	2.251	2.271	0.0089	0.0326	0.0406	30
4	Dala	5.180	5.270	0.0174	2.267	2.284	0.0075	0.0305	0.0341	30
5	Dala	5.344	5.450	0.0198	2.248	2.266	0.0080	0.0151	0.0384	30
6	PEG	5.503	5.460	-0.0078	2.269	2.257	-0.0053	-0.0685	-0.0170	30
7	Dala	5.198	5.310	0.0215	2.237	2.248	0.0049	0.040624	0.0424	30
8	PEG	5.484	5.462	-0.0040	2.243	2.233	-0.0045	-0.0877	-0.0105	30

BI – *Before* injection of vancomycin, AI – *After* injection of vancomycin

G05: 100μM vancomycin concentration

Cantilever		$f_{res}^{(n)}$ [kHz] BI	$f_{res}^{(n)}$ [kHz] AI	$\Delta f / f_0$	Q (BI)	Q (AI)	$\Delta Q/Q_0$	$\Delta m/m_0$	$\Delta D/D_0$	$f_{vac}^{(n)}$ [kHz]
2	PEG	5.124	5.100	-0.0047	2.075	2.070	-0.0024	-0.0215	-0.0095	30
3	Dala	5.150	5.330	0.0350	2.121	2.154	0.0156	0.0796	0.0697	30
4	Dala	5.174	5.350	0.0340	2.142	2.173	0.0145	0.0545	0.0671	30
5	Dala	5.070	5.250	0.0355	2.110	2.142	0.0152	0.0620	0.0701	30
6	PEG	5.323	5.300	-0.0043	2.137	2.130	-0.0033	-0.0518	-0.0098	30
7	Dala	5.064	5.271	0.0409	2.117	2.154	0.0175	0.0727	0.0810	30
8	PEG	5.122	5.100	-0.0043	2.104	2.094	-0.0048	-0.0746	-0.0103	30

F10 500 μM vancomycin concentration

Cantilever		$f_{res}^{(n)}$ [kHz] BI	$f_{res}^{(n)}$ [kHz] AI	$\Delta f / f_0$	Q (BI)	Q (AI)	$\Delta Q/Q_0$	$\Delta m/m_0$	$\Delta D/D_0$	$f_{vac}^{(n)}$ [kHz]
1	PEG	5.397	5.371	-0.0048	2.1560	2.146	-0.00464	-0.08663	-0.01188	30
2	DAla	5.271	5.481	0.0398	2.204	2.264	0.02722	0.2583	0.0854	30
3	PEG	5.198	5.250	0.0100	2.187	2.194	0.00320	-0.0198	0.0184	30
4	PEG	5.322	5.377	0.0103	2.276	2.281	0.00237	-0.0492	0.0181	30
5	DAla	5.397	5.580	0.0339	2.255	2.298	0.01907	0.1901	0.0718	30
6	DAla	5.283	5.503	0.0416	2.211	2.261	0.02261	0.2190	0.0877	30
7	PEG	5.334	5.318	-0.0030	2.281	2.276	-0.00219	-0.0332	-0.0067	30
8	DAla	5.301	5.480	0.0338	2.198	2.245	0.02148	0.2750	0.0741	30

APPENDIX D

BI – *Before* injection of vancomycin, AI – *After* injection of vancomycin

F15 500 µM vancomycin concentration

Cantilever		$f_{res}^{(n)}$ **[kHz] BI**	$f_{res}^{(n)}$ **[kHz] AI**	$\Delta f/f_0$	**Q (BI)**	**Q (AI)**	$\Delta Q/Q_0$	$\Delta m/m_0$	$\Delta D/D_0$	$f_{vac}^{(n)}$ **[kHz]**
1	DAla	5.340	5.520	0.0337	2.2600	2.30	0.01770	0.15422	0.070017	30
2	Dala	5.310	5.544	0.0441	2.251	2.301	0.02221	0.1756	0.0911	30
3	PEG	5.405	5.383	-0.0041	2.271	2.265	-0.00264	-0.0335	-0.0088	30
4	PEG	5.412	5.381	-0.0057	2.231	2.220	-0.00493	-0.0844	-0.0135	30
5	DAla	5.421	5.670	0.0459	2.175	2.216	0.01885	0.0463	0.0905	30
6	PEG	5.334	5.308	-0.0049	2.254	2.248	-0.00266	-0.0254	-0.0100	30
7	DAla	5.384	5.540	0.0290	2.279	2.320	0.01799	0.2151	0.0629	30
8	DAla	5.371	5.547	0.0328	2.198	2.242	0.02002	0.2669	0.0666	30

G05 500 µM vancomycin concentration

Cantilever		$f_{res}^{(n)}$ **[kHz] BI**	$f_{res}^{(n)}$ **[kHz] AI**	$\Delta f/f_0$	**Q (BI)**	**Q (AI)**	$\Delta Q/Q_0$	$\Delta m/m_0$	$\Delta D/D_0$	$f_{vac}^{(n)}$ **[kHz]**
2	PEG	5.220	5.200	-0.0038	2.155	2.150	-0.0023	-0.0284	-0.0081	30
3	Dala	5.268	5.428	0.0304	2.197	2.226	0.0132	0.0551	0.0601	30
4	Dala	5.260	5.434	0.0331	2.180	2.227	0.0216	0.2905	0.0731	30
5	Dala	5.350	5.511	0.0301	2.234	2.239	0.0022	-0.2833	0.0482	30
6	PEG	5.286	5.360	0.0140	2.240	2.250	0.0045	-0.0272	0.0258	30
7	Dala	5.218	5.489	0.0519	2.157	2.235	0.0362	0.5375	0.1186	30
8	PEG	5.272	5.240	-0.0061	2.201	2.190	-0.0050	-0.0870	-0.0141	30

APPENDIX E

Resonance frequency and quality factor data for ethanol and glycerol solutions, and commercial drinks

Aspect Ratio 10:1

Mode 2

Solution	$f_{med}^{(n)}$ kHz	$Q_{med}^{(n)}$	ρ [kg m^{-3}]	η [kg m^{-1} s^{-1}]
0%ethanol (100% water)	3.95	2.35	0.917	0.640
20% ethanol	3.49	1.48	0.902	1.939
40% ethanol	3.38	1.30	0.848	2.624
60%ethanol	3.45	1.32	0.814	2.399
80% ethanol	3.74	1.49	0.783	1.718
100% ethanol	4.06	1.81	0.725	1.032

Mode 3

Solution	$f_{med}^{(n)}$ kHz	$Q_{med}^{(n)}$	ρ [kg m^{-3}]	η [kg m^{-1} s^{-1}]
0%ethanol (100% water)	19.02	3.22	0.952	0.750
20% ethanol	17.97	2.44	0.942	1.880
40% ethanol	16.84	2.28	0.902	2.650
60%ethanol	17.60	2.35	0.820	2.321
80% ethanol	18.43	2.62	0.779	1.710
100% ethanol	19.58	3.20	0.742	1.106

APPENDIX E

Aspect Ratio 10:1

Mode 2

Solution	$f_{med}^{(n)}$ kHz	$Q_{med}^{(n)}$	ρ [kg m^{-3}]	η [kg m^{-1} s^{-1}]
0% glycerol (100% water)	3.95	2.35	0.957	0.640
20% glycerol	2.68	1.02	1.083	5.855
40% glycerol	2.51	0.84	1.032	12.892
60% glycerol	2.08	0.61	0.967	21.831
80% glycerol	1.32	0.382	0.943	57.084

Mode 3

Solution	$f_{med}^{(n)}$ kHz	$Q_{med}^{(n)}$	ρ [kg m^{-3}]	η [kg m^{-1} s^{-1}]
0% glycerol (100% water)	19.02	3.22	0.950	0.830
20% glycerol	18.8	1.496	1.072	9.800
40% glycerol	16.85	1.325	1.040	11.100
60% glycerol	15.26	0.687	0.970	21.800
80% glycerol	12.51	0.5414	0.940	73.000

APPENDIX E

Aspect Ratio 13:1

Mode 2

Solution	$f_{med}^{(n)}$ kHz	$Q_{med}^{(n)}$	ρ [kg m$^{-3]}$	η [kg m^{-1} s^{-1}]
0%ethanol (100% water)	6.85	1.776	0.964	0.712
20% ethanol	5.960	1.540	0.929	1.976
40% ethanol	5.700	1.300	0.899	2.682
60%ethanol	5.962	1.452	0.845	2.457
80% ethanol	5.750	1.340	0.799	1.745
100% ethanol	6.043	1.404	0.753	1.101

Mode 3

Solution	$f_{med}^{(n)}$ kHz	$Q_{med}^{(n)}$	ρ [kg m$^{-3]}$	η [kg m^{-1} s^{-1}]
0%ethanol (100% water)	50.84	3.30	0.975	0.780
20% ethanol	45.93	3.10	0.895	2.001
40% ethanol	45.80	3.00	0.870	2.733
60%ethanol	46.00	2.79	0.855	2.370
80% ethanol	46.21	2.75	0.800	1.818
100% ethanol	49.19	3.25	0.740	1.154

APPENDIX E

Aspect Ratio 13:1

Mode 2

Solution	$f_{med}^{(n)}$ kHz	$Q_{med}^{(n)}$	ρ [kg m^{-3}]	η [kg m^{-1} s^{-1}]
0% glycerol (100% water)	6.88	1.846	0.958	0.980
20% glycerol	5.040	1.340	1.099	6.100
40% glycerol	4.870	1.003	1.069	10.760
60% glycerol	3.262	0.852	0.987	20.000
80% glycerol	2.250	0.540	0.961	55.000

Mode 3

Solution	$f_{med}^{(n)}$ kHz	$Q_{med}^{(n)}$	ρ [kg m^{-3}]	η [kg m^{-1} s^{-1}]
0% glycerol (100% water)	50.94	3.18	0.850	0.910
20% glycerol	34.83	2.10	0.965	11.643
40% glycerol	29.18	1.77	0.960	15.523
60% glycerol	20.11	1.27	0.881	24.429
80% glycerol	15.11	1.02	0.843	75.354

Mode 2

Drink	$f_{med}^{(n)}$ kHz	$Q_{med}^{(n)}$	ρ [kg m^{-3}]	η [kg m^{-1} s^{-1}]
Whisky 40%	3.56	1.25	876.1640	0.0025
Gin 37.5%	3.35	1.21	875.4080	0.0025
Vodka 37.5%	3.47	1.30	883.8930	0.0025
White Wine 12%	3.76	1.78	931.2420	0.0014
Beer 3.8%	3.88	1.66	927.1520	0.0009
beer 0%	3.94	1.86	935.2920	0.0006

APPENDIX E

Aspect Ratio 5:1

Mode 2

Solution	$f_{med}^{(n)}$ kHz	$Q_{med}^{(n)}$	ρ [kg m^{-3}]	η [kg m^{-1} s^{-1}]
0%ethanol (100% water)	5.816	3.313	0.840	0.500
20% ethanol	5.382	2.511	0.815	1.584
40% ethanol	5.099	2.385	0.757	2.340
60%ethanol	5.195	2.540	0.753	2.077
80% ethanol	5.426	3.081	0.704	1.485
100% ethanol	6.011	3.799	0.659	0.975

Mode 3

Solution	$f_{med}^{(n)}$ kHz	$Q_{med}^{(n)}$	ρ [kg m^{-3}]	η [kg m^{-1} s^{-1}]
0%ethanol (100% water)	17.990	5.263	0.809	0.562
20% ethanol	17.316	4.695	0.789	1.654
40% ethanol	16.253	3.710	0.773	2.299
60%ethanol	16.570	4.180	0.753	1.961
80% ethanol	17.310	5.183	0.677	1.369
100% ethanol	18.794	5.809	0.647	0.848

APPENDIX E

Aspect Ratio 5:1

Mode 2

Solution	$f_{med}^{(n)}$ kHz	$Q_{med}^{(n)}$	ρ [kg m^{-3}]	η [kg m^{-1} s^{-1}]
0% glycerol (100% water)	5.810	3.240	0.820	0.910
20% glycerol	4.28	1.89	0.975	7.643
40% glycerol	3.97	1.46	0.935	14.523
60% glycerol	3.79	1.16	0.841	25.243
80% glycerol	3.162	0.821	0.824	60.354

Mode 3

Solution	$f_{med}^{(n)}$ kHz	$Q_{med}^{(n)}$	ρ [kg m^{-3}]	η [kg m^{-1} s^{-1}]
0% glycerol (100% water)	17.11	5.60	0.850	0.910
20% glycerol	9.80	2.24	0.965	11.643
40% glycerol	9.50	2.07	0.960	15.523
60% glycerol	9.19	1.60	0.881	24.429
80% glycerol	7.71	1.03	0.843	75.354

APPENDIX F – Mathematica notebooks

Fitting procedure for resonance peak

Mathematica notebook to extract resonant frequency and quality factor from resonance peak.

To run:
(1) Enter the directory and filename of the data file
(2) Specify the type of data (amplitude or dB)
(3) Type ffit[fpeak, Q, fmin, fmax], where
    fpeak is an estimate of the resonant frequency
    Q is an estimate of the quality factor
    fmin & fmax define the frequency interval over which to fit the data.
(4) Run the entire notebook.

NOTE: (1) Notebook reads data files containing two columns (frequency, value).
(2) Frequency units are specified by those in the data file.
(3) Frequency division between all data points must be the same.

Fitting procedure

COMPATIBILITYISSUE

```
Clear["Global`*"]
```

Set the directory containingthe data file and data file name:

```
SetDirectory["C:\\Users\\Rosemary Paxman\\Desktop"];
datac1 = ReadList["jake.txt", {Number, Number}];
ListLogPlot[datac1, PlotRange → All]
filename = "40Au_max_therm_A.txt";
```

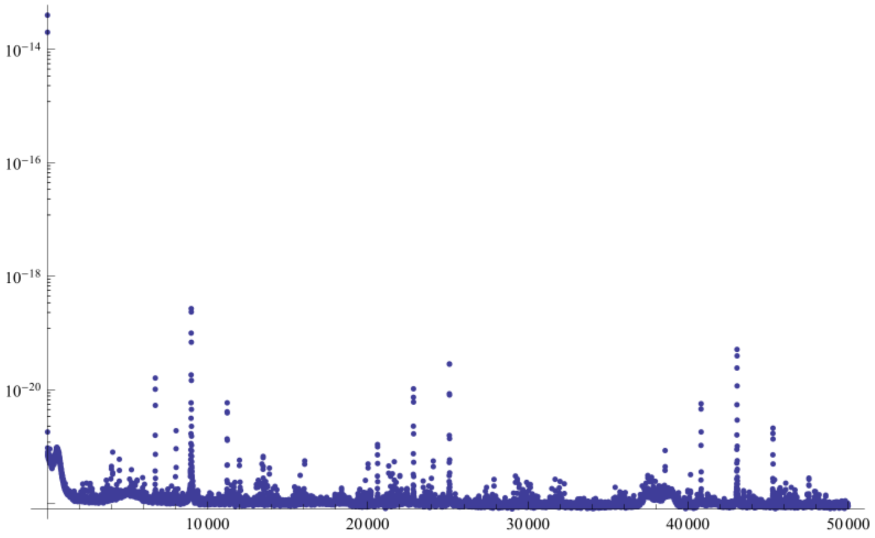

If you would like to cut the data, then put the ranges in here.

```
cutMax = 6700;
cutMin = 3000;
```

This will show you the data you are now fitting to.

```
datac2 = If[cutMax ≠ 0 && cutMin ≠ 0,
   Sort[DeleteCases[Map[If[cutMin > #[[1]] || #[[1]] > cutMax, 0, #] &, datac1 ], 0]] /.
    {f_, u_} → {f, (u)^2}, datac1 /. {f_, u_} → {f, (u)^2}];
ListLogPlot[datac2, PlotRange → All]
```

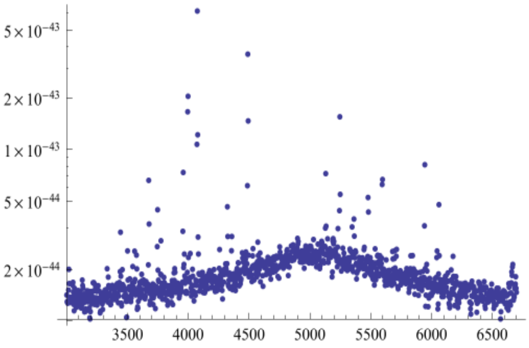

This section fits a line to a constant background. The range is in Hz. However if the background noise is to small to effect the fit then select one (or both) as zero.

```
MinRange = 10 000;
MaxRange = 20 000;
```

Specify the nature of the data (1 for linear amplitude spectra; 0 for dB power spectra)

```
linear = 1;
```

Functions

```
If[MinRange == 0 || MaxRange == 0,
 List3 = {0, 0};,

 line = NonlinearModelFit[
   DeleteCases[Map[If[MinRange > #[[1]] || #[[1]] > MaxRange, 0, #] &, datac1], 0], a, a, x];
 Print[Show[ListPlot[DeleteCases[Map[If[MinRange > #[[1]] || #[[1]] > MaxRange, 0, #] &,
      datac1 ], 0]], Plot[line[x], {x, MinRange, MaxRange}, PlotStyle → Black]]];
 List3 = {line["ParameterTable"][[1, 1, 2, 2]], line["ParameterTable"][[1, 1, 2, 3]]};
 datac = Map[{#[[1]], If[#[[2]] - List3[[1]] < 0, 10^-11, #[[2]] - List3[[1]]]} &, datac2];
 ListLogPlot[datac, PlotRange → All]]
```

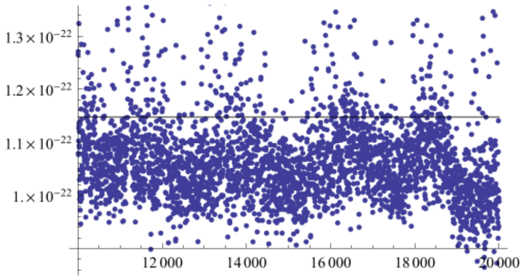

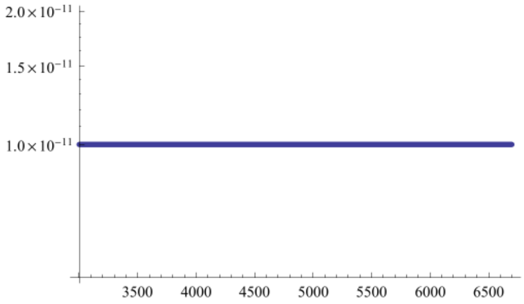

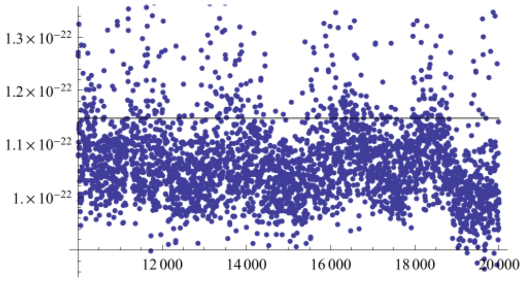

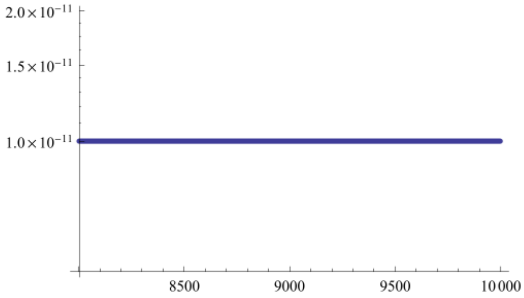

Frequency step in datafile (no changes required):

Frequency step in datafile (no changes required):

```
freqstep = ( datac[[-1]][[1]] - datac[[1]][[1]] ) / (Length[datac] - 1)
  (* frequency division *);
```

Fitting routine (no changes required):

```
maxnum = Length[datac];
Apeak = 1;

List1 = {}; List2 = {};
ffit[fpeak_, Qest_, ffmin_, ffmax_, g_] := Module[{setting1},


   ffmin1 = Floor[(ffmin - datac1[[1]][[1]]) / freqstep] + 1;
   ffmax1 = Floor[(ffmax - datac1[[1]][[1]]) / freqstep] + 1;
   max = 0;

   kb = 1.38 × 10^-23;
   T = 293.15;

   If[linear == 0,
    For[i = ffmin1, i ≤ ffmax1, i++,
     sub = 10 ^ (datac[[i]][[2]] / 20); If[sub > max, max = sub];];
    data2 = Table[{datac[[i]][[1]], 10 ^ (datac[[i]][[2]] / 20) / max}, {i, ffmin1, ffmax1}],
    For[i = ffmin1, i ≤ ffmax1, i++, If[datac1[[i]][[2]] > max, max = datac1[[i]][[2]]];];
    data2 = Table[{datac1[[i]][[1]], datac1[[i]][[2]] / max}, {i, ffmin1, ffmax1}];
   ];



   lp0 = ListPlot[data2, PlotRange → All];
```

$$\mathtt{model6[f\_,\ fm\_,\ Qm\_,\ km\_]} := \frac{1}{\mathrm{max}}\left(10^{9}\sqrt{\frac{\mathrm{kb}\ \mathrm{T}}{\mathrm{km}}\ \frac{2}{\pi\ \mathrm{fm}\ \mathrm{Qm}}\ \frac{\mathrm{fm}^4}{\left(\mathrm{fm}^2-\mathrm{f}^2\right)^2+\frac{\mathrm{f}^2\ \mathrm{fm}^2}{\mathrm{Qm}^2}}}\right)^2;$$

```
   klist = DeleteDuplicates[List1, #1[[-1]] == #2[[-1]] &] /.
     {asds1___, {asds___, ft_String /; ft == g}, asds2___} → {asds1, asds2};
   model7[ff_] := Total[Table[model6[ff, klist[[ii, 1]], klist[[ii, 3]], klist[[ii, 5]]],
      {ii, 1, Length[klist]}]];
   data2 = data2 /. {fff_, dd_} → {fff, dd - model7[fff]};

   klist2 = DeleteDuplicates[List2, #1[[-1]] == #2[[-1]] &] /.
```

APPENDIX F

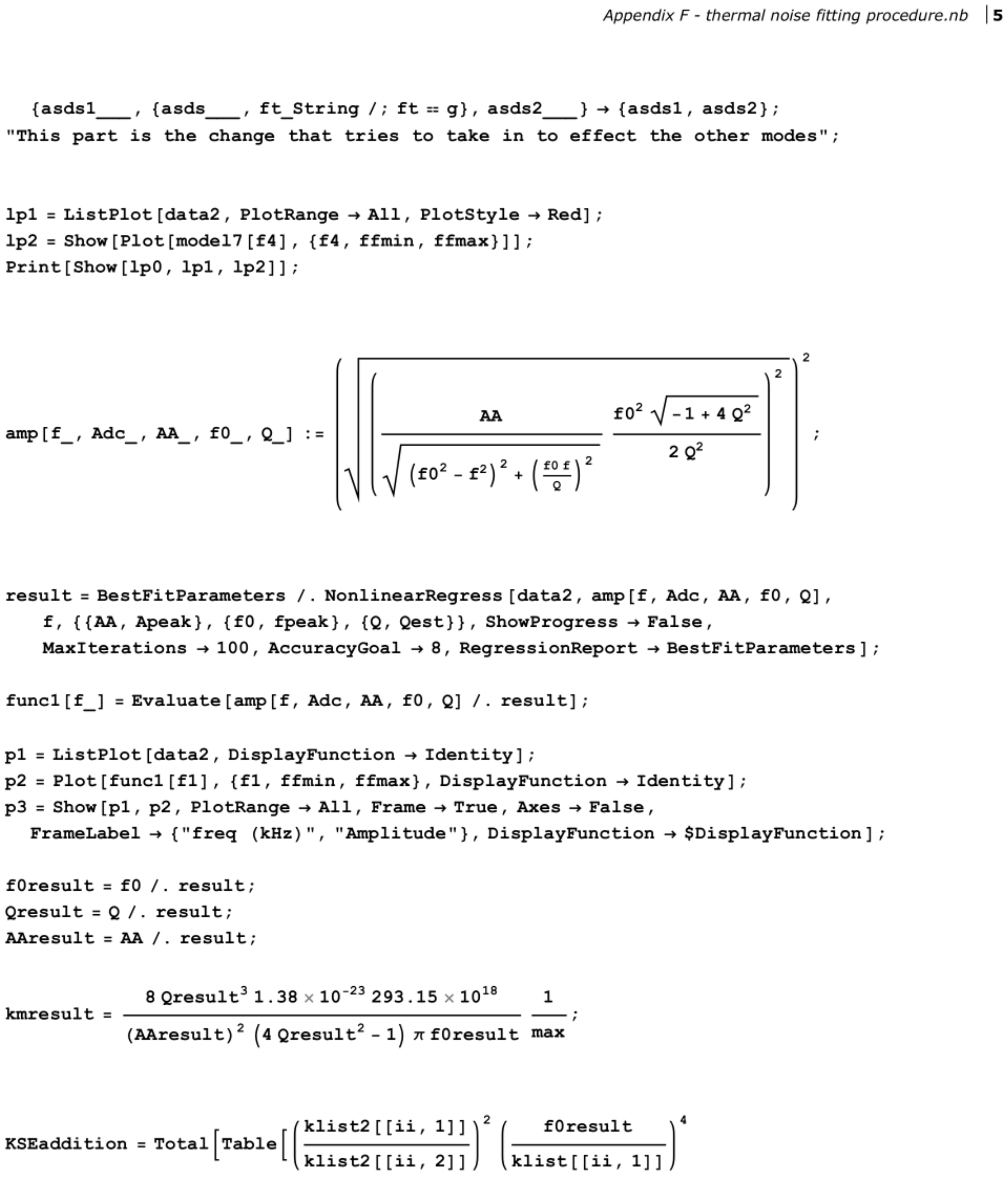

```
  {asds1___, {asds___, ft_String /; ft == g}, asds2___} → {asds1, asds2};
"This part is the change that tries to take in to effect the other modes";


lp1 = ListPlot[data2, PlotRange → All, PlotStyle → Red];
lp2 = Show[Plot[model7[f4], {f4, ffmin, ffmax}]];
Print[Show[lp0, lp1, lp2]];
```

$$amp[f\_, Adc\_, AA\_, f0\_, Q\_] := \left(\sqrt{\left(\frac{AA}{\sqrt{\left(f0^2-f^2\right)^2+\left(\frac{f0\,f}{Q}\right)^2}}\;\frac{f0^2\sqrt{-1+4\,Q^2}}{2\,Q^2}\right)^2}\right)^2;$$

```
result = BestFitParameters /. NonlinearRegress[data2, amp[f, Adc, AA, f0, Q],
    f, {{AA, Apeak}, {f0, fpeak}, {Q, Qest}}, ShowProgress → False,
    MaxIterations → 100, AccuracyGoal → 8, RegressionReport → BestFitParameters];

func1[f_] = Evaluate[amp[f, Adc, AA, f0, Q] /. result];

p1 = ListPlot[data2, DisplayFunction → Identity];
p2 = Plot[func1[f1], {f1, ffmin, ffmax}, DisplayFunction → Identity];
p3 = Show[p1, p2, PlotRange → All, Frame → True, Axes → False,
  FrameLabel → {"freq (kHz)", "Amplitude"}, DisplayFunction → $DisplayFunction];

f0result = f0 /. result;
Qresult = Q /. result;
AAresult = AA /. result;
```

$$kmresult = \frac{8\,Qresult^3\,1.38\times10^{-23}\,293.15\times10^{18}}{(AAresult)^2\,\left(4\,Qresult^2-1\right)\,\pi\,f0result}\;\frac{1}{max};$$

$$KSEaddition = Total\Big[Table\Big[\left(\frac{klist2[[ii,\,1]]}{klist2[[ii,\,2]]}\right)^2\left(\frac{f0result}{klist[[ii,\,1]]}\right)^4$$

$$\left(\frac{\texttt{1}}{\texttt{klist[[ii, 1]] klist[[ii, 3]]}}\right)\texttt{, \{ii, 1, Length[klist2]\}]];}$$

```
f0SEresult = FullForm[ParameterTable /. NonlinearRegress[data2, amp[f, Adc, AA, f0, Q],
      f, {{AA, Apeak}, {f0, fpeak}, {Q, Qest}}, MaxIterations → 100,
      AccuracyGoal → 8, RegressionReport → ParameterTable]][[1, 1, 2, 2]];
QSEresult = FullForm[ParameterTable /. NonlinearRegress[data2, amp[f, Adc, AA, f0, Q],
      f, {{AA, Apeak}, {f0, fpeak}, {Q, Qest}}, MaxIterations → 100,
      AccuracyGoal → 8, RegressionReport → ParameterTable]][[1, 1, 3, 2]];
AASE = (AAresult 0.1 + FullForm[ParameterTable /. NonlinearRegress[data2, amp[f, Adc,
          AA, f0, Q], f, {{AA, Apeak}, {f0, fpeak}, {Q, Qest}}, MaxIterations → 100,
         AccuracyGoal → 8, RegressionReport → ParameterTable]][[1, 1, 1, 2]]) √max ;
```

$$\texttt{kmSEresult2} = \sqrt{\Biggl(\Biggl(\biggl(\frac{1}{\texttt{AAresult}^{2}\ \texttt{f0result}}\ \frac{1}{\texttt{max}}\ \frac{\texttt{Qresult}^{2}}{(4\ \texttt{Qresult}^{2}-1)}\biggr)^{2}\ \biggl(\frac{(4\ \texttt{Qresult}^{2}-3)^{2}}{(4\ \texttt{Qresult}^{2}-1)^{2}}\ \texttt{QSEresult} + \Bigl(\frac{2\ \texttt{Qresult}}{\texttt{AAresult}}\Bigr)^{2}\ \frac{1}{\texttt{max}}\ \texttt{AASE}^{2} + \Bigl(\frac{\texttt{Qresult}}{\texttt{f0result}}\Bigr)^{2}\ \texttt{f0SEresult}^{2}\biggr)\ \Bigl(\frac{8\ \ 1.38\times 10^{-23}\ 293.15\times 10^{18}}{\pi}\Bigr)^{2}\Biggr)}\ \texttt{;}$$

$$\texttt{kmSEresult} = \sqrt{\texttt{kmSEresult2}^{2} + \texttt{KSEaddition} + \texttt{List3[[2]]}^{2}}\ \texttt{;}$$

```
Print["km value = ", Abs[kmresult], " ; km SE = ", Abs[kmSEresult]];
Print["f0 = ", f0result, " ; Q = ",
 Abs[Qresult], " ; ParameterTable = ", ParameterTable /.
  NonlinearRegress[data2, amp[f, Adc, AA, f0, Q], f, {{AA, Apeak}, {f0, fpeak}, {Q, Qest}},
   MaxIterations → 100, AccuracyGoal → 8, RegressionReport → ParameterTable]];

PrependTo[List1, {f0result, f0SEresult,
  Abs[Qresult], Abs[QSEresult], Abs[kmresult], Abs[kmSEresult], g}];
PrependTo[List2, {kmSEresult, kmresult, g}];


Qm = Qresult;
fm = f0result;
km = kmresult;
```

$$\texttt{model5[f\_] :=}\left(10^{9}\sqrt{\frac{\text{kb T}}{\text{km}}\,\frac{2}{\pi\,\text{fm Qm}}\,\frac{\text{fm}^{4}}{\left(\text{fm}^{2}-\text{f}^{2}\right)^{2}+\frac{\text{f}^{2}\,\text{fm}^{2}}{\text{Qm}^{2}}}}\right)^{2};$$

```
 Show[ListPlot[DeleteCases[
     Map[If[ffmin > #[[1]] || #[[1]] > ffmax, 0, #] &, datac1 ], 0], PlotRange → All],
   Show[Plot[model5[f], {f, ffmin, ffmax}, PlotRange → All, PlotStyle → Red]],
   Show[Plot[model5[f] + max model7[f], {f, ffmin, ffmax}, PlotRange → All]]]
 ];

finalPlot[] := Module[{},
  klist2 = DeleteDuplicates[List1, #1[[-1]] == #2[[-1]] &];
```

$$\texttt{model8[f\_, fm\_, Qm\_, km\_] :=}\left(10^{9}\sqrt{\frac{\text{kb T}}{\text{km}}\,\frac{2}{\pi\,\text{fm Qm}}\,\frac{\text{fm}^{4}}{\left(\text{fm}^{2}-\text{f}^{2}\right)^{2}+\frac{\text{f}^{2}\,\text{fm}^{2}}{\text{Qm}^{2}}}}\right)^{2};$$

```
  model9[ff_] := Total[Table[model8[ff, klist2[[ii, 1]],
      klist2[[ii, 3]], klist2[[ii, 5]]], {ii, 1, Length[klist2]}]];

  List1 = DeleteDuplicates[List1, #1[[-1]] == #2[[-1]] &];


  Show[LogPlot[model9[hj], {hj, datac1[[1, 1]], datac1[[-1, 1]]}, PlotRange → All,
    PlotStyle → Red], ListLogPlot[datac1, PlotRange → All, PlotStyle → Opacity[0.5]]]]
```

Evaluation

```
freqstep
```

```
3.05194
```

For example, to fit the resonance peak between 4.5 and 6.5 (kHz) with an initial estimate of f0 = 5 (kHz) and Q = 4, enter the following.
NOTE: Frequency units are specified by datafile.
The last part should be a string, "z0" for mode 1, "z1" and "z2" for mode 3

```
ffit[5000, 4, 4000, 6400, "z0"]
```

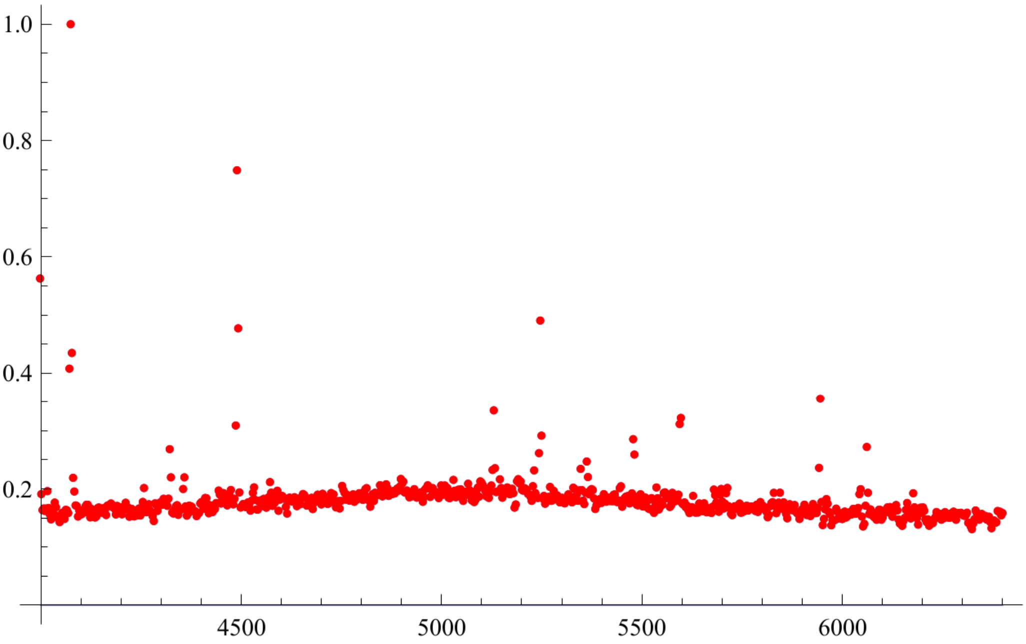

km value = 3.94139 × 10^{15} ; km SE = 1.00024 × 10^{15}

f0 = 6128.1 ; Q = 1.1964 ; ParameterTable =

	Estimate	Asymp. SE	TStat	PValue
AA	0.438849	0.00283179	154.972	7.344955146983985 × 10^{-591}
f0	6128.1	149.656	40.948	0.
Q	1.1964	0.0795091	15.0474	0.

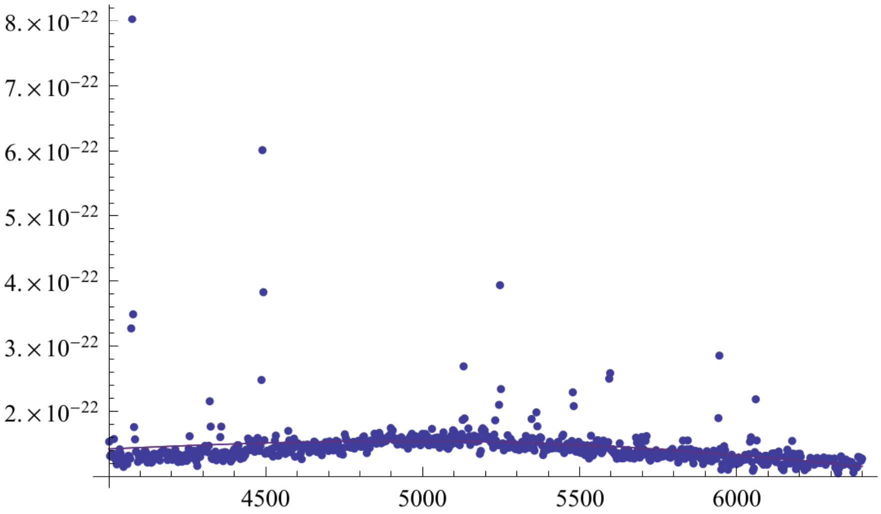

APPENDIX F – Adsorbate mass and rigidity determination

Density [kg m^(-3)] and viscosity [kg m^(-1) s^(-1)] of reference medium [e.g., air : ρ = 1.18; η = 1.86 *10^(-5); water : ρ = 1.0 *10^(3); η = 8.6 *10^(-4)];

Hydrodynamic function

```
Clear["Global`*"] (* Clear all *)
ρ = 1.0 * 10 ^ (3);
η = 8.6 * 10 ^ (-4);
```

The Reynolds number of the flow:

```
Ren[f_, b_] := ρ f b^2 / (4 η)
```

The correction function $\Omega(\omega)$ (such that $\Gamma(\omega)$_r = $\Omega(\omega)$ $\Gamma(\omega)$_c) is computed using a nonlinear least squares regression as a function of log10(Re). $\Omega(\omega)$ is composed of a real and imaginary component: $\Omega(\omega)$ = Gr + i Gi.

```
Gr[z_] := (0.91324 - 0.48274 z + 0.46842 z^2 - 0.12886 z^3 + 0.044055 z^4 - 0.0035117 z^5 +
(1 - 0.56964 z + 0.48690 z^2 - 0.13444 z^3 + 0.045155 z^4 - 0.0035862 z^5 + 0.00069085 z^6);

Gi[z_] := (-0.024134 - 0.029256 z + 0.016294 z^2
- 0.00010961 z^3 + 0.000064577 z^4 - 0.00004451 z^5)/
(1 - 0.59702 z + 0.55182 z^2 - 0.18357 z^3 + 0.079156 z^4 - 0.014369 z^5 + 0.0028361 z^6);

Cfun[z_] := Gr[z] + I Gi[z];
```

The hydrodynamic function for a circular cylinder is known, being (expressed in terms of Re)

```
Gcirc[f_, b_] := 1 + (4 I BesselK[1, - I Sqrt[I Ren[f,b]]])/
(Sqrt[ I Ren[f,b]] BesselK[0, - I Sqrt[I Ren[f,b]]]);
```

The Hydrodynamic function for a rectangular beam can then be appoximated as

```
Grect[f_, b_] := Cfun[Log[10, Ren[f,b]]] Gcirc[f,b];
```

Redefine notation, use Γ for hydrodynamic function:

```
Γ[f_, b_] := Cfun[Log[10, Ren[f, b]]] Gcirc[f, b];
```

In the following, insert the dimensions in μm (width b and thickness t_c), frequencies in kHz, and density in kg$/m^3$:

```
b = 100;
fbare = 5.1136;
Qbare = 3.317;
f = 4.476;
Δf = f - fbare;
Q = 3.151;
ΔQ = Q - Qbare;
fbarevac = 30; (* This is typically several times f₀ *)
ρc = 2330;
tc = 0.940;
```

```
Re[Γ[2 π 1000 (f), 0.0001]]
```

```
1.35686
```

```
Im[Γ[2 π 1000 (f), 0.0001]]
```

```
0.326817
```

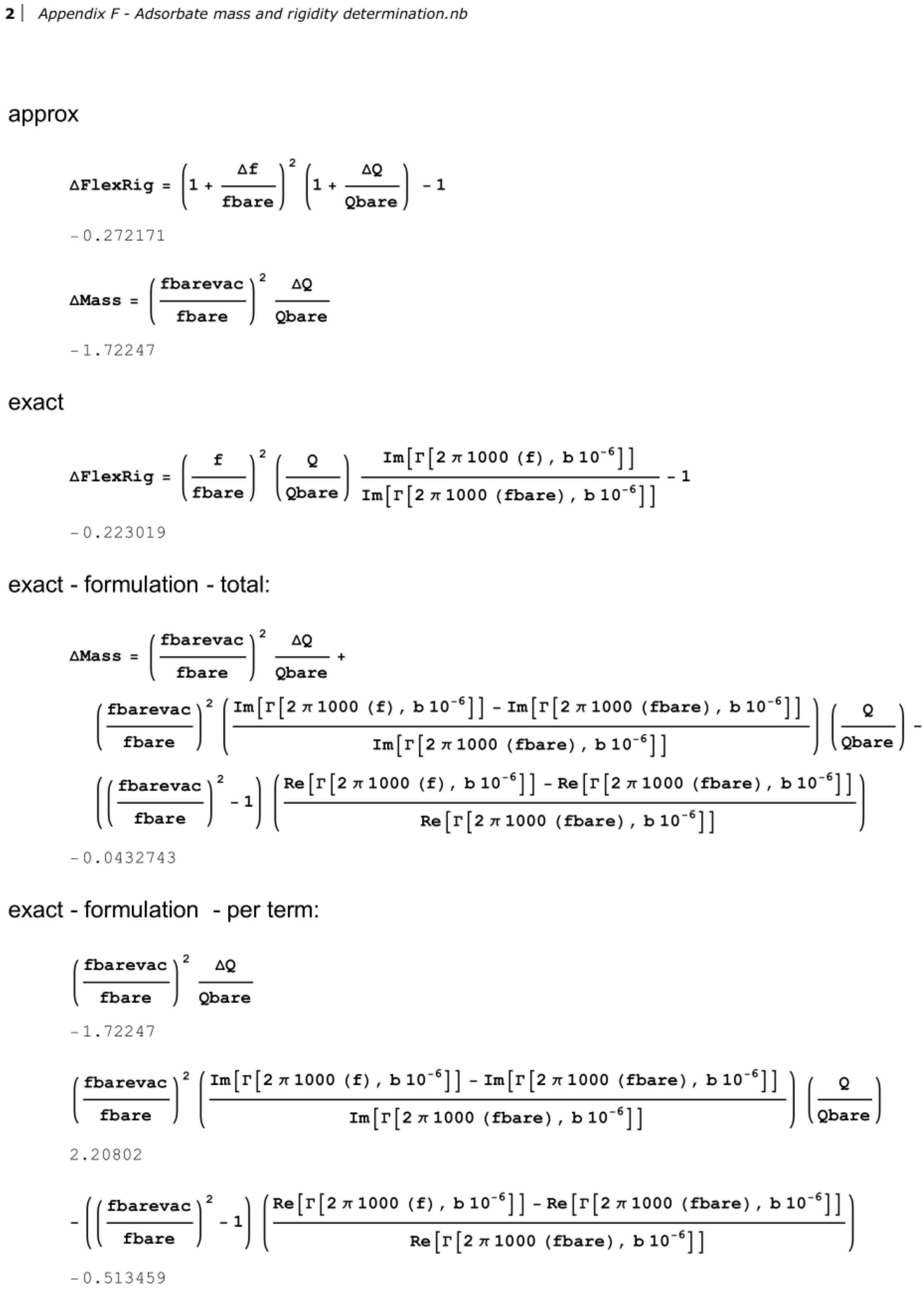

2 | *Appendix F - Adsorbate mass and rigidity determination.nb*

approx

$$\Delta\text{FlexRig} = \left(1 + \frac{\Delta f}{\text{fbare}}\right)^2 \left(1 + \frac{\Delta Q}{\text{Qbare}}\right) - 1$$

```
-0.272171
```

$$\Delta\text{Mass} = \left(\frac{\text{fbarevac}}{\text{fbare}}\right)^2 \frac{\Delta Q}{\text{Qbare}}$$

```
-1.72247
```

exact

$$\Delta\text{FlexRig} = \left(\frac{f}{\text{fbare}}\right)^2 \left(\frac{Q}{\text{Qbare}}\right) \frac{\text{Im}\left[\Gamma\left[2\,\pi\,1000\,(f),\, b\,10^{-6}\right]\right]}{\text{Im}\left[\Gamma\left[2\,\pi\,1000\,(\text{fbare}),\, b\,10^{-6}\right]\right]} - 1$$

```
-0.223019
```

exact - formulation - total:

$$\Delta\text{Mass} = \left(\frac{\text{fbarevac}}{\text{fbare}}\right)^2 \frac{\Delta Q}{\text{Qbare}} + \left(\frac{\text{fbarevac}}{\text{fbare}}\right)^2 \left(\frac{\text{Im}\left[\Gamma\left[2\,\pi\,1000\,(f),\, b\,10^{-6}\right]\right] - \text{Im}\left[\Gamma\left[2\,\pi\,1000\,(\text{fbare}),\, b\,10^{-6}\right]\right]}{\text{Im}\left[\Gamma\left[2\,\pi\,1000\,(\text{fbare}),\, b\,10^{-6}\right]\right]}\right) \left(\frac{Q}{\text{Qbare}}\right) - \left(\left(\frac{\text{fbarevac}}{\text{fbare}}\right)^2 - 1\right) \left(\frac{\text{Re}\left[\Gamma\left[2\,\pi\,1000\,(f),\, b\,10^{-6}\right]\right] - \text{Re}\left[\Gamma\left[2\,\pi\,1000\,(\text{fbare}),\, b\,10^{-6}\right]\right]}{\text{Re}\left[\Gamma\left[2\,\pi\,1000\,(\text{fbare}),\, b\,10^{-6}\right]\right]}\right)$$

```
-0.0432743
```

exact - formulation - per term:

$$\left(\frac{\text{fbarevac}}{\text{fbare}}\right)^2 \frac{\Delta Q}{\text{Qbare}}$$

```
-1.72247
```

$$\left(\frac{\text{fbarevac}}{\text{fbare}}\right)^2 \left(\frac{\text{Im}\left[\Gamma\left[2\,\pi\,1000\,(f),\, b\,10^{-6}\right]\right] - \text{Im}\left[\Gamma\left[2\,\pi\,1000\,(\text{fbare}),\, b\,10^{-6}\right]\right]}{\text{Im}\left[\Gamma\left[2\,\pi\,1000\,(\text{fbare}),\, b\,10^{-6}\right]\right]}\right) \left(\frac{Q}{\text{Qbare}}\right)$$

```
2.20802
```

$$-\left(\left(\frac{\text{fbarevac}}{\text{fbare}}\right)^2 - 1\right) \left(\frac{\text{Re}\left[\Gamma\left[2\,\pi\,1000\,(f),\, b\,10^{-6}\right]\right] - \text{Re}\left[\Gamma\left[2\,\pi\,1000\,(\text{fbare}),\, b\,10^{-6}\right]\right]}{\text{Re}\left[\Gamma\left[2\,\pi\,1000\,(\text{fbare}),\, b\,10^{-6}\right]\right]}\right)$$

```
-0.513459
```

APPENDIX F

Determination of mass density and viscosity of a medium via the properties of oscillating rectangular cantilevers.

Mathematica notebook modified from Sader's implementation (downloaded from http://www.ampc.ms.unimelb.edu.au/afm/) of spring constant calibration using the method of Sader et al., Rev. Sci. Instrum., 70, 3967 (1999).
The calculation for mass density and viscosity of the medium follows Boskovic et al., Journal of Rheology 46, 891-899 (2002). The linear mass density and resonance frequency in vacuum can best be obtained by a measurement in a reference medium.

Cantilever dimensions are to be given in μm, frequencies in kHz.

* Note: Default density and viscosity of air are entered under the "equations" heading. Please change these if required.

Equations

Cantilever parameters: cantilever width b [in μm], linear density μ [kg m^(-1)], resonance frequencies in vacuum fvac and in medium f [in kHz], and quality factor Q:

```
b = 29;
μ = 1.39359 × 10^(-7);
fvac = 85.9432;
f = 34.2;
Q = 4.34;
```

Density [kg m^(-3)] and viscosity [kg m^(-1) s^(-1)] of reference medium [e.g., air: ρ = 1.18; η = 1.86 *10^(-5); water: ρ = 1.0 *10^(3); η = 8.6 *10^(-4)]. These will form the starting point for finding the roots of the two coupled equations below.

```
ρ0 = 1.18;
η0 = 1.86 * 10^(-5);
```

The Reynolds number of the flow:

```
Ren[ρ_, η_] := ρ (2 π 1000 f) (b 10^(-6))^2 / (4 η)
```

The correction function Ω(ω) (such that Γ(ω)_r = Ω(ω) Γ(ω)_c) is computed using a nonlinear least squares regression as a function of log10(Re). Ω(ω) is composed of a real and imaginary component: Ω(ω) = Gr + i Gi.

```
Gr[z_] := (0.91324 - 0.48274 z + 0.46842 z^2 - 0.12886 z^3 + 0.044055 z^4 - 0.0035117 z^5 +
(1 - 0.56964 z + 0.48690 z^2 - 0.13444 z^3 + 0.045155 z^4 - 0.0035862 z^5 + 0.00069085 z^6);

Gi[z_] := (-0.024134 - 0.029256 z + 0.016294 z^2
- 0.00010961 z^3 + 0.000064577 z^4 - 0.00004451 z^5)/
(1 - 0.59702 z + 0.55182 z^2 - 0.18357 z^3 + 0.079156 z^4 - 0.014369 z^5 + 0.0028361 z^6);

Cfun[z_] := Gr[z] + I Gi[z];
```

The hydrodynamic function for a circular cylinder is known, being (expressed in terms of Re)

```
Gcirc[ρ_, η_] := 1 + (4 I BesselK[1, - I Sqrt[I Ren[ρ,η]]])/
(Sqrt[ I Ren[ρ,η]] BesselK[0, - I Sqrt[I Ren[ρ,η]]]);
```

The Hydrodynamic function for a rectangular beam can then be appoximated as

```
Grect[ρ_, η_] := Cfun[Log[10, Ren[ρ,η]]] Gcirc[ρ,η];
```

Corrected Hydrodynamic function to facilitate the solution for mass density ρ and viscosity η:

```
Grectcorr[ρ_, η_] := π ρ (b 10^(-6))^2 / (4 μ) Grect[ρ, η];
```

Solve for mass density and viscosity

The following line solves the two coupled equations for resonance frequency and quality factor in a medium, to yield the mass density ρ and the viscosity η of the medium.

```
FindRoot[{Re[Grectcorr[ρ, η]] == (fvac / f)^2 - 1,
  Im[Grectcorr[ρ, η]] == Q^(-1) (fvac / f)^2}, {{ρ, ρ0}, {η, η0}}]
```

```
{1000. → 739.908, 0.00086 → 0.000589519}
```